

AD-A021 998

NATURAL AND ARTIFICIAL ILLUMINATION IN OPTICALLY
THICK ATMOSPHERES

Robert E. Turner, et al

Environmental Research Institute of Michigan

Prepared for:

Picatinny Arsenal

10 April 1975

DISTRIBUTED BY:

NTIS

National Technical Information Service
U. S. DEPARTMENT OF COMMERCE

084105

108300-4-F

ADA021998

Final Report

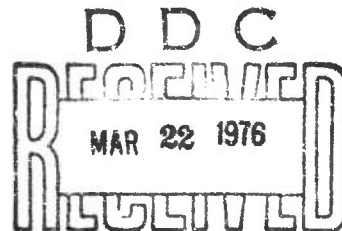
NATURAL AND ARTIFICIAL ILLUMINATION IN OPTICALLY THICK ATMOSPHERES

Robert E. Turner and Peter F. Lambeck
INFRARED AND OPTICS DIVISION

APRIL 1975

Distribution of this document is unlimited.

U.S. Army
Picatinny Arsenal
Dover, New Jersey
Contract No. DAAA21-74-C-0331



**ENVIRONMENTAL
RESEARCH INSTITUTE OF MICHIGAN**
FORMERLY WILLOW RUN LABORATORIES, THE UNIVERSITY OF MICHIGAN
BOX 618 • ANN ARBOR • MICHIGAN 48107

NOTICES

Sponsorship. The work reported herein was conducted by the Environmental Research Institute of Michigan for the U.S. Army, Picatinny Arsenal, Dover, New Jersey, Contract No. DAAA21-74-C-0331. Contracts and grants to the Institute for the support of sponsored research are administered through the Office of Contracts Administration.

Distribution. Initial distribution is indicated at the end of this document.

DDC Availability. Qualified requesters may obtain copies of this document from:

Defense Documentation Center
Cameron Station
Alexandria, Virginia 22314

Final Disposition. After this document has served its purpose, it may be destroyed. Please do not return it to the Environmental Research Institute of Michigan.

ACCESSION 127	
NTIS	127
DDC	127
UNCLASSIFIED	
CONFIDENTIAL	
BY _____	
DATE _____	
FBI	
A	

UNCLASSIFIED

SECURITY CLASSIFICATION OF THIS PAGE (When Data Entered)

REPORT DOCUMENTATION PAGE		READ INSTRUCTIONS BEFORE COMPLETING FORM
1. REPORT NUMBER 108300-4-F	2. GOVT ACCESSION NO.	3. RECIPIENT'S CATALOG NUMBER
4. TITLE (and Subtitle) NATURAL AND ARTIFICIAL ILLUMINATION IN OPTICALLY THICK ATMOSPHERES		5. TYPE OF REPORT & PERIOD COVERED Final, 3/18/74 - 4/10/75
		6. PERFORMING ORG. REPORT NUMBER ERIM 108300-4-F
7. AUTHOR(s) Robert E. Turner Peter F. Lambeck		8. CONTRACT OR GRANT NUMBER(s) DAAA21-74-C-0331
9. PERFORMING ORGANIZATION NAME AND ADDRESS Environmental Research Institute of Michigan Infrared and Optics Division P.O. Box 618 Ann Arbor, Michigan 48107		10. PROGRAM ELEMENT, PROJECT, TASK AREA & WORK UNIT NUMBERS
11. CONTROLLING OFFICE NAME AND ADDRESS U. S. Army Picatinny Arsenal Dover, New Jersey 07801		12. REPORT DATE 10 April 1975
		13. NUMBER OF PAGES 121
14. MONITORING AGENCY NAME AND ADDRESS (if different from Controlling Office)		15. SECURITY CLASS. (of this report) Unclassified
		15a. DECLASSIFICATION/DOWNGRADING SCHEDULE
16. DISTRIBUTION STATEMENT (of this Report) Distribution of this document is unlimited		
17. DISTRIBUTION STATEMENT (of the abstract entered in Block 20, if different from Report)		
18. SUPPLEMENTARY NOTES		
19. KEY WORDS (Continue on reverse side if necessary and identify by block number) Nighttime Illumination Flares Radiative Transfer Aerosol Scattering Fogs		
20. ABSTRACT (Continue on reverse side if necessary and identify by block number) In the analysis of target signatures it is essential that the illumination level be defined and determined for a variety of environmental conditions. This report deals primarily with two important sources of illumination, the moon and man-made flares. The illumination due to the moon is calculated using an atmospheric-radiative-transfer model which includes multiple scattering by gases and particulates in the atmosphere but does not include absorption due to gases. A variety of atmospheric states is considered, from very clear atmospheres to very hazy.		

DD FORM 1473 EDITION OF 1 NOV 66 IS OBSOLETE

UNCLASSIFIED

SECURITY CLASSIFICATION OF THIS PAGE (When Data Entered)

UNCLASSIFIED

SECURITY CLASSIFICATION OF THIS PAGE (When Data Entered)

20. (Continued)

A detailed analysis of fogs was carried out and density profiles were calculated to represent different kinds of fogs. A mathematically exact formula was developed which allows one to calculate the surface illumination due to one or more point sources (flares). Calculations were performed to determine surface illumination in terms of distance from source, source height, height of fog layer, and visibility. Contours were plotted which illustrate the surface illumination for various flare configurations.

UNCLASSIFIED

SECURITY CLASSIFICATION OF THIS PAGE (When Data Entered)

PREFACE

This report describes work performed on atmospheric-radiative-transfer models as part of the Army's target signature analysis program. In the development of a comprehensive model which embodies reflectance, illumination, transmittance, and detector submodels we have considered in some detail an illumination model for poor atmospheric conditions. In particular, we analyzed mathematically the natural radiation field at the Earth's surface arising from the moon in various phases. We also examined the illumination on the surface as a result of man-made flares embedded within fogs.

For several years the Environmental Research Institute of Michigan (ERIM) has been developing atmospheric-radiative-transfer models primarily for use in the analysis of multispectral data acquired by satellites and aircraft. The present study extends our capability to analyze artificial sources and extremely dense atmospheres.

The research described in this report was performed under Contract DAAA21-74-C-0331 and covers the period from 18 March 1974 through 10 April 1975. Mr. Matthew Nowak served as Technical Monitor. The program was directed by R. R. Legault, Vice President of ERIM and R. E. Turner, Principal Investigator. The ERIM number of this report is 108300-4-F.

The authors wish to acknowledge the direction provided by R. R. Legault. J. D. Erickson, Head of ERIM's Information Systems and Analysis Department read the report and made suggestions. Computer programming was done by L. R. Ziegler, W. Wolber, and P. F. Lambeck, who also contributed a section on programming problems. The authors also thank D. Dickerson for her secretarial assistance in the preparation of this report.

CONTENTS

PREFACE.	1
CONTENTS	2
ILLUSTRATIONS.	3
1. SUMMARY.	7
2. INTRODUCTION	8
3. ATMOSPHERIC STRUCTURE.	10
3.1 Gases	10
3.2 Aerosols.	10
3.3 Optical Weather	13
3.3.1 Hazes.	13
3.3.2 Fogs	16
4. ATTENUATION OF RADIATION	21
4.1 Transmittance	21
4.2 Attenuation Coefficients.	22
4.2.1 Visibility	22
4.2.2 Hazes.	25
4.2.3 Fogs	27
5. NATURAL RADIATION.	50
5.1 Solar Spectrum.	50
5.2 The Lunar Spectrum.	51
5.2.1 Extraterrestrial Values.	51
5.2.2 Sea Level Values (Measured).	55
5.2.3 Sea Level Values (Calculated).	58
6. ARTIFICIAL SOURCES	73
6.1 Point Source.	73
6.2 Distributed Source.	74
6.3 The Radiation Field	74
6.4 Results of Calculations	77
6.5 Illumination Model.	97
7. COMPUTATIONAL METHODS.	102
7.1 Simplifications and Approximations Which Reduce Computational Expense	103
7.2 Simplifications and Approximations Which Make the Equation Soluble	106
8. CONCLUSIONS AND RECOMMENDATIONS.	111
APPENDIX	116
REFERENCES	118

ILLUSTRATIONS

1. Haze-Type Distribution Functions Used.	15
2. The Saturation Curve	17
3. Aerosol Distributions as a Function of Lapse Time After the Initiation of the Condensation Process	20
4. Detection of Direct and Background Radiation	24
5. Variation of Visual Range With Extinction Coefficient.	26
6. Spectral Attenuation and Scattering Coefficients for Various Haze (L,M,H) and Cloud (C_1, C_2, C_3) Models (Adapted from Deirmendjian).	28
7. Aerosol Attenuation Coefficients Vs Altitude at $\lambda_1 = 0.55\mu$	29
8. Atmospheric Transmittance Spectra for Selective Fogs as Measured by Arnulf et al.	31
9. Atmospheric Transmittance Spectra for Evolving Fogs as Measured by Arnulf et al.	32
10. Atmospheric Transmittance Spectra for Stable Fogs, Type 1, as Measured by Arnulf et al	33
11. Atmospheric Transmittance Spectra for Stable Fogs, Type 2, as Measured by Arnulf et al	34
12. Measured and Computed Fog Spectral Attenuations Illustrating Goodness of Fit.	35
13. Typical Values Found for Atmospheric Extinction Coefficient Vs Wavelength	36
14. Scattering Efficiency Factor for Homogeneous Spheres of Complex Refractive Index m	40
15. Absorption Efficiency Factor for Homogeneous Spheres of Complex Refractive Index m	41
16. Total Efficiency Factor for Homogeneous Spheres of Complex Refractive Index m	42

ILLUSTRATIONS (Cont'd)

17. Single-Scattering Polydisperse Phase Function.	45
18. Vertical Distribution of Liquid Water Content in Fog	49
19. Variation in a Lunation.	52
20. Geometrical Albedo Vs. Wavelength.	54
21. Solar and Lunar Spectral Irradiance at the Top of Earth's Atmosphere.	56
22. Natural Luminous Incidence (Illuminance) as a Function of Solar and Lunar Altitude and for Various Phases of the Moon as Measured by Brown.	57
23. Night Sky Radiant Sterance Spectra for Various Altitudes of the Moon as Measured by Vatsia, Stich and Dunlap.	59
24. Irradiance from Full Moonlight Plus Airglow	60
25. Irradiance from 0.3 x Full Moonlight Plus Airglow	60
26. Irradiance from 0.1 x Full Moonlight Plus Airglow	61
27. Irradiance from 0.03 x Full Moonlight Plus Airglow.	61
28. Diffuse Lunar Irradiance at the Earth's Surface Vs. Lunar Zenith Angle	62
29. Diffuse Lunar Irradiance at the Earth's Surface Vs. Lunar Zenith Angle	64
30. Total Irradiance at the Earth's Surface Vs. Lunar Zenith Angle. . .	65
31. Total Irradiance at the Earth's Surface Vs. Lunar Zenith Angle. . .	66
32. Total Lunar Irradiance at the Earth's Surface Vs. Visibility. . . .	67
33. Total Irradiance at the Earth's Surface Vs. Visibility.	68
34. Total and Downward Diffuse Lunar Irradiance at the Earth's Surface Vs. Transmittance	59
35. Diffuse Downward Lunar Irradiance at the Earth's Surface Vs. Back- ground Reflectance.	70

ILLUSTRATIONS (Cont'd)

36. Total Lunar Irradiance at the Earth's Surface Vs. Background Reflectance.	72
37. Point Source Geometry.	75
38. Natural and Artificial Illumination Configuration.	77
39. Direct Plus Singly Scattered Irradiance Generated by a Point Source of Radiation Vs. Distance on the Ground from the Source . .	79
40. Direct Plus Singly Scattered Irradiance Generated by a Point Source of Radiation Vs. Distance on the Ground from the Source . .	80
41. Direct Plus Singly Scattered Irradiance Generated by a Point Source of Radiation Vs. Distance on the Ground from the Source . .	81
42. Direct Plus Singly Scattered Irradiance Generated by a Point Source of Radiation Vs. Altitude of the Source	82
43. Direct Plus Singly Scattered Irradiance Generated by a Point Source of Radiation Vs. Visibility in a Fog.	84
44. Direct Plus Singly Scattered Irradiance Generated by a Point Source of Radiation Vs. Visibility in a Fog.	85
45. Direct and Singly Scattered Irradiance Generated by a Point Source of Radiation Vs. Wavelength	86
46. Direct and Singly Scattered Irradiance Generated by a Point Source of Radiation Vs. Wavelength	87
47. Direct and Singly Scattered Irradiance Generated by a Point Source of Radiation Vs. Wavelength	89
48. Direct and Singly Scattered Irradiance Generated by a Point Source of Radiation Vs. Wavelength	90
49. Power Output of Mark 45 Flare Vs. Wavelength	91
50. Power Output of SR 485 Flare Extrapolated to Mark 45 Size and Burning Rate Vs. Wavelength.	92
51. Direct and Singly Scattered Irradiance Generated by a Mark 45 Flare Vs. Wavelength	93

ILLUSTRATIONS (Cont'd)

52.	Contours of Constant Direct Plus Singly Scattered Irradiance Generated by Three Mark 45 Flares.	94
53.	Contours of Constant Direct Plus Singly Scattered Irradiance Generated by Three Mark 45 Flares.	95
54.	Contours of Constant Direct Plus Singly Scattered Irradiance Generated by Three Mark 45 Flares.	96
55.	Contours of Constant Direct Plus Singly Scattered Irradiance Generated by Four Mark 45 Flares	98
56.	Contours of Constant Direct Plus Singly Scattered Irradiance Generated by Four Mark 45 Flares	99
57.	Illumination Model for Natural and Artificial Sources.	100

SUMMARY

Over the last seven years considerable effort has been spent on atmospheric-radiative-transfer modeling at the Environmental Research Institute of Michigan (ERIM). Much of this effort has been associated with remote sensing applications using aircraft and satellite multi-spectral data. This report is a continuation of atmospheric-radiative-transfer modeling techniques with particular emphasis on low visibility atmospheres and artificial sources.

The impetus for this study arises from a need by the Army to develop a comprehensive model for the target signature analysis program which can be used to determine illumination levels on military scenes as a result of natural and artificial sources. In this investigation we considered in detail the natural illumination on the Earth's surface as a result of the moon in various phases and, in particular for various atmospheric states. It was found that the illumination is dependent upon atmospheric visibility and surface reflectance in a predictable but somewhat surprising way.

A major part of this study involved the analysis of the illumination levels due to one or more flares (isotropic point sources) embedded either within or outside of dense fogs. It was found that the spatial distribution over the surface was quite extended for flares above the fog layer but more concentrated when the flare was inside the fog. Contours are plotted which show the illumination levels for several flares in various configurations.

In the final section of this report we discuss the advances made as a result of this investigation and we recommend additional studies to continue the current modeling effort in order to develop the most realistic atmospheric radiation for target signature analysis.

INTRODUCTION

In order to model the real world of illumination it is necessary that experiments be conducted to determine typical values of quantities which one ultimately would like to measure or know in order to quantify a realistic environment. It is oftentimes not practical to conduct the possibly enormous number of measurements which would be necessary to define all environmental conditions however. For this reason, it is desirable that one develop a model of the realistic environment and test the model calculations with experimental data. Such a procedure will then determine the range of validity of the model and enable the user to gain confidence in the use of model calculations to simulate specific missions.

Although a number of measurements of the natural nighttime illumination of the Earth's surface have been made over the years, there have been no attempts to model realistic atmospheres and the nighttime illumination through these atmospheres starting from the basic principles of radiative-transfer. In subsequent sections of this report we will make use of an atmospheric-radiative-transfer model to calculate the natural nighttime spectral irradiance on the Earth's surface as a result of the moon. It should be noted that the procedure of developing a mathematical model is generally preferable to the method of using a strictly empirical model of the radiation field. This is true because the great variation in environmental factors can preclude practical use of empirical models. Thus, making use of an empirical model of, say, illumination vs. visibility, would lead one to consider only that factor when, in reality other conditions such as fog profile, e.g., might have a more important effect on the overall results. Therefore, a mathematical model based upon sound physical principles should be of greater utility to the user in the practical implementation of the model to simulate reality.

In a later section we will develop a model of artificial point sources (flares) embedded in various atmospheres of varying degrees of turbidity. The model developed is approximate only in the sense that multiple scattering is neglected. Realistic atmospheric states may be considered and the results are valid for wavelengths in the visible and near infrared, except for the bands of gaseous absorption.

Finally, we model several point sources located at specified positions in a horizontally uniform atmosphere which is also being illuminated by moonlight. Contours of the irradiance are presented which show the relative magnitude of artificial and natural radiation fields. With these computational procedures one can simulate a great variety of situations involving natural and artificial sources of illumination under nighttime conditions.

ATMOSPHERIC STRUCTURE

In this chapter we shall discuss the physical state of the atmosphere in general terms. Thus, we shall characterize the weather in terms of the static conditions of the gaseous component and the particulate component, i.e., we exclude specific temporal changes due to wind and precipitation. We shall define the complete optical state of the atmosphere for all conditions in which precipitation does not occur.

3.1 GASES

Our atmosphere is composed of the major permanent gaseous components, molecular oxygen, nitrogen, and argon. These gases absorb very little radiation in the visible and near-infrared part of the spectrum, whereas the variable gaseous components, water vapor, carbon dioxide, ozone, sulfur dioxide, nitrogen compounds, methane, and other trace gases do absorb a significant amount of radiation. Of these components, ozone, water vapor, and carbon dioxide are the most important absorbers of radiation in the near-infrared. If other gases are introduced to the immediate environment where observations are being made then some quantitative parameterization of their composition and concentration must be made in order to account for the attenuation of radiation. It is beyond the scope of this report to consider gaseous absorption in detail. More detailed studies of atmospheric gases have been done by Goody [1].

3.2 AEROSOLS

One may define an aerosol as a semi-permanent suspension of solid or liquid particles in the Earth's atmosphere. Typical aerosol distributions would be hazes, clouds, mists, fogs, smokes, and dusts. It is the aerosol component of the atmosphere which is quite variable. Depending upon location and time, aerosols can have many compositions, sizes, shapes, and densities. In condensation processes, the predominant composition

[1] R. M. Goody, Atmospheric Radiation, Oxford University Press, New York, 1964.

is water (for which the refractive index is well known). Depending upon the history of the distribution, however, various contaminants can mix with water and water vapor in the formation of droplets to produce a composition quite different from that of water. The major primary source of atmospheric aerosols on a world-wide basis is sea spray [2]; other primary sources are wind-blown dust and smoke from forest fires. While the composition of a world-wide aerosol distribution can be estimated, this composition can nevertheless vary over a wide range depending upon its proximity to various local sources. The only ways in which the composition can be determined is by direct in situ sampling of the air in a particular location or by radiometric techniques. Much in situ sampling has been done by Volz [3,4], Grams et al. [5], and Flanigan and DeLong [6]. As a result of their work and that of others, the mean world-wide aerosol can be considered to have a real refractive index of about 1.5 and an imaginary part between 0.01 and 1.0. Hence,

$$m(\lambda) = m_1 - im_2 \quad (1)$$

where m_1 and m_2 , respectively, are the real and imaginary part of the refractive index, and λ is the wavelength. For realistic atmospheric conditions,

$$1.33 < m_1 < 1.55 \quad (2)$$

[2] G. M. Hidy and J. R. Brock, *An Assessment of the Global Sources of Tropospheric Aerosols*, Academic Press, New York, 1971, p. 1088.

[3] F. E. Volz, *Infrared Absorption by Atmospheric Aerosol Substances*, J. Geophys. Res., 77, No. 6, 1972, p. 1017.

[4] F. E. Volz, *Infrared Optical Constants of Ammonium Sulfate, Sahara Dust, Volcanic Pumice, and Flyash*, Appl. Optics, 12, No. 3, 1973, p. 564.

[5] G. W. Grams, I. H. Blifford, Jr., E. G. Schuster, and J. J. DeLuisi, *Complex Index of Refraction of Airborne Fly Ash Determined by Laser Radar and Collection of Particles at 13 km*, J. of Atmos. Sciences, 29, 1972, p. 900.

[6] D. F. Flanigan and H. P. DeLong, *Spectral Absorption Characteristics of the Major Components of Dust Clouds*, Appl. Optics, 10, No. 1, 1971, p. 51.

and

$$0 < m_2^{\sim} < 1.0 \quad (3)$$

which are roughly independent of wavelength.

Particles also come in various sizes. Generally, however, they can be put into three categories: the Aitken nuclei with radii between 10^{-7} and 10^{-5} cm, the large particles with radii between 10^{-5} and 10^{-4} cm, and the so-called giant particles with radii greater than 10^{-4} cm. In most hazes, the optically active region is made up of those particles in the large or giant categories. Junge [7] showed that most aerosol distributions follow the simple power law:

$$n(z, r) = C(z)r^{-\nu} \quad (4)$$

where

$n(z, r)$ is the particle number density for radius, r ,
at altitude, z

ν is the exponent of the power law

Experimentally, ν has been found to vary from 2 to 5 for various tropospheric aerosol distributions. Also, other investigators have found a better fit to the particulate data by using the modified gamma distribution,

$$n(z, r) = ar^{\alpha} \exp(-br^{\gamma}); 0 \leq r < \infty \quad (5)$$

where a , α , b , and γ are parameters which describe the distribution.

For the liquid aerosols it can be assumed that the particles are spherical or nearly spherical in shape. For solid particles, however, the shape may assume any form. A number of investigators [8,9,10] have

[7] C. E. Junge, Journal Meteorol., 12, 1955, p. 13.

[8] A. C. Holland and G. Gagne, The Scattering of Polarized Light by Polydisperse Systems of Irregular Particles, Appl. Optics, 9, No. 5, 1970, p. 1113.

[9] R. S. Powell, R. R. Circle, D. C. Vogel, P. D. Woodson III, and B. Donn, Optical Scattering from Non-Spherical Randomly Aligned, Polydisperse Particles, Planet. Space Sci., 15, 1967, p. 1641.

[10] D. M. Ruthven and K. F. Loughlin, Effects of Particle Shape and Size Distribution on the Transient Solution of the Diffusion Equation, Nature Phys. Sci., 230, 1971, p. 69.

studied the influence of particle shape on the scattering of radiation. The scattering of electromagnetic radiation by odd-shaped particles has a different pattern from that produced by spherical particles; but given a polydisperse collection of odd-shaped particles, the nature of the difference is not clear. Most of the work on radiation in atmospheres concerns spherical aerosols; we shall follow suit and neglect the complications of particle shape.

3.3 OPTICAL WEATHER

Generally, we can classify almost all states of the atmosphere as being either hazy or foggy. The haze may be almost non-existent (clear) or very heavy. Fogs begin where haze or mist ends, i.e., the optical attenuation is usually much greater.

3.3.1 HAZES

Haze can be defined as a state of the atmosphere when the visibility is less than the ultimate visibility of 336 km for an aerosol-free atmosphere. For the casual observer the usual region of haze is that condition for which the visual range (at sea level) in a horizontal path lies between 23 km and 1 km.

Deirmendjian [11] has used the modified gamma distribution (Equation (5)) to characterize different hazes. The following is a list of the hazes Deirmendjian considered and the relevant parameters.

<u>Haze Type</u>	<u>a</u>	<u>α</u>	<u>γ</u>	<u>b</u>
M	5.3333×10^4	1	1/2	8.9443
L	4.9757×10^6	2	1/2	15.1186
H	4.0000×10^5	2	1	20.0000

Haze M, used to describe a marine or coastal haze, has a peak in the distribution at $r = 0.05 \mu\text{m}$. The haze L represents a continental distribution and has a peak at $r = 0.07 \mu\text{m}$. The haze H model can be used

[11] D. Deirmendjian, *Electromagnetic Scattering on Spherical Polydispersions*, Elsevier, New York, 1969, p. 78.

to represent a stratospheric aerosol or dust layers; it has a peak at 0.10 μm . A graph of the three hazes is illustrated in Figure 1. We shall make use of these hazes in the detailed analysis of atmospheric radiation.

Thus far we have considered the composition, sizes, and shapes of aerosol particles, but in order to define the atmospheric state we must also know the concentration of particles. Wiegand [12] was the first to measure the vertical profile of an aerosol number concentration of condensation nuclei. As a result of his measurements and many others cited in Ivlev [13], it was found that the concentration of condensation nuclei obeys an exponential law with altitude. It was also determined that a zone of increased concentration of large particles exists in the 17 to 23 km altitude range (Junge layer) and in a probable layer under the tropopause at 9 to 10 km. These layers are relatively stable compared to the lower part of the troposphere. As an example of an aerosol model atmosphere, Zuyev [14] has constructed the following altitude-dependent, number density-distribution-function for aerosols:

$$N(z) = \begin{cases} N(0)e^{-bz}; & z \leq 5 \text{ km} \\ 0.03; & 5 \text{ km} \leq z \leq 15 \text{ km} \\ 0.03e^{0.06z}; & 15 \text{ km} \leq z \leq 20 \text{ km} \\ 0.01e^{-0.09z}; & z \geq 20 \text{ km} \end{cases} \quad (6)$$

where $N(z)$ and $N(0)$, respectively, are the number densities at altitude z and the Earth's surface (altitude 0).

[12] C. Wiegand, Chemical Composition and Radioactivity of the Atmosphere, C. Junge, World Publishing Co., Cleveland, 1963.

[13] L. S. Ivlev, Aerosol Model of the Atmosphere, Prob. Fiz. Atmos. Leningrad, No. 7, 1967, pp. 125-160.

[14] V. Ye. Zuyev, Propagation of Visible and Infrared Waves in the Atmosphere, NASA TTF-707, NTIS, U. S. Department of Commerce, Springfield, Va., 1970.

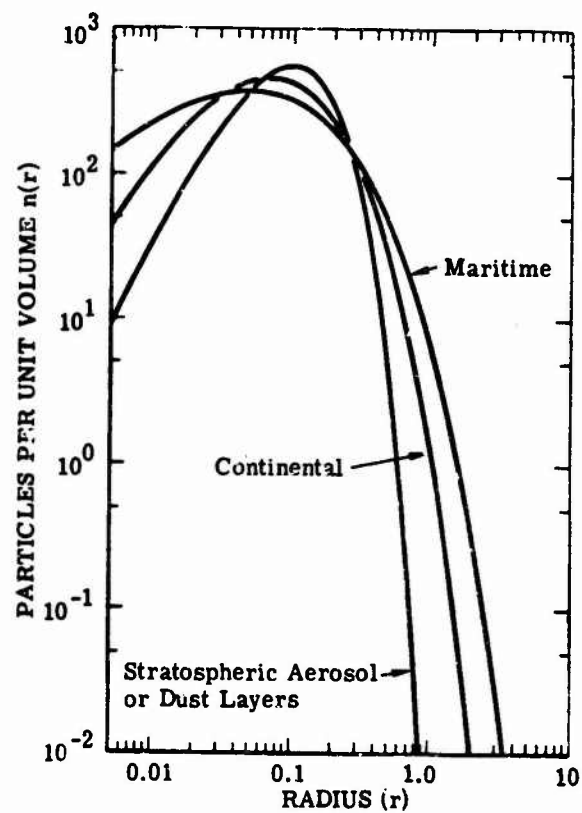


FIGURE 1. HAZE-TYPE DISTRIBUTION FUNCTIONS USED.
Units depend on the particular model.

In conclusion, we can say that the most significant aspect of aerosol particles in the atmosphere is their high degree of variability -- in composition, size distribution, and especially in number density. All the models in the current literature deal with a highly approximate average-condition from which large deviations can occur in real situations. The many details of aerosol science will not be considered in this report. For a more complete study of the physics and chemistry of aerosols, one should consult Mason [15], Fuchs [16], Davies [17], or Green and Lane [18].

3.3.2 FOGS

Fogs represent those conditions in which the visual range is less than 1 km. Thus, in the visible part of the spectrum there can be severe attenuation of radiation. In contrast to hazes the relative humidity in a fog is very high and condensation of water vapor onto small nuclei has taken place. Fogs and clouds are quite similar in terms of their optical properties but the conditions under which they form may be quite different. To understand the conditions for fog formation let us refer to Figure 2. The curve in Figure 2 represents the condition in which the air is just saturated with water vapor. At a given temperature it will hold the amount indicated by the curve. This is called the dew point. If the temperature falls then the air is supersaturated, condensation takes place and a fog or cloud forms. As a consequence, the dew point decreases because water vapor has condensed.

Fogs are generally classified according to the conditions under which they form. There are three general categories: air mass fogs, frontal fogs, and ice fogs.

[15] B. J. Mason, *The Physics of Clouds*, Clarendon Press, Oxford, 1971.

[16] N. A. Fuchs, *The Mechanics of Aerosols*, Pergamon, Elmsford, N.Y., 1964.

[17] C. N. Davies, *Aerosol Science*, Academic Press, New York, 1964.

[18] H. L. Green and W. R. Lane, *Particulate Clouds, Dusts, Smokes, and Mists*, 2nd Edition, D. Van Nostrand, Inc., Princeton, 1964.

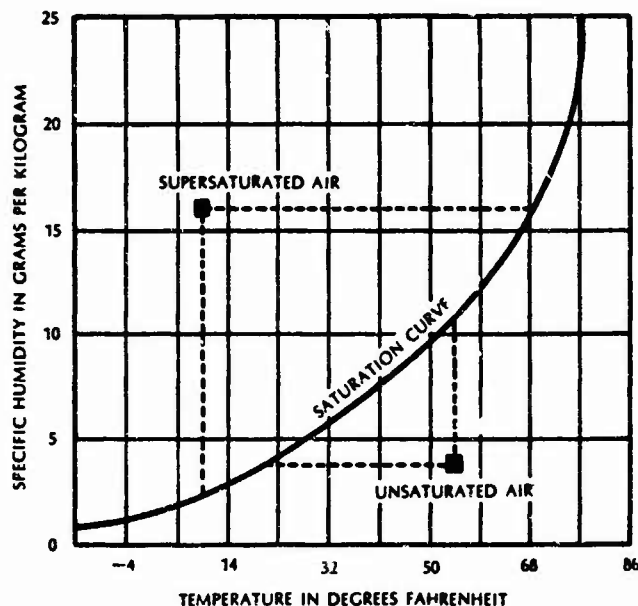


FIGURE 2. THE SATURATION CURVE

Air mass fogs can be subdivided into four general types: 1) advection, 2) radiation fogs, 3) advection-radiation fogs, and 4) upslope fogs. Advection fogs form when warmer air blows over a colder land or water surface. Thus, the warmer air gives off heat to the colder surface, thereby cooling the air to the dew point. The water vapor in the air condenses on the nuclei of salt, dust, or smoke even before the relative humidity reaches 100 per cent. The air does not tend to rise because it is being cooled and it then becomes dense, heavy, and stable. Examples of advection fogs are the following:

1. Land- and Sea-Breeze Fog: Characterized by warm, moist, land air passing over cold water. Typical of New England coast.
2. Sea Fog: This is similar to the land- and sea-breeze fog except that it arises from the cooling of sea air over a cold ocean current or cold coastal current. Typical of California coast in summer.

3. Tropical-Air Fog: This is caused by the gradual cooling of tropical air as it moves poleward over the ocean or over land. It is probably the most common type of fog over the open sea. Typical of the southeastern U.S. and east coast of the U.S.

4. Steam Fog: Steam fog, characterized by tufts of whirling smoke coming out of the water is caused by the passage of cold air over warmer water. In polar latitudes it is called arctic sea smoke.

Radiation fogs are different from advection fogs in that they form over land when the sky is clear, the wind is light, and the relative humidity is high near sunset. Since the relative humidity is high a slight cooling will result in a lowering of the temperature to the dew point. We have two kinds of radiation fogs.

1. Ground Fog: This is the simplest type, involving light winds, clear skies, and a surface temperature inversion. Typical of the Appalachian valleys.

2. High Inversion Fog: A winter time, land phenomenon resulting from more than a single night of cooling. This is typical of the tropical west coasts of continents as in California.

The third type of air mass fog is the advection-radiation fog. It is caused by nighttime radiational cooling of air that has moved inland from the sea during the day. Typical of the California coast or the Great Lakes during Fall.

The fourth type of air mass fog is the upslope or expansion fog. This involves the cooling of air in its dew point by adiabatic expansion as the air moves to higher elevations. It is typical of the Great Plains in the U.S.

There are three kinds of frontal fogs, prefrontal, post-frontal, and front-passage fogs.

1. Prefrontal Fog (warm front): This is characterized by rain falling into stable cooler air, evaporating and raising the dew point of the air to the condensation point. It is typical of the Mid- and North-Atlantic coast states in Winter; also the Appalachian valleys.

2. Post-Frontal (cold front): This fog is similar to the pre-frontal fog except that the associated precipitation band is much more restricted in area. It is typical of the Midwestern U.S. during polar air mass outbreaks.

3. Front-Passage Fog: This is a short lived fog that can form in various ways with the passage of a frontal zone.

Finally, we have the last category of fogs, the ice fog. It is caused primarily by man-made sources of moisture (engines runnings) at temperatures lower than about -30°C . Typical of the polar regions.

Having considered the general types of fogs and their formation we shall now investigate the size distribution of the droplets. When droplets begin to grow in size at the saturation point the growth proceeds at a regular rate. Neiburger and Chien [19] investigated this growth process and found that the size distribution of the particles changes as the fog ages and that the distribution becomes bimodal. This is illustrated in Figure 3. As time goes on and saturation and then supersaturation occurs the transition from haze to fog is quite rapid. As condensation takes place the particles coalesce and the fog size distribution develops a secondary peak in the 3 to 6 μm range.

The shape of the particles are assumed to be spherical since in a fog we have water droplets. Their composition, however, may vary since a fog may be contaminated by dust, smoke, or other matter in the immediate environment.

[19] M. Neiburger and C. W. Chien, Physics of Precipitation, Geophys. Monogr. No. 5, Washington, D.C., 1960, pp. 191-210.

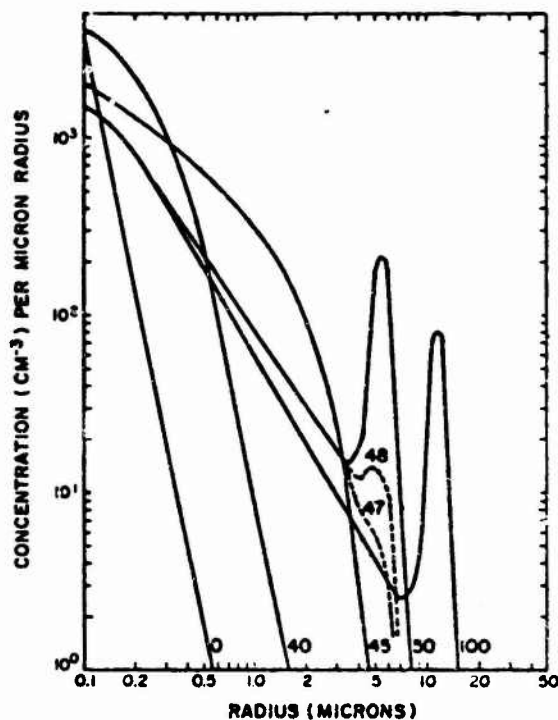


FIGURE 3. AEROSOL DISTRIBUTIONS AS A FUNCTION OF LAPSE TIME AFTER THE INITIATION OF THE CONDENSATION PROCESS. The times, in minutes, are indicated at the base of each curve after Neiburger and Chien (1960).

ATTENUATION OF RADIATION

In this section we shall investigate the interaction of visible and infrared radiation with a scattering and absorbing medium such as a haze or fog. Before a radiative-transfer model is developed we need to know the basic input parameters for the environment under consideration.

4.1 TRANSMITTANCE

The transmittance of a beam of radiation propagating through the atmosphere lies somewhere between zero and unity. For zero transmittance no direct radiation passes through the medium and for a value of one all the radiation passes through undiminished in intensity. We shall neglect gaseous absorption in this report because we are primarily interested in the scattering of radiation by gases and aerosols.

If an infinitesimal, narrow beam of monochromatic radiation propagates through a medium the intensity at a distance x from the source is

$$I_{\lambda}(x) = I_{\lambda}(0)T_{\lambda}(x) \quad (7)$$

where $I_{\lambda}(0)$ is the source intensity at wavelength λ and $T_{\lambda}(x)$ is the spectral transmittance at distance x . If the loss of radiation from the beam is total, i.e., complete absorption and/or scattering out of the beam then the fractional change in intensity is given by the following:

$$\frac{\Delta I_{\lambda}(x)}{I_{\lambda}(x)} = -\kappa_{\lambda}(x) \Delta x \quad (8)$$

where $\kappa_{\lambda}(x)$ is the probability per unit length for a net loss of radiation from the beam and Δx is the distance over which the fractional change occurs. As the length Δx approaches zero we have

$$\frac{dI_{\lambda}(x)}{dx} = -\kappa_{\lambda}(x) I_{\lambda}(x) \quad (9)$$

or

$$I_{\lambda}(x) = I_{\lambda}(0) e^{-\int_0^x \kappa_{\lambda}(x') dx'} \quad (10)$$

Thus, we see that the spectral transmittance $T_{\lambda}(x)$ is given by

$$T_{\lambda}(x) = e^{-\int_0^x \kappa_{\lambda}(x') dx'} \quad (11)$$

Hence, one of the problems is to determine the probability per unit length $\kappa_{\lambda}(x)$.

4.2 ATTENUATION COEFFICIENTS

The probability per unit length $\kappa_{\lambda}(x)$ is also called the volume extinction coefficient of the medium. In this section we shall see how this quantity is determined for various atmospheric states.

4.2.1 VISIBILITY

The spectral transmittance of a region of the atmosphere can be determined by measuring the intensity $I_{\lambda}(x)$ of a laser beam at distance x from the laser. There are times however, when it is not convenient to use lasers in field measurements. We would then like to have another method of estimating the extinction coefficient $\kappa_{\lambda}(x)$.

Equation (10) describes the intensity of a self-luminous object at distance x . If, in addition there is background radiation being received by a detector at distance x then we have

$$I_{\lambda}(x) = I_{\lambda}(0) T(x) + \int_0^{\infty} B_{\lambda}(x') \kappa_{\lambda}(x') T(x') dx' \quad (12)$$

where the integral represents the sum of all background radiation along a given path. These components are depicted in Figure 4. If the background radiation $B_\lambda(x')$ is independent of distance as it usually is in homogeneous atmospheres then Equation (12) becomes

$$I_\lambda(x) = I_\lambda(o)T(x) + B_\lambda[1-T(x)] \quad (13)$$

Expression (13) is quite general and applies to a variable path. If the luminous object is moved to a great distance then the intensity is just about due to the atmosphere, i.e.,

$$I_\lambda(x) \rightarrow B_\lambda \quad \text{as } x \rightarrow \infty \quad (14)$$

If the background is defined as the atmosphere then the contrast can be defined as

$$C = \frac{I_\lambda(o) - I_\lambda(x)}{I_\lambda(x)} = \frac{(I_\lambda(o) - B_\lambda)[1-T(x)]}{I_\lambda(o)T(x) + B_\lambda[1-T(x)]} \quad (15)$$

Now, if an intrinsic contrast C_o is defined as

$$C_o = \frac{I_\lambda(o) - B_\lambda}{B_\lambda} \quad (16)$$

then

$$C = C_o T_c \quad (17)$$

where the contrast transmittance T_c is

$$T_c = \left[1 + \frac{I_\lambda(o)}{B_\lambda} - \frac{T(x)}{1-T(x)} \right]^{-1} \quad (18)$$

Thus, by measuring the contrast the distance x can be determined. For the case of a black object measured against the atmosphere we have according to Equation (13)

$$I_\lambda(x) = B_\lambda[1-T(x)] \quad (19)$$

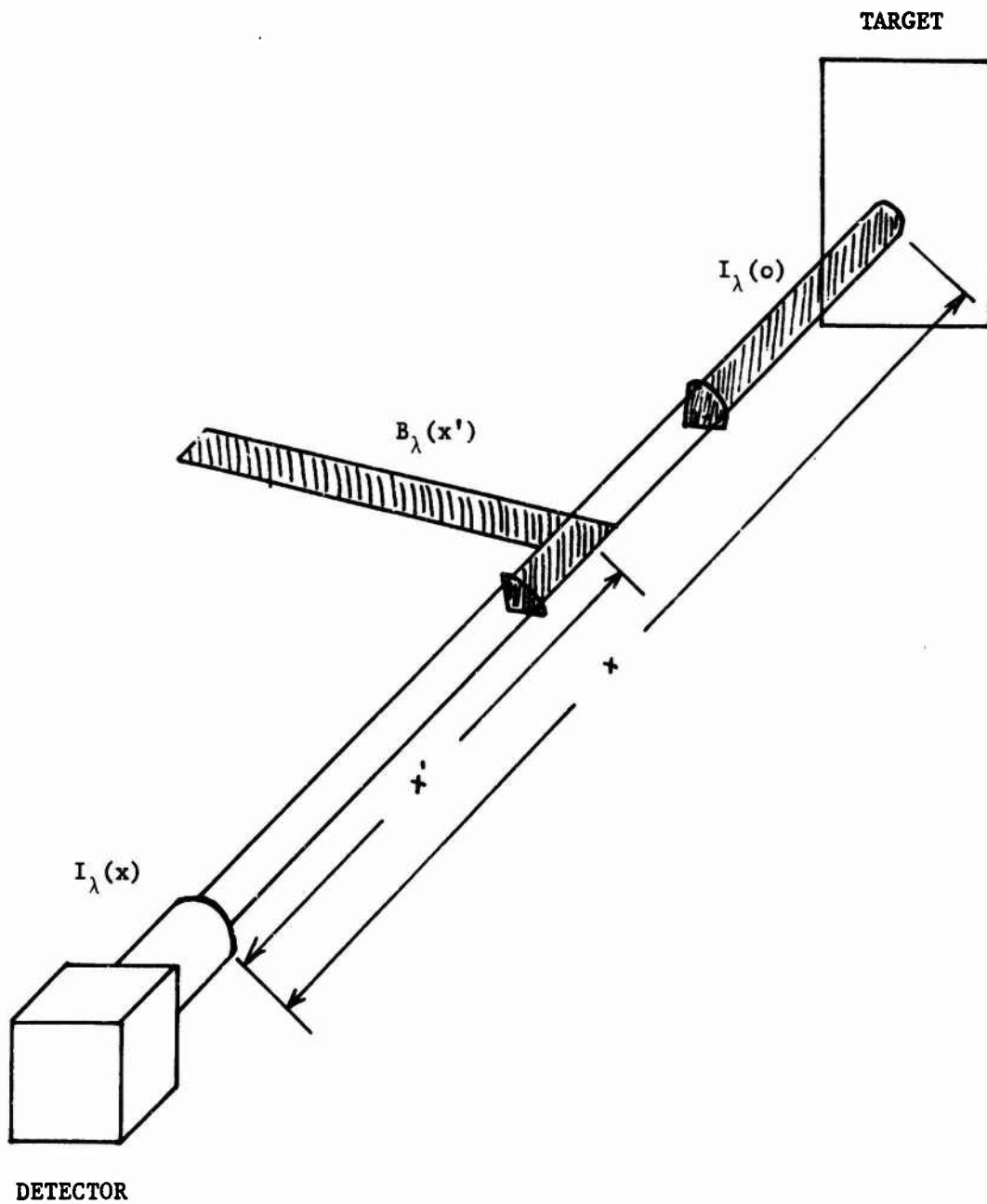


FIGURE 4. DETECTION OF DIRECT AND BACKGROUND RADIATION

Thus, the contrast is

$$C = \frac{I_{\lambda}(x) - B_{\lambda}}{B_{\lambda}} \quad (20)$$

or

$$C = T(x) = e^{-\int_0^x \kappa(x') dx} \quad (21)$$

Koschmieder [20] defined the limiting contrast for the eye as 0.02. In that case the distance at which the contrast is 0.02 for a constant atmosphere is

$$V = \frac{3.912}{\kappa} \quad (22)$$

where V is the so-called visual range and κ is the volume extinction coefficient at a wavelength of 0.55 μm . Figure 5 illustrates this variation of visual range with κ . The ultimate visual range is that for an aerosol free atmosphere. This value is 336 km. More realistic cases are those for smaller visual ranges. The fog regime begins rather abruptly near a visual range of 1 kilometer. As we shall see in a later section a mist regime may also be defined in-between the haze and fog.

4.2.2 HAZES

Knowing the gaseous composition of the atmosphere one can calculate the Rayleigh extinction coefficient at any wavelength. This was done by one of the authors (Turner) for any visible and near-infrared wavelength and as a function of altitude. A correction was also made for variable terrain altitudes. The Rayleigh extinction coefficient is

$$\kappa_R(z) = \sigma_R N_R(z) \quad (23)$$

[20] H. Koschmieder, Theorie der horizontalen Sichtweite, Beitr. Phys. freien Atm. 12, 1924, pp. 33-53.

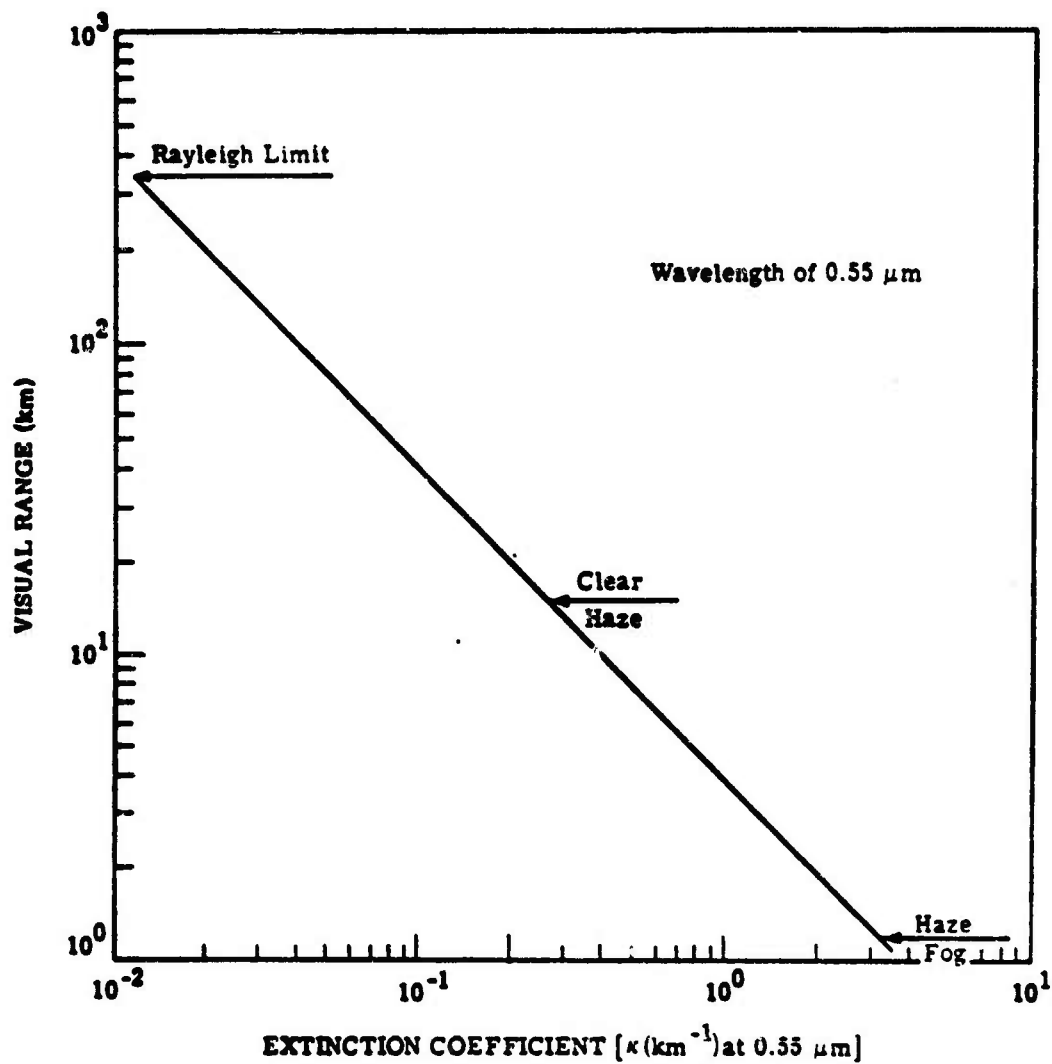


FIGURE 5. VARIATION OF VISUAL RANGE WITH EXTINCTION COEFFICIENT

where σ_R is the Rayleigh cross section and $N_R(z)$ is the molecular number density. The cross section has the well-known $1/\lambda^4$ wavelength dependence. For a haze there is more scattering but since the scattering centers are large compared to the wavelength, many orders of scattering contribute to the total and there is little dependence on wavelength. For hazes the spectral dependence is approximately $\lambda^{-1.3}$. Figure 6 illustrates the spectral dependence of the extinction coefficient for hazes and clouds. These coefficients were calculated by Deirmendjian [11] for water spheres.

The dependence on altitude is more complicated. Elterman [21] collected data on various experiments to determine the extinction coefficients for hazy atmospheres. The results are presented in Figure 7. Here we see a gradual decrease with altitude for most of the experiments. Elterman [22] has also modeled hazes in terms of altitude, visual range, and wavelength making use of experimental data at a known visual range. The resulting compilation is what we shall use in the calculation of the natural radiation field.

Hence, we can say that the model described above characterizes a general "standard" haze but there can be large variations from the model in individual cases. In a specific situation one should measure either the spectral transmittance or the visual ranges in order to define the state of the atmosphere.

4.2.3 FOGS

Clouds and fogs are made up of particles which are much larger than those for hazes. As a result, the scattering is usually less selective, or dependent upon wavelength. Arnulf et al. [23] presented data on fogs

[21] L. Elterman, U.V., Visible, and IR Attenuation for Altitudes to 50 km, 1968, AFCRL Report No. 68-0153, Office of Aerospace Research.

[22] L. Elterman, Vertical-Attenuation Model with Eight Surface Meteorological Ranges 2 to 13 Kilometers, AFCRL Report No. 70-0200, 1970, Office of Aerospace Research.

[23] A. Arnulf, J. Bricard, E. Curé, and C. Véret, Transmission by Haze and Fog in the Spectral Region 0.35 to 10 Microns, J. of the Opt. Soc. of Amer., Vol. 47, No. 6, 1957, pp. 491-498.

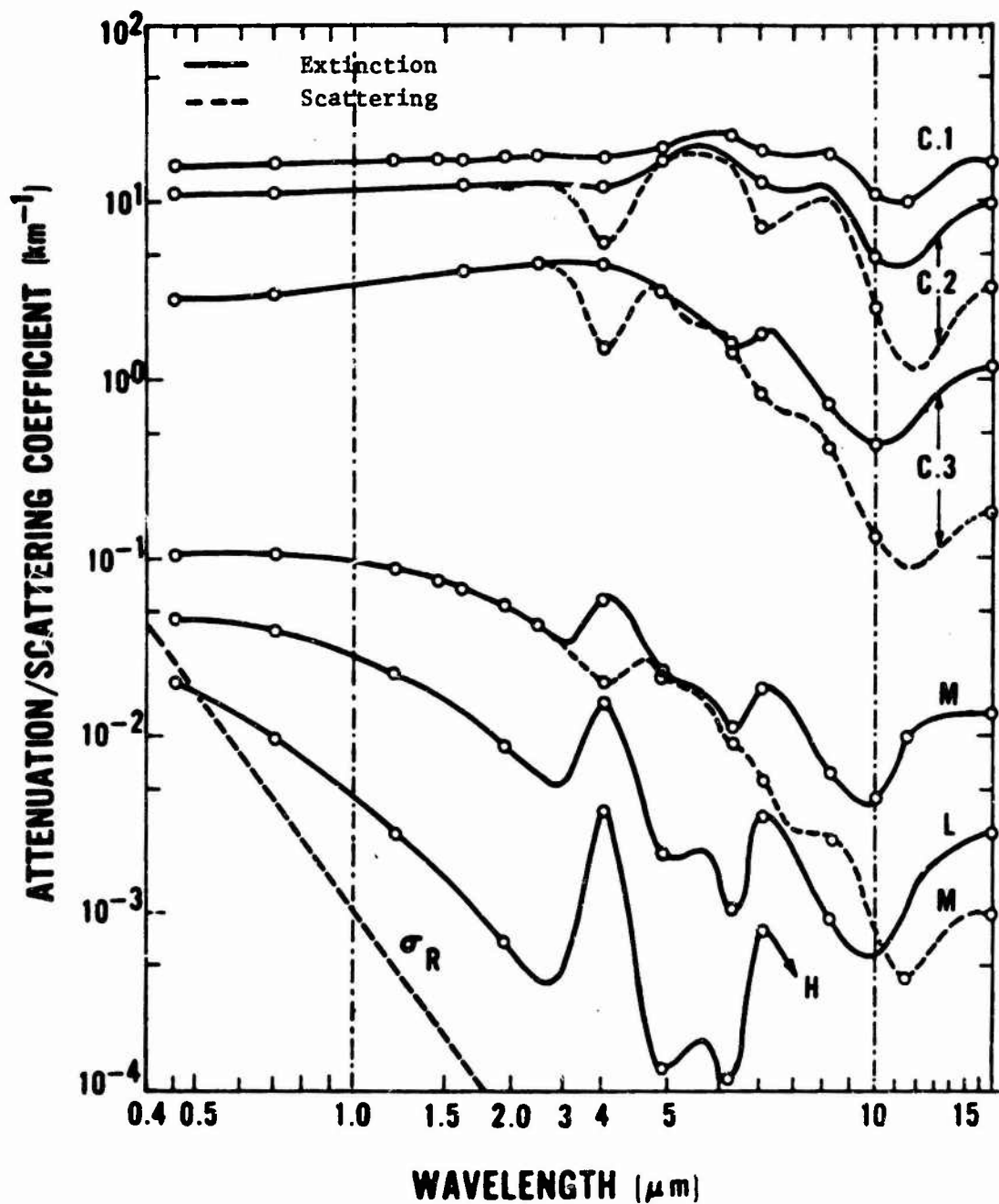


FIGURE 6. SPECTRAL ATTENUATION AND SCATTERING COEFFICIENTS FOR VARIOUS HAZE (L,M,H) AND CLOUD (C₁,C₂,C₃) MODELS (ADAPTED FROM DEIRMENDJIAN).

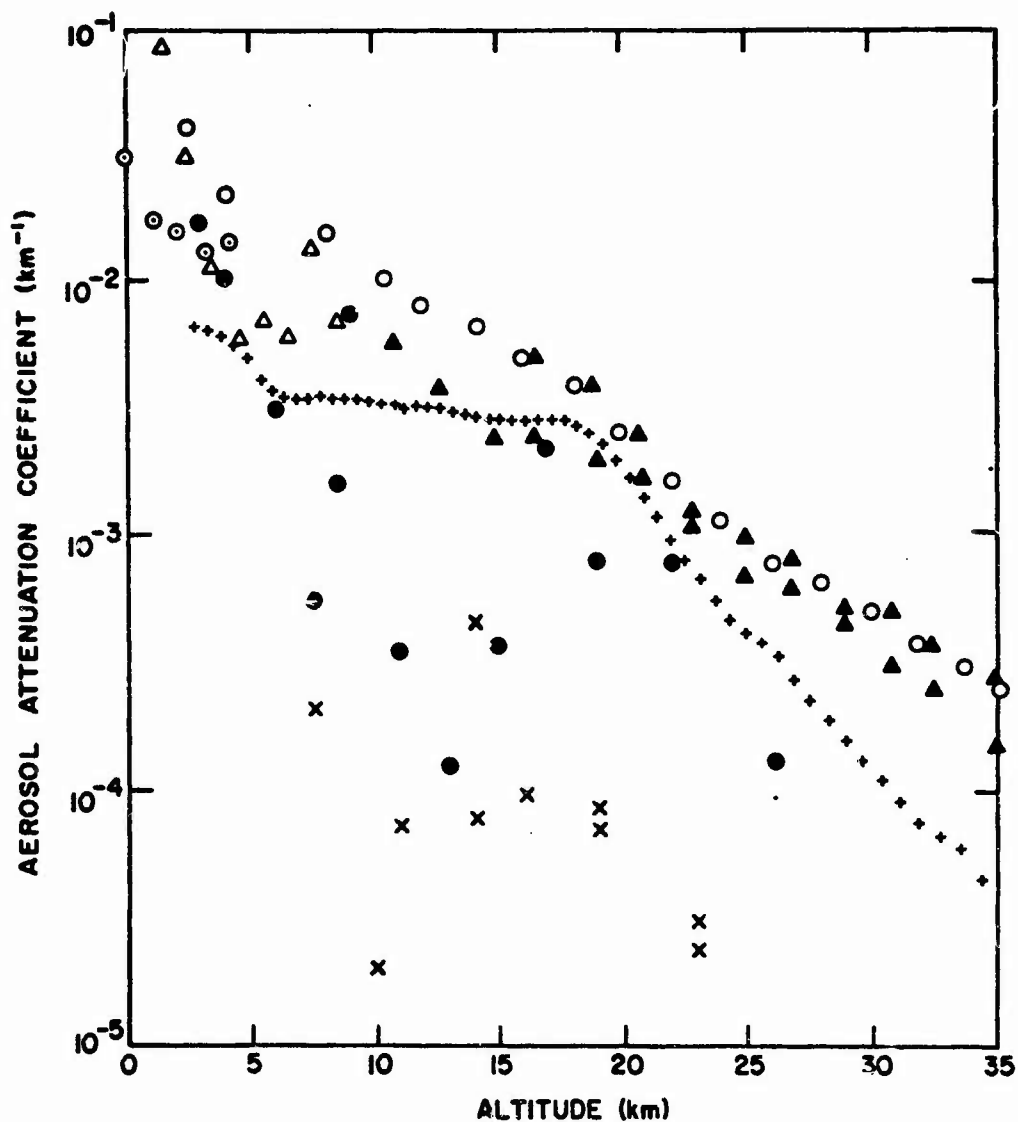


FIGURE 7. AEROSOL ATTENUATION COEFFICIENTS VS ALTITUDE AT $\lambda_1 = 0.55\mu$

Comparison of results:

- XXXX solar aureole, 2 balloon flights, Newkirk and Eddy (1964);
- ΔΔΔΔ solar radiation measured from aircraft, mean of 8 flights, Penndorf (1954);
- ++++ searchlight probing, mean of 105 profiles, Elterman (1966a) and (1966b);
- balloon integrating nephelometer, mean of 14 flights, Crosby and Koerber (1962);
- solar radiation measured from balloons, mean of 3 flights, Kondratiev et al. (1967);
- ▲▲▲▲ spacecraft horizon photography, analysis of 4 frames, Rozenberg (1966), Feoktistov (1965);
- searchlight probing, mean for 5 nights, Rozenberg (1966)

of various types. The extinction coefficients (density per kilometer) for four fogs is illustrated in Figures 8, 9, 10, and 11. It should be noted that selective fogs are similar to hazes in that there is a definite spectral dependence whereas for the stable fogs there is essentially no spectral dependence in the visible and near infrared regions, in fact, the transmission diminishes in the near infrared in some cases. Only beyond $3.7 \mu\text{m}$ does the extinction coefficient begin to decrease. By measuring droplets in a fog and comparing these measurements with calculations for various fog droplet size distributions Eldridge [24] determined four basic fog extinction coefficients. These are depicted in Figure 12. Hence, we can summarize the spectral dependence of all the coefficients in Figure 13. These results are taken from Deirmendjian [25]. The greatest change is for a pure, Rayleigh atmosphere, and as the medium develops a haze the spectral dependence is much less pronounced. For a fog there is little dependence on wavelength in the visible and near infrared.

In order to calculate the volume extinction coefficient we must realize that the total coefficient is made up of two parts, that due to the gaseous component are that due to the particles; thus

$$\kappa(\lambda, r) = \kappa_R(\lambda, r) + \kappa_A(\lambda, m, r) \quad (24)$$

where $\kappa_R(\lambda, r)$ is the Rayleigh coefficient at position in space r and for wavelength λ and $\kappa_A(\lambda, m, r)$ is the aerosol coefficient at the same point and same wavelength but for a composition denoted by the refractive index m which is wavelength dependent. As we have seen the Rayleigh component is easy to calculate since it only depends on the gaseous density of the atmosphere and the wavelength. The aerosol extinction coefficient is

[24] R. G. Eldridge, Haze and Fog Aerosol Distributions, J. of Atmos. Sciences, 1966, pp. 605-613.

[25] D. Deirmendjian, Quart. Journal Royal Meteorol. Soc. 86, 371, (1960).

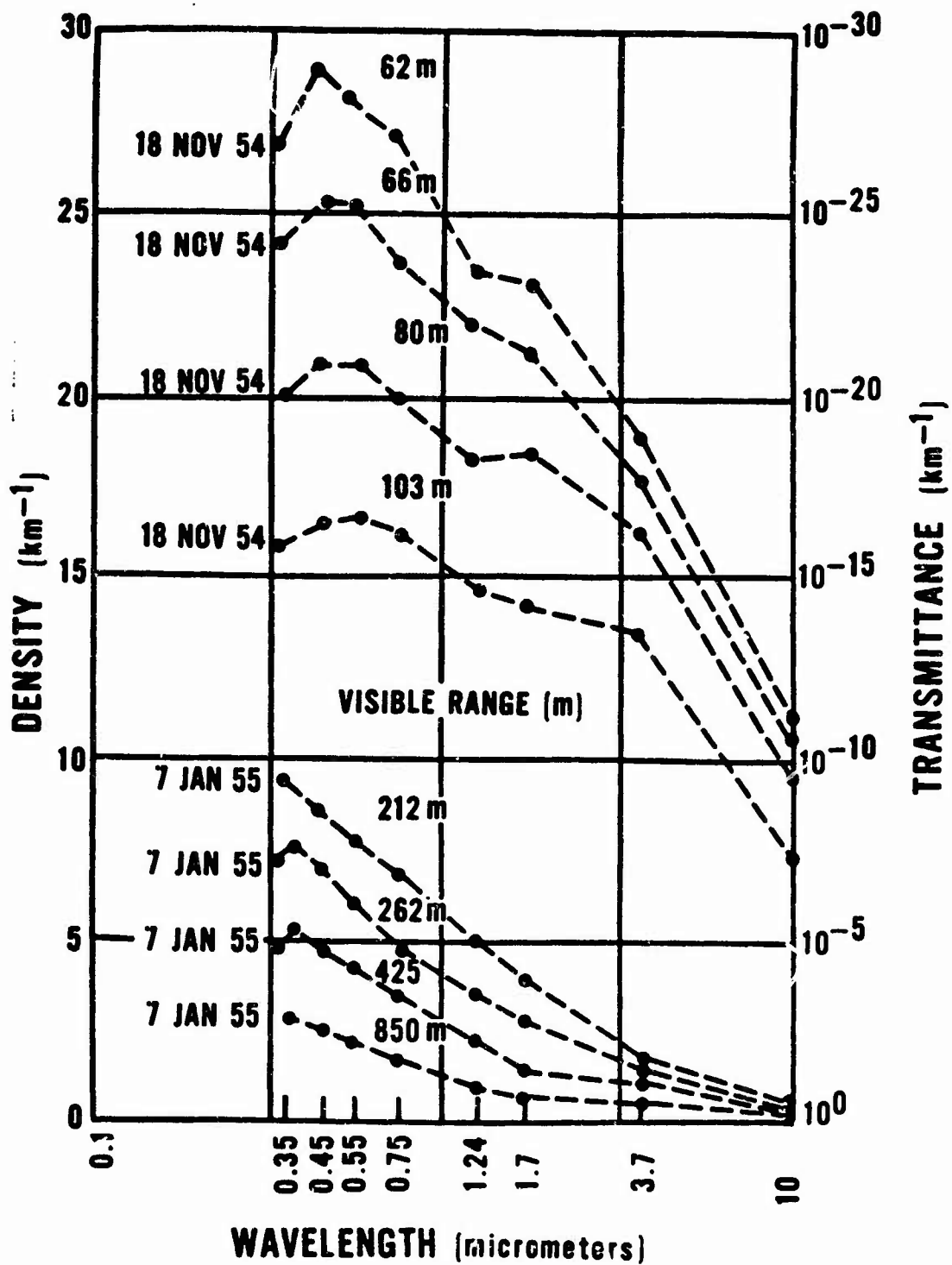


FIGURE 8. ATMOSPHERIC TRANSMITTANCE SPECTRA FOR SELECTIVE FOGS AS MEASURED BY ARNULF ET AL.

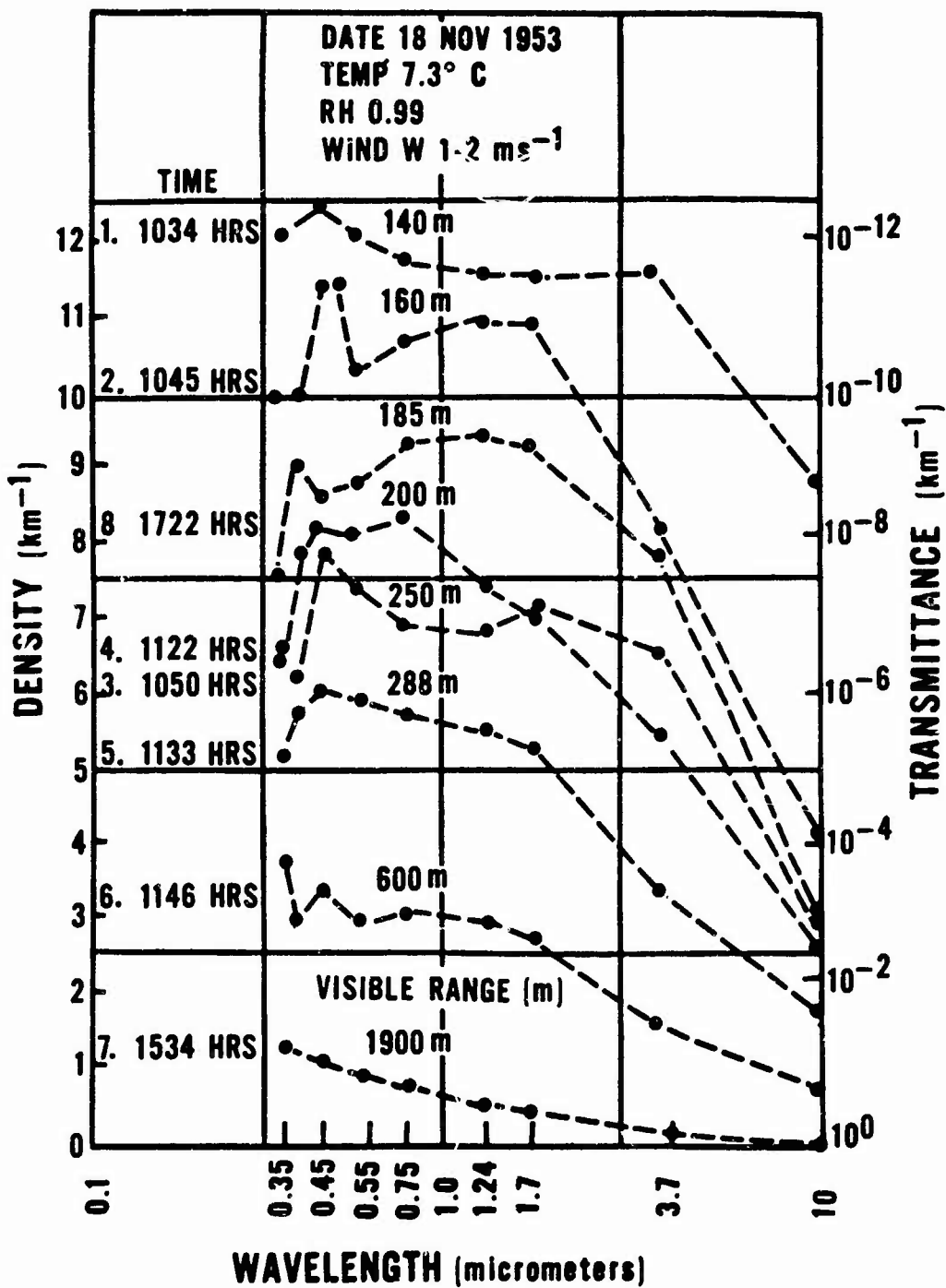


FIGURE 9. ATMOSPHERIC TRANSMITTANCE SPECTRA FOR EVOLVING FOGS AS MEASURED BY ARNULF ET AL.

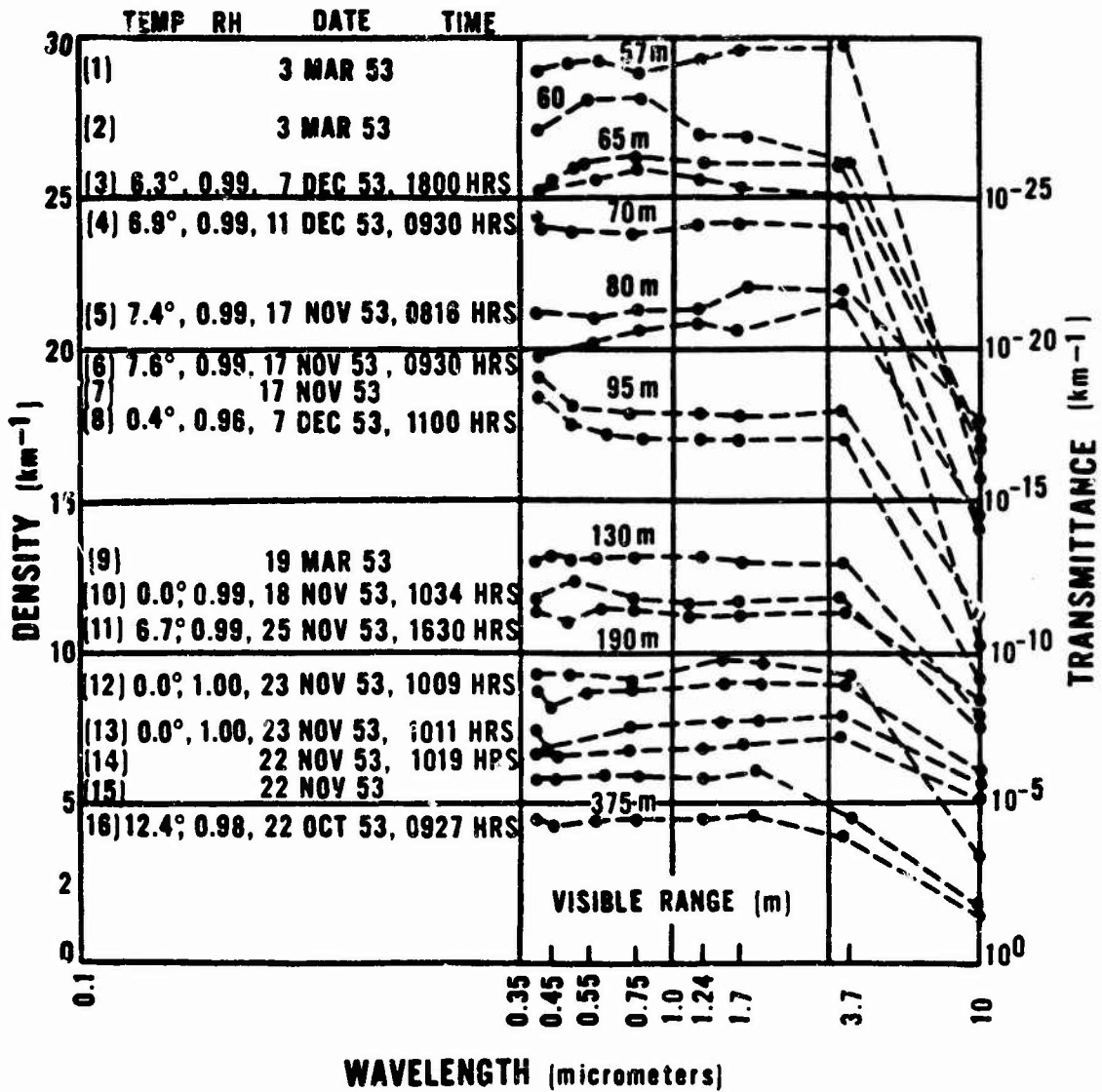


FIGURE 10. ATMOSPHERIC TRANSMITTANCE SPECTRA FOR STABLE FOGS, TYPE 1, AS MEASURED BY ARNULF ET AL.

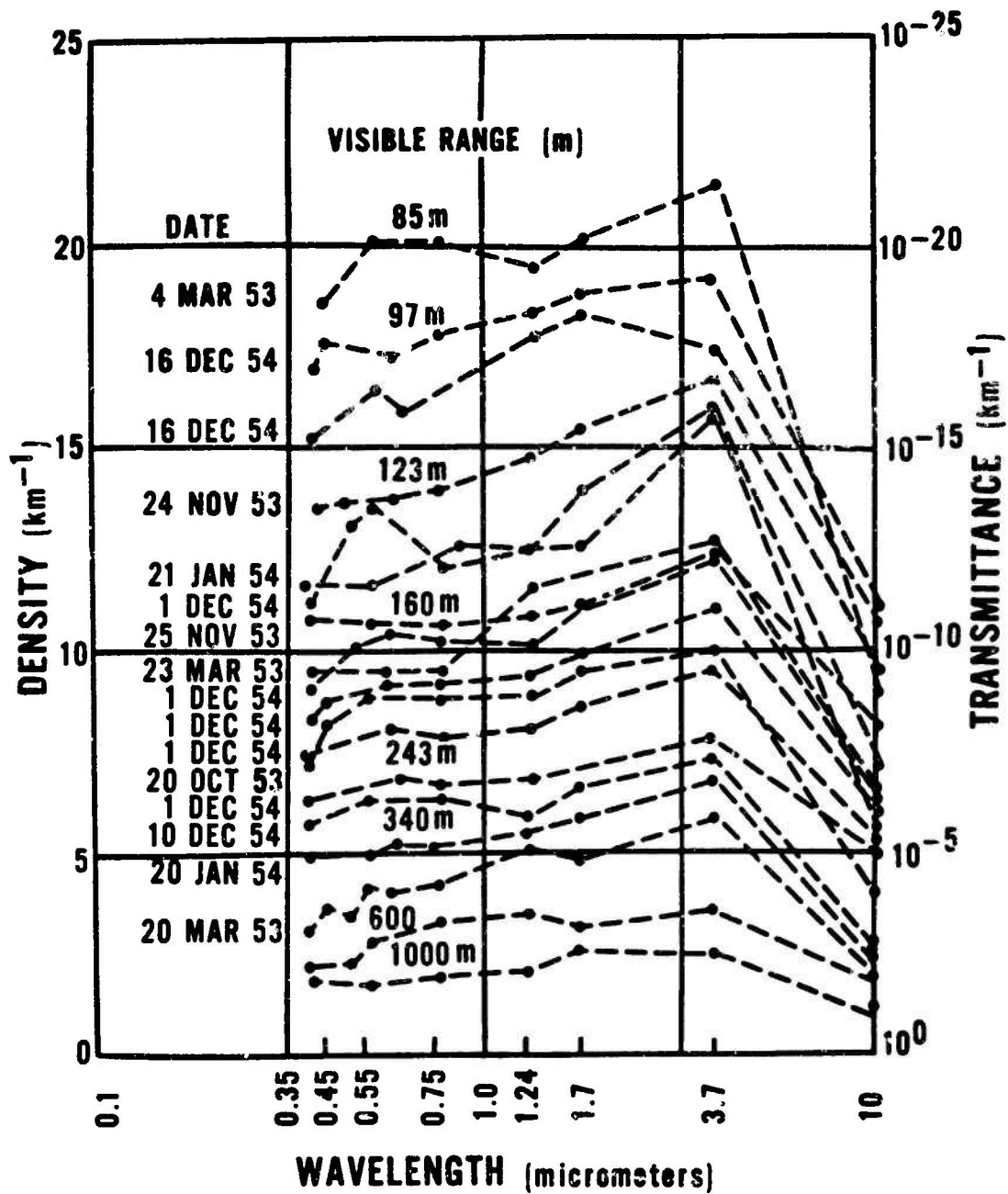


FIGURE 11. ATMOSPHERIC TRANSMITTANCE SPECTRA FOR STABLE FOGS, TYPE 2, AS MEASURED BY ARNULF ET AL.

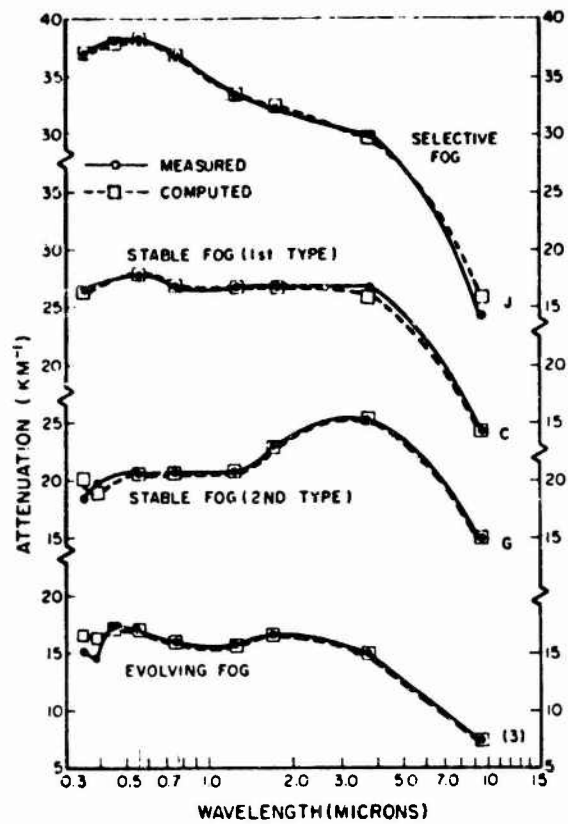


FIGURE 12. MEASURED AND COMPUTED FOG SPECTRAL ATTENUATIONS ILLUSTRATING GOODNESS OF FIT

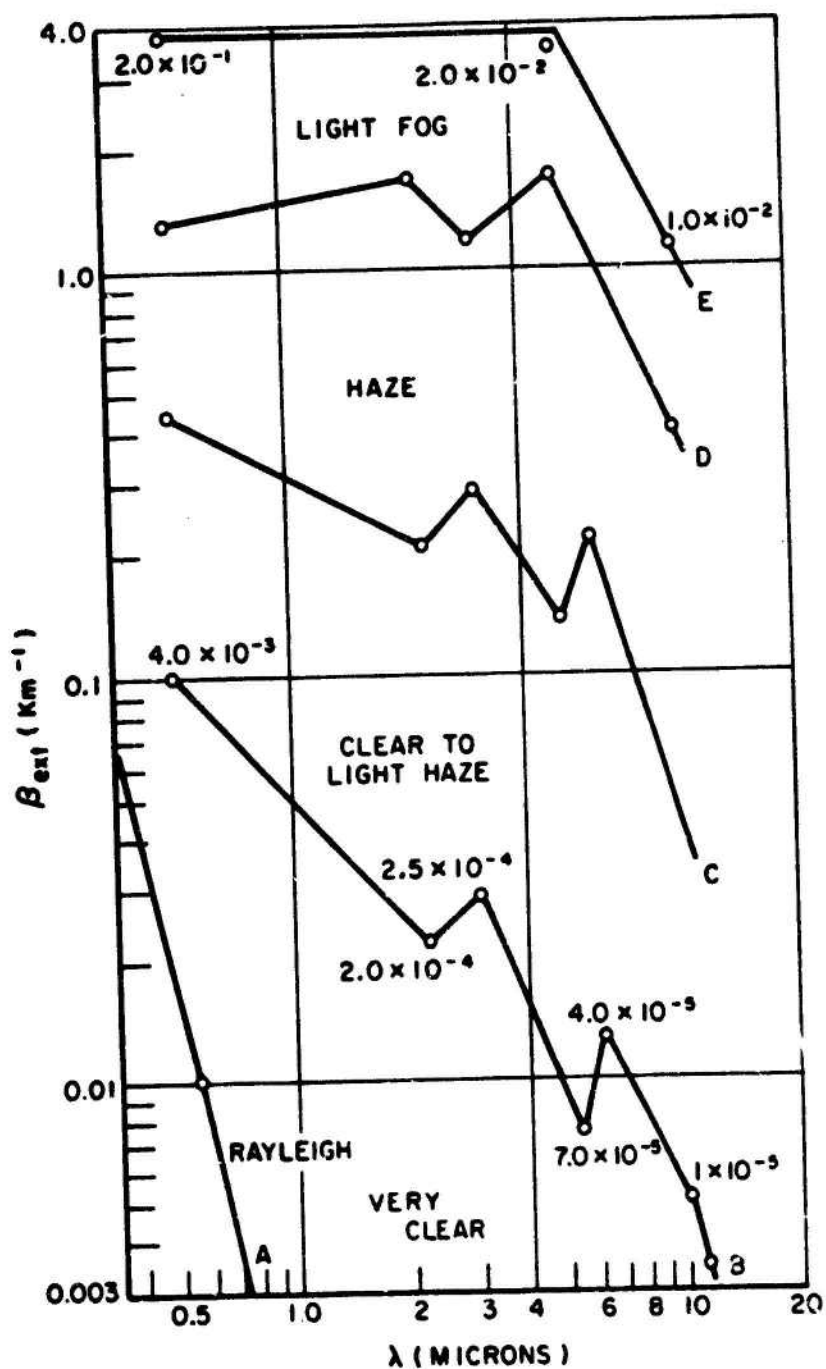


FIGURE 13. TYPICAL VALUES FOUND FOR ATMOSPHERIC EXTINCTION COEFFICIENT VS WAVELENGTH. Indicated values for curves B and E are $P(180^\circ)/4\pi \cdot \beta_{sca}$.

however, more difficult to calculate. If uniform spherical particles are assumed with a known refractive index then we can calculate the cross sections. The scattering of electromagnetic radiation by homogeneous dielectric spheres is called MIE scattering. In principle, determining the scattering and absorption cross-sections and the scattering phase function is straightforward. First, the wave equation is solved inside and outside the sphere; then the solutions are match at the boundary to determine the constants. The intensity of the radiation scattered into an angle χ is given by

$$I = \frac{\lambda^2}{4\pi^2 R^2} \frac{|S_1|^2 + |S_2|^2}{2} I_0 \quad (25)$$

where R is the distance from the sphere, and I_0 is the incident intensity. The scattering amplitudes $|S_1|^2$ and $|S_2|^2$ are given by

$$S_1 = \sum_{\ell=1}^{\infty} \frac{2\ell+1}{\ell(\ell+1)} [a_{\ell} \pi_{\ell} + b_{\ell} \tau_{\ell}] \quad (26)$$

$$S_2 = \sum_{\ell=1}^{\infty} \frac{2\ell+1}{\ell(\ell+1)} [a_{\ell} \tau_{\ell} + b_{\ell} \pi_{\ell}]$$

In Equation (26) a_{ℓ} and b_{ℓ} , which are the Mie coefficients, are given by

$$a = \frac{\psi_{\ell}'(mx) \psi_{\ell}(x) - m \psi_{\ell}(mx) \psi_{\ell}'(x)}{\psi_{\ell}'(mx) \zeta_{\ell}(x) - m \psi_{\ell}(mx) \zeta_{\ell}'(x)} \quad (27)$$

$$b = \frac{m \psi_{\ell}'(mx) \psi_{\ell}(x) - \psi_{\ell}(mx) \psi_{\ell}'(x)}{m \psi_{\ell}'(mx) \zeta_{\ell}(x) - \psi_{\ell}(mx) \zeta_{\ell}'(x)} \quad (28)$$

where m and x , respectively, are the complex refractive index and size parameters -- that is, $m = m_1 - im_2$ and $x = 2\pi r/\lambda$ when r is the particle radius. The functions ψ_ℓ and ζ_ℓ are the Riccati-Bessel functions, and a prime indicates differentiation with respect to the argument. The π_ℓ and τ_ℓ functions are given by

$$\pi_\ell(\cos \chi) = \frac{dP_\ell(\cos \chi)}{d \cos \chi} \quad (29)$$

and

$$\tau_\ell(\cos \chi) = \cos \chi \pi_\ell(\cos \chi) - \sin \chi \frac{d\pi_\ell(\cos \chi)}{d \cos \chi} \quad (30)$$

where $P_\ell(\cos \chi)$ is a Legendre polynomial. The scattering cross-section is

$$\sigma_s(\lambda, r, m) = \pi r^2 Q_s(x, m) = \frac{\lambda^2}{2\pi} \sum_{\ell=1}^{\infty} (2\ell + 1) [|a_\ell|^2 + |b_\ell|^2] \quad (31)$$

where $Q_s(x, m)$ is called the scattering efficiency factor. The total (scattering plus absorption) cross-section is

$$\sigma_t(\lambda, r, m) = \pi r^2 Q_t(x, m) = \frac{\lambda^2}{2\pi} \sum_{\ell=1}^{\infty} (2\ell + 1) \operatorname{Re}(a_\ell + b_\ell) \quad (32)$$

where $Q_t(x, m)$ is the total efficiency factor. Likewise, the absorption cross-section is then

$$\sigma_a(\lambda, r, m) = \sigma_t(\lambda, r, m) - \sigma_s(\lambda, r, m) \quad (33)$$

with a corresponding efficiency factor $Q_a(x, m)$. As in the Rayleigh case, a scattering phase function can be defined:

$$P(\cos \chi) = \frac{1}{2\pi x^2 Q_s(x, m)} [|S_1|^2 + |S_2|^2] \quad (34)$$

Calculating all the functions given above for various refractive indices and size parameters is quite involved. Nevertheless, computer programs have been written which allow the performance of this analysis. Having obtained a program written by J. V. Dave, we used it to calculate the cross-sections and phase functions. For example, we have calculated the scattering efficiency factor for homogeneous spheres of refractive indices $m = 1.29$, $1.29 - 0.0465i$, and $1.28 - 1.37i$. The results are shown in Figure 14. It should be noted that the efficiency factor is greatest for the real index (that is, when there is no absorption) and decreases with increasing imaginary index. The absorption efficiency factor has also been calculated for $m = 1.28 - 0.0465i$ and $1.28 - 1.37i$. Here the efficiency factor is large for a high imaginary index and small particles, as illustrated in Figure 15. Finally, the total efficiency factor is shown in Figure 16 for the same set of refractive indices. Thus, it can be seen that efficiency factors vary strongly for different refractive indices and size parameters.

Knowing the cross-sections, one can then calculate the scattering, absorption, and extinction coefficients by multiplying the cross-sections by the particle number density. For real atmospheric conditions characterized by haze, fogs, and dusts, there is a distribution of particle sizes. (One distribution, characterized in Section 3.2, is the modified gamma distribution.) Thus, for a polydispersion, one must integrate over particle size to obtain the absorption, scattering, and extinction coefficients:

$$\alpha_A(\lambda, m, z) = \int_0^{\infty} \sigma_{a,A}(\lambda, m, r)n(z, r)dr. \quad (35)$$

$$\beta_A(\lambda, m, z) = \int_0^{\infty} \sigma_{s,A}(\lambda, m, r)n(z, r)dr \quad (36)$$

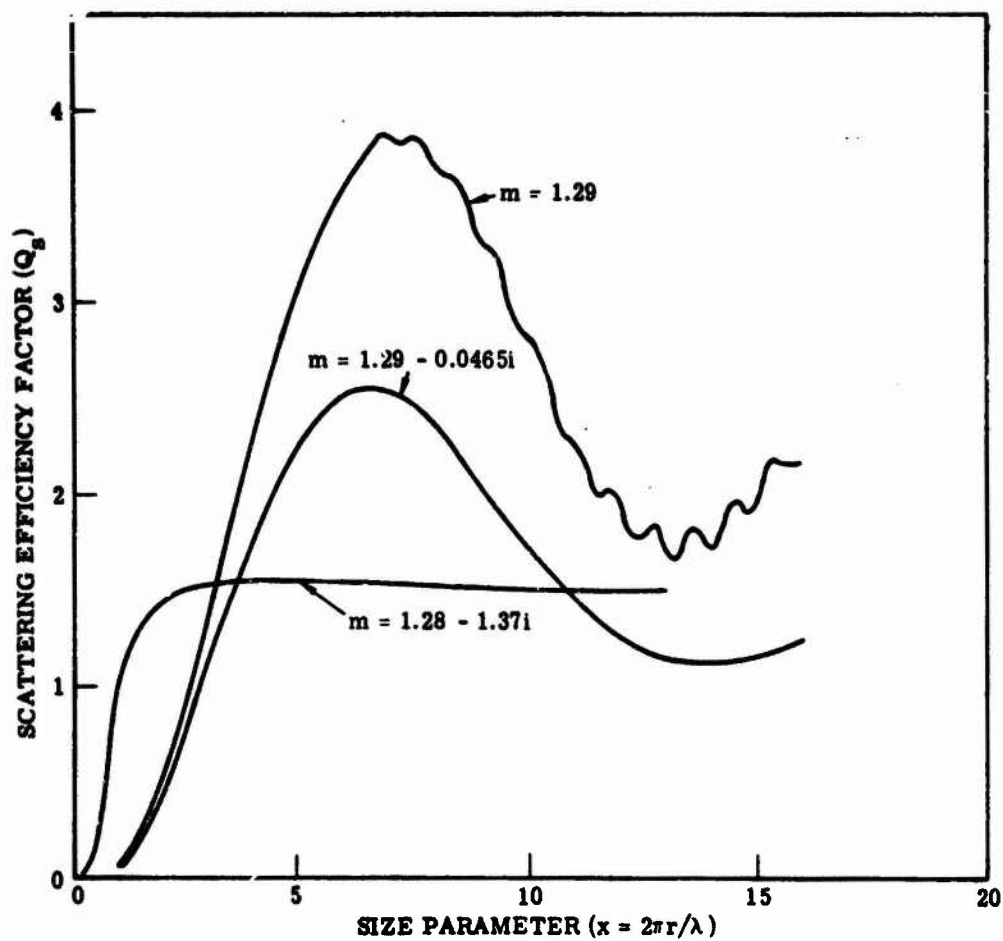


FIGURE 14. SCATTERING EFFICIENCY FACTOR FOR HOMOGENEOUS SPHERES OF COMPLEX REFRACTIVE INDEX m

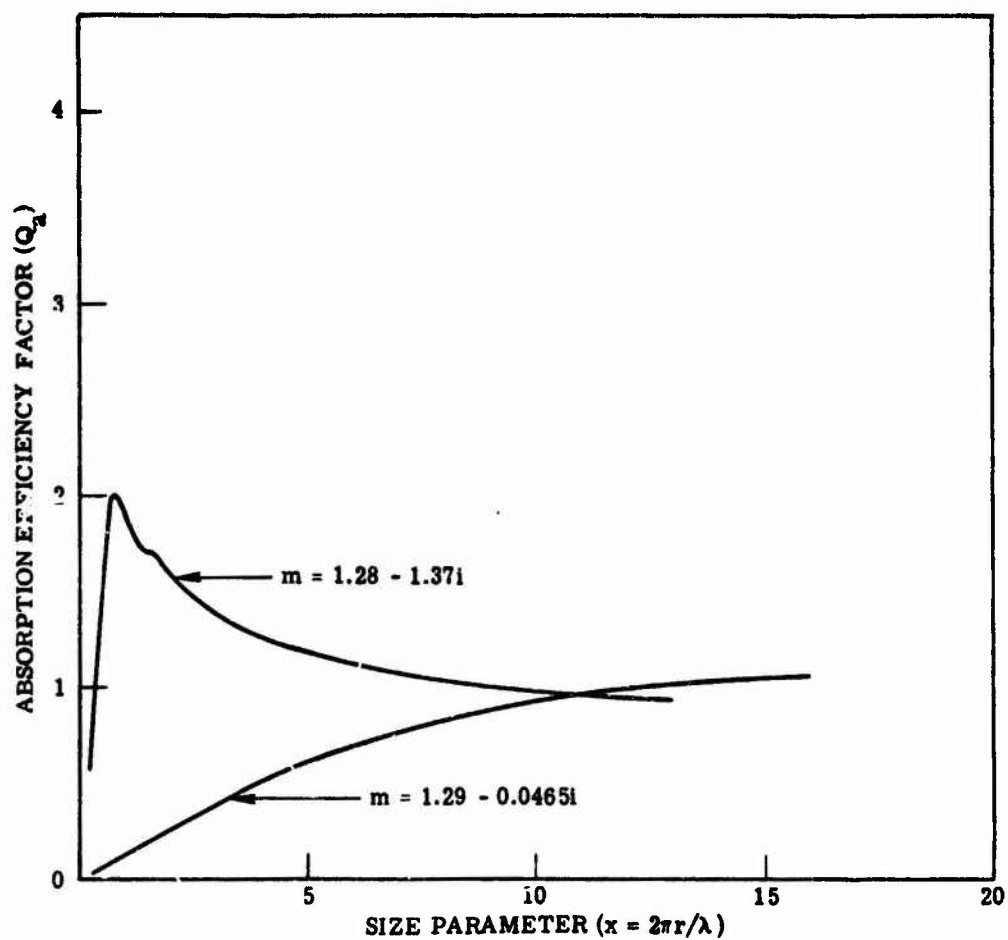


FIGURE 15. ABSORPTION EFFICIENCY FACTOR FOR HOMOGENEOUS SPHERES OF COMPLEX REFRACTIVE INDEX m

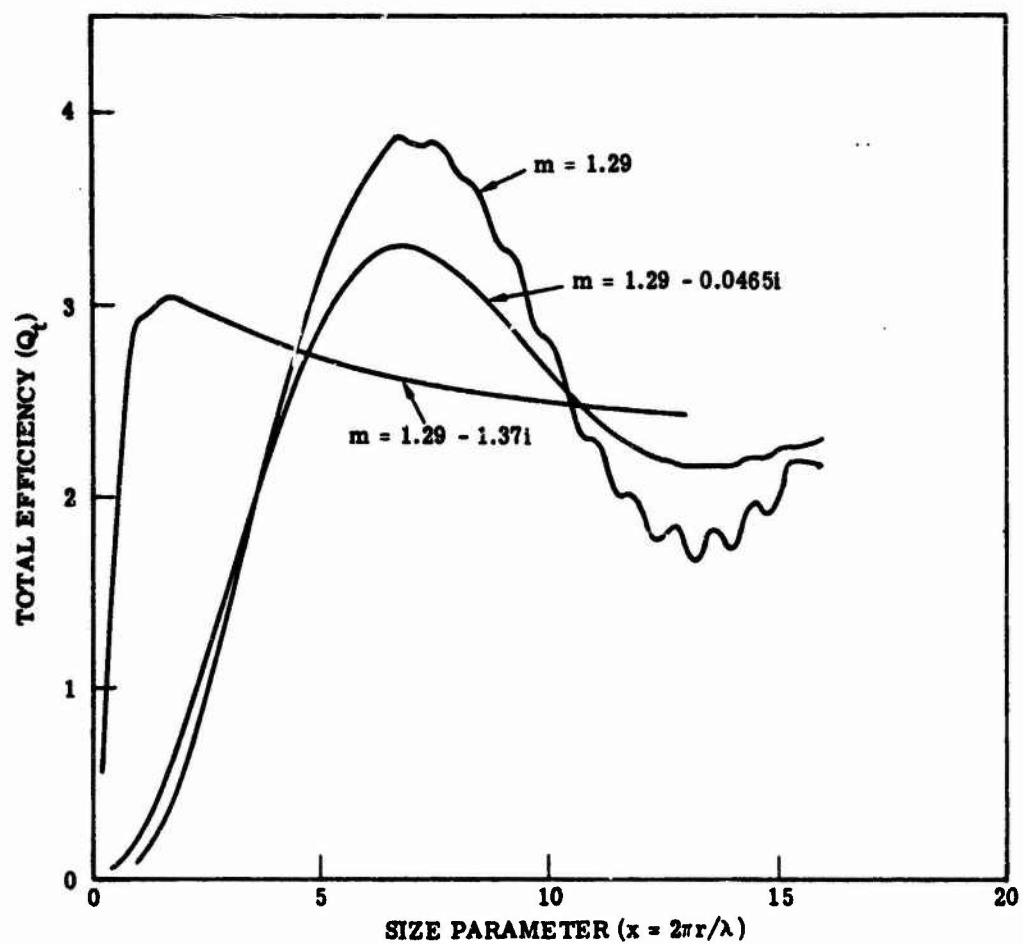


FIGURE 16. TOTAL EFFICIENCY FACTOR FOR HOMOGENEOUS SPHERES OF COMPLEX REFRACTIVE INDEX m

$$\kappa_A(\lambda, m, z) = \int_0^{\infty} \sigma_{t,A}(\lambda, m, r) n(z, r) dr \quad (37)$$

where α , β , and κ denote absorption, scattering, and extinction coefficients

A designates aerosol

$n(z, r)$ is the aerosol-particle number density at altitude z for particles in size range Δr at size r

The number density is normalized as follows:

$$N(z) = \int_0^{\infty} n(z, r) dr \quad (38)$$

where $N(z)$ is just the total number density. Likewise, the corresponding coefficients for molecular scattering can be found. The scattering cross-section is well known and the absorption cross-section is usually taken to be that for ozone in the visible spectral region. Thus, we have for the complete atmosphere:

$$\alpha(\lambda, m, s, z) = \alpha_R(\lambda, z) + \alpha_A(\lambda, m, s, z) \quad (39)$$

$$\beta(\lambda, m, s, z) = \beta_R(\lambda, z) + \beta_A(\lambda, m, s, z) \quad (40)$$

$$\kappa(\lambda, m, s, z) = \kappa_R(\lambda, z) + \kappa_A(\lambda, m, s, z) \quad (41)$$

where we have shown the explicit dependence on a complex refractive index m and a particular size distribution s .

It is sometimes useful to deal with an average cross-section for aerosols. Assuming that the size distribution is altitude-independent, we can write Equations (35), (36), and (37) as

$$\alpha_A(\lambda, m, z) = N(z) \bar{\alpha}_{a,A}(\lambda, m) \quad (42)$$

$$\beta_A(\lambda, m, z) = N(z) \bar{\sigma}_{s,A}(\lambda, m) \quad (43)$$

$$\kappa_A(\lambda, m, z) = N(z)\bar{\sigma}_{t,A}(\lambda, m) \quad (44)$$

where

$$\bar{\sigma}_{i,A}(\lambda, m) = \int_0^{\infty} \sigma_{i,A}(\lambda, m, r)\psi(r)dr \quad (45)$$

in which the function $\psi(r)$ is normalized to 1 and the index i can indicate a , s , or t . We have computed many values of the average cross-sections for homogeneous spheres of various refractive indices and size distributions. The results of this analysis will be presented later.

The angular scattering properties of the spherical particles can also be calculated using Mie theory. We will not go into the details of this analysis here. There are several excellent treatises on this subject, van de Hulst [26], Kerker [27], and Deirmendjian [11]. A typical phase function or differential scattering cross section is depicted in Figure 17 for the case of a polydisperse collection of cloud or fog particles. As one can see the radiation is sharply peaked in the forward direction. It is this anisotropy which presents great difficulties in the mathematical analysis of radiative-transfer.

Since fogs are composed of water droplets it seems natural to relate the visual range to the total water content of a fog. It was noted by Trabert [28] in 1901 that the visual range is related to water content w by the simple relation

$$V = Cr/w \quad (46)$$

[26] H. C. van de Hulst, *Light Scattering by Small Particles*, John Wiley and Sons, 1957.

[27] M. Kerker, *The Scattering of Light and Other Electromagnetic Radiation*, Academic Press, 1969.

[28] W. Trabert, *Die Extinction des Lichtes in einem truben Medium (Sichtweite in Wolken)*, Meteor. Z., 18, pp. 518-525, 1901.

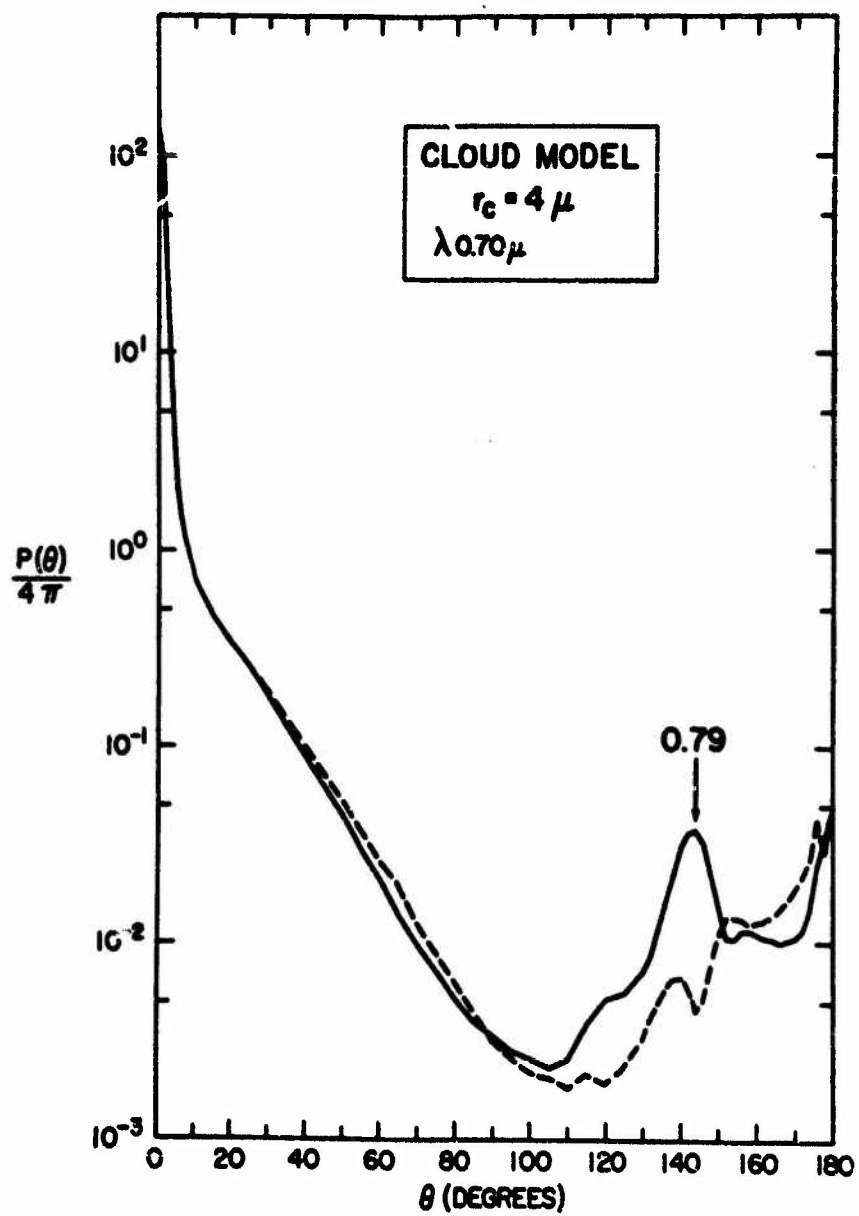


FIGURE 17. SINGLE-SCATTERING POLYDISPERSE PHASE FUNCTION

where C is a constant and r is the droplet radius. This follows from the fact that the extinction coefficient κ is

$$\kappa_{\lambda} = N \pi r^2 Q(\lambda, r) \quad (47)$$

and the visual range is

$$V = \frac{3.912}{\kappa_{\lambda_0}} \quad (48)$$

where $\lambda_0 = 0.55 \mu\text{m}$. Now from Mie theory we saw that for very large particles $Q(\lambda, r) \rightarrow 2$ and hence κ_{λ} is independent of wavelength. Thus,

$$V = \frac{3.912}{2\pi N r^2} \quad (49)$$

Now, the water content w is given by

$$w = \frac{4}{3} \pi r^3 N \rho \quad (50)$$

where ρ is the density of a water droplet. Thus, we have

$$V = 2.608 r/w \quad (51)$$

Therefore, if the size of the droplets remains constant, the visual range varies inversely as the water content. If however, the number of particles, N remains constant then we have $r \propto w^{1/3}$ and hence

$$V = C' w^{-2/3} \quad (52)$$

Instead of making these approximations we will develop a semi-empirical model of fogs. Consider the fog extinction coefficient

$$\kappa(z, \lambda) = \int_0^{\infty} n(z, r) \sigma(z, r, \lambda) dr \quad (53)$$

but, if $\sigma(z, r, \lambda) = \sigma(r, \lambda)$ then

$$\sigma(r, \lambda) = \pi r^2 Q(r, \lambda) \quad (54)$$

Furthermore, let the size distribution be given by

$$n(z, r) = N(z) \psi(r) \quad (55)$$

where $N(z)$ is the number of particles per unit volume and $\psi(r)$ is the distribution function. Hence,

$$\begin{aligned} \kappa(z, \lambda) &= N(z) \int_0^{\infty} \psi(r) \pi r^2 Q(r, \lambda) dr \\ &= N(z) F(\lambda) \end{aligned} \quad (56)$$

Now, the water content $w(z)$ is

$$\begin{aligned} w(z) &= \int_0^{\infty} n(z, r) \frac{4}{3} \pi r^3 \rho dr \\ &= N(z) C \end{aligned} \quad (57)$$

Therefore, we have the scaling relation

$$\kappa(z, \lambda) = \frac{\kappa(z, \lambda)}{\kappa(z, \lambda^*)} \frac{\kappa(z, \lambda^*)}{\kappa(z_p, \lambda^*)} \kappa(z_p, \lambda^*) \quad (58)$$

$$= \frac{F(\lambda)}{F(\lambda^*)} \frac{w(z)}{w(z_p)} \kappa(z_p, \lambda^*) \quad (59)$$

$$= f(\lambda) g(z) \kappa(z_p, \lambda^*) \quad (60)$$

where z_p is some altitude at which the visual range is measured. Thus, we have a formula to describe the spectral and altitude dependence of the fog extinction coefficient. In Equation (60) $\lambda^* = 0.55$. We finally have the relation

$$\kappa_{ij}(z, \lambda) = \frac{3.912 f_i(\lambda) g_j(z)}{V(z_p)} \quad (61)$$

We shall use for $f_i(\lambda)$ the spectral dependence of each fog type i given in Figure 12. The function $g_j(z)$ which defines the fog profile is very difficult to determine. Very little data exist on the altitude profiles of fogs. Figure 18 illustrates typical profiles for various fogs as taken from Jiusto [29]. An analytic expression which approximates the sea fog profile is the following:

$$g(z) = \frac{z(z_c - z)}{z_p(z_c - z_p)} U(z_c - z) \quad (62)$$

where z_c is the cut-off for the fog and $U(z_c - z)$ is the Heaviside function.

[29] J. E. Jiusto, Project Fog Drops, Investigation of Warm Fog Properties and Fog Modification Concepts, NASA CR-72, 1964.

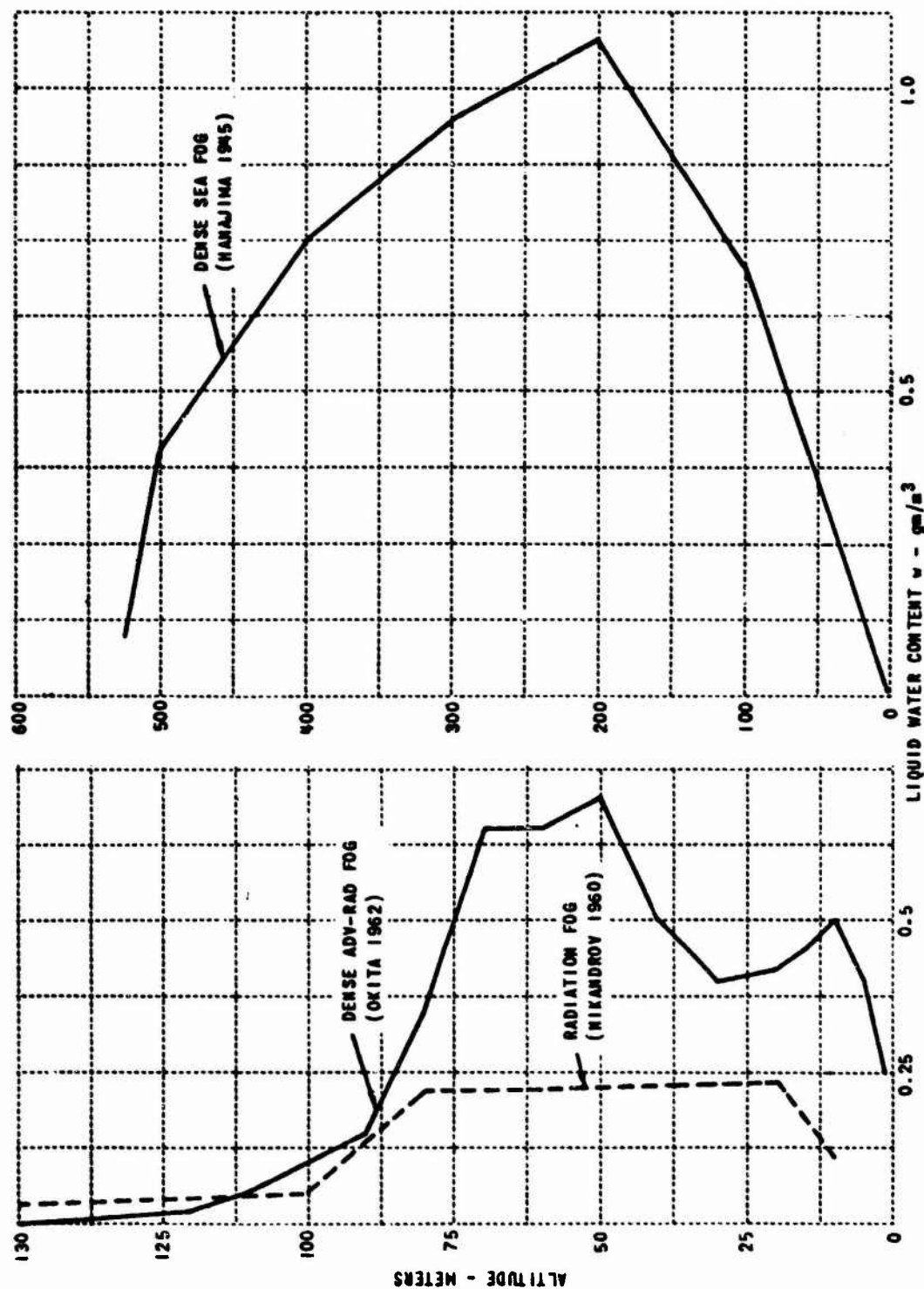


FIGURE 18. VERTICAL DISTRIBUTION OF LIQUID WATER CONTENT IN FOG

NATURAL RADIATION

In this section we shall discuss the natural sources of visible and infrared radiation with emphasis on nighttime conditions.

5.1 SOLAR SPECTRUM

The extraterrestrial value of the solar spectrum at the top of Earth's atmosphere has been measured several times in the last few years. In the past, measurements of the solar spectrum were conducted on the Earth's surface for various air masses and then extrapolations were made to estimate the spectrum at the top of the atmosphere. A typical set of solar values at sea level are given in the Handbook of Geophysics [30]. With the accessibility of high flying instrumented aircraft and spacecraft, good extraterrestrial values of the solar spectrum were obtained by Arvesen et al. [31] and Thekaekara and Drummond [32]. The NASA standard values of Thekaekara and Drummond are those which one shall use in our analysis. It is not known to what extent the solar spectrum changes spectrally over an extended period of time. Solar flares and the eleven year solar cycle do cause changes in the total output but just how the spectrum changes is part of continuing astrophysical research. It is generally believed however, that the variations in the visible and near infrared parts of the solar spectrum are not greater than the geometric variation from perihelion to aphelion. The latter changes by about seven per cent and can easily be calculated.

[30] USAF Air Research and Development Command, Handbook of Geophysics, The Macmillan Co., New York, Rev. Ed., 1961.

[31] J. C. Arvesen, R. N. Griffin, Jr. and B. D. Pearson, Jr., Determination of Extraterrestrial Solar Spectral Irradiance from a Research Aircraft, Appl. Optics, 8, No. 11, 1969.

[32] M. P. Thekaekara and A. J. Drummond, Standard Values for the Solar Constant and Its Spectral Components, Nature Phys. Sci., 229, 1971, pp. 6-9.

5.2 THE LUNAR SPECTRUM

5.2.1 EXTRATERRESTRIAL VALUES

During the daytime the sun overwhelms every other source of natural radiation. It has no intrinsic radiative properties of its own and all radiation which emanates from the moon arises from reflected sunlight, absorbed sunlight being reemitted by a heated lunar surface, or earth-shine being reflected by the moon. Since we are concerned primarily with the visible and near infrared part of the spectrum, we shall only consider the directly reflected sunlight. We shall now see how to calculate the lunar spectrum at the top of Earth's atmosphere given the solar spectrum.

We can define the geometrical albedo of the moon as the ratio of the exitance at a phase angle of zero (full moon) to the total solar irradiance on the moon, i.e.,

$$p(\text{geometrical albedo}) \equiv E(0)/E_0 \quad (63)$$

The Bond albedo is defined as the ratio of the radiation reflected over all angles to the solar input, i.e.,

$$A(\text{Bond albedo}) \equiv \frac{1}{E_0} \int_0^{2\pi} E(\alpha) \sin \alpha \, d\alpha \quad (64)$$

but, this can be written as

$$2 \frac{E(0)}{E_0} \int_0^{\pi} \phi(\alpha) \sin \alpha \, d\alpha = pq \quad (65)$$

where

$$q = 2 \int_0^{\pi} \phi(\alpha) \sin \alpha \, d\alpha \quad (66)$$

is called the phase integral. The so-called phase function of the moon has been the subject of much investigation over the years. Early measurements of the relative intensity of moonlight as a function of lunar phase were made by Russell [33], Rougier [34], and Bullrich [35]. Figure 19 illustrates the variation in a lunation according to Russell. Lane and Irvine [36] determined values of the phase function on terms of wavelength.

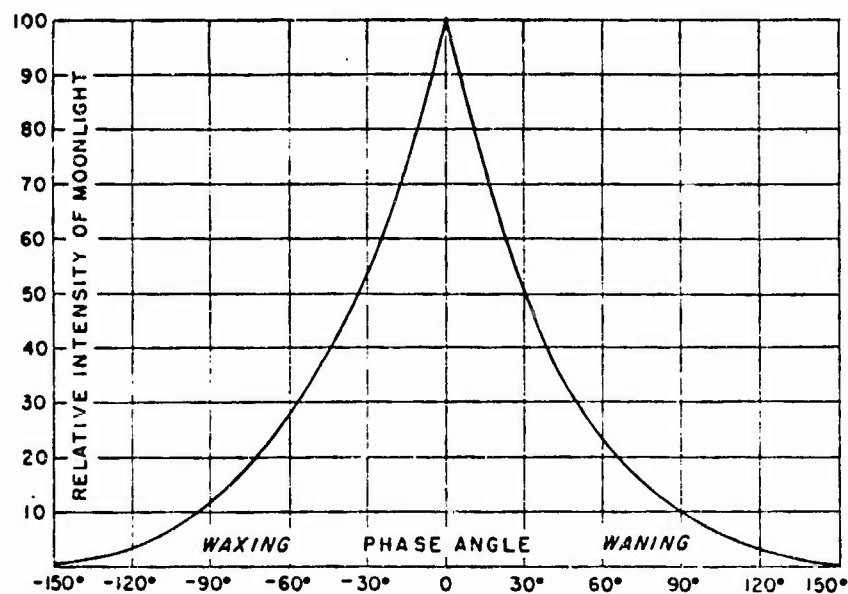


FIGURE 19. VARIATION IN A LUNATION

[33] H. N. Russell, *Ap. J.* 43, 1916, p. 117.

[34] M. G. Rougier, *Ann. Obs. Strassbourg*, 2, 1933, p. 205.

[35] K. Bullrich, *Ber. Deutsch. Wetterd.*, U.S. Zone No. 4, 1948.

[36] A. P. Lane and W. M. Irvine, *Astron. J.* 78, No. 3, 1973, p. 267.

For our studies however, this degree of refinement is not necessary and we shall use Bullrich's values for all wavelengths. These are presented in Table 1.

TABLE 1. THE INTEGRATED PHASE-CURVE OF THE MOON

Phase Angle	<u>Relative Intensity</u>		Phase Angle	<u>Relative Intensity</u>	
	Rougier	Bullrich		Rougier	Bullrich
0°	100	100	90°	8.0	6.7
10	72.5	73.2	100	5.6	4.7
20	57.8	56.0	110	3.9	3.6
30	43.7	42.3	120	2.5	2.4
40	33.9	32.0	130	1.6	1.2
50	26.3	23.3	140	0.9	0.9
60	20.8	16.7	150	0.4	0.4
70	16.6	12.4	160	0.002	0.002
80	11.5	8.7			

Values of the geometric albedo, p of the moon were taken from data of Condrón et al. [37] and of Lane and Irvine [36]. The geometric albedo [37] is shown in Figure 20.

In order to determine the extraterrestrial value of the lunar spectrum at the top of Earth's atmosphere we must know the mean angle of the moon subtended at Earth. The mean half angle $\bar{\theta}_m$ is

$$\bar{\theta}_m = 932.7'' \quad (67)$$

[37] T. P. Condrón, J. J. Lovett, W. H. Barnes, L. Marcotte, and R. Nadile, Gemini 7 Lunar Measurements, AFCRL-68-0438, Sept., 1968.

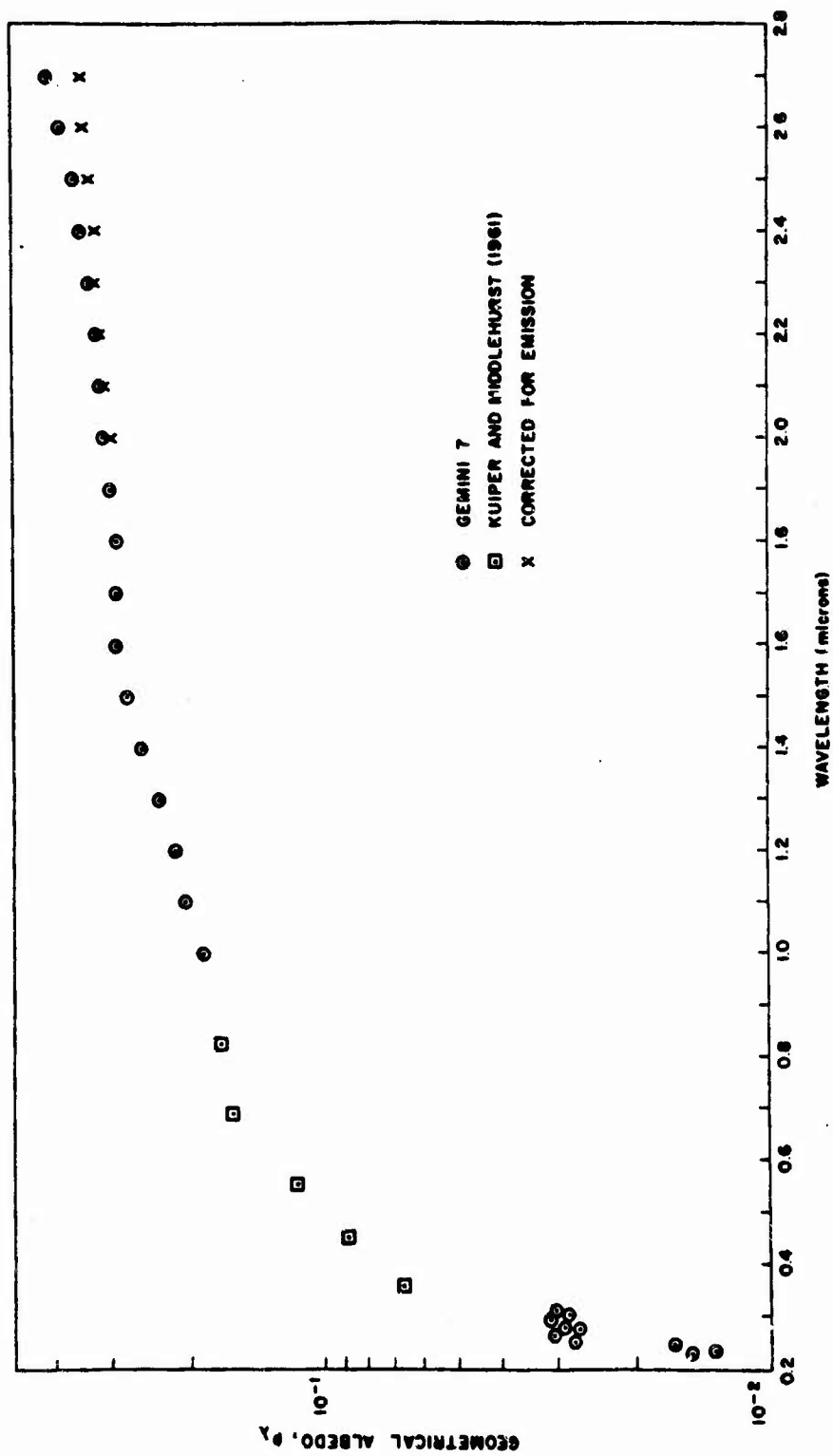


FIGURE 20. GEOMETRICAL ALBEDO VS. WAVELENGTH

Thus, the geometric albedo, p is given by

$$p = \frac{\pi}{\Omega} \frac{E_{om}}{E_o} \quad (68)$$

where Ω is the lunar solid angle and E_{om} is the extraterrestrial lunar irradiance at the top of Earth's atmosphere. Hence, we have, in general

$$E_{om}(\lambda, \chi) = \frac{\Omega}{\pi} E_o(\lambda, \chi) p(\lambda) P(\chi) \quad (69)$$

where $\Omega/\pi = 2.04472 \times 10^{-5}$. The solar irradiance, $E_o(\lambda, \chi)$ depends only slightly on phase angle, χ and we shall neglect this small variation in our present work. The phase function, $P(\chi)$ depends little on the wavelength λ so that we can rewrite Equation (69) as

$$E_{om}(\lambda, \chi) = 2.04472 \times 10^{-5} E_o(\lambda) p(\lambda) P(\chi) \quad (70)$$

where $P(0) = 1$. Using Equation (70) we calculated the lunar spectrum at the top of the atmosphere for a full moon. This is illustrated in Figure 21 along with the solar spectrum.

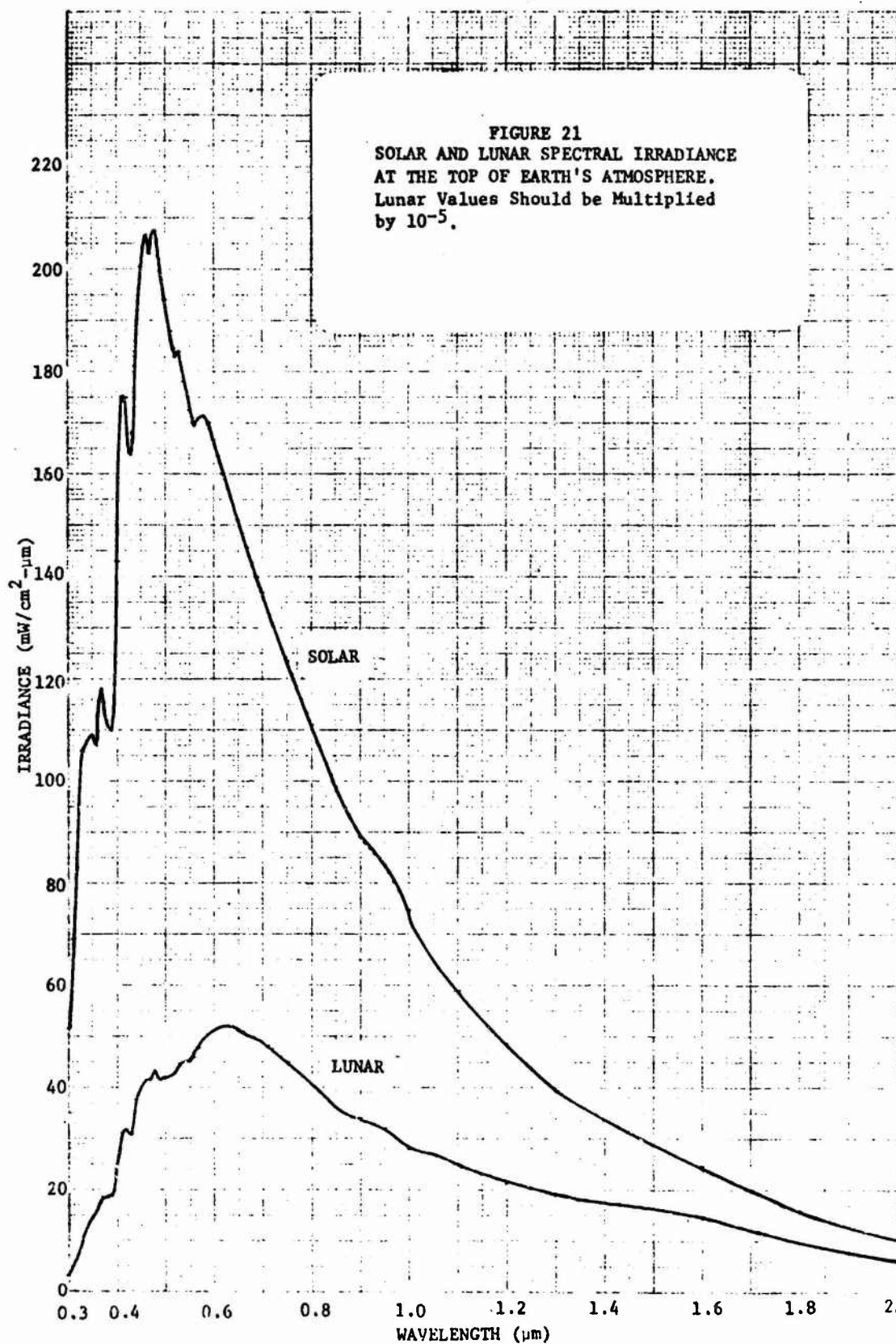
5.2.2 SEA LEVEL VALUES (MEASURED)

The sea level value of the irradiance due to the moon has been measured by a number of investigators over the years. In the period 1943-1947, Brown [38] made photometric measurements of daytime and nighttime illumination as a function of solar altitude throughout the world. Figure 22 gives the illuminance as a function of solar and lunar altitude. Pleiter and Morley [39] and Vatsia et al. [40] measured spectral irradiance

[38] D. R. E. Brown, Natural Illumination Charts, Report No. 374-1, Dept. of the Navy, Bureau of Ships, Washington, D.C., 1952.

[39] D. Pleiter and G. A. Morley, Night Radiation Measurements, Defense Documentation Center, AD 865252.

[40] M. L. Vatsia, U. K. Stich, and D. Dunlap, J. Opt. Soc. Am. 59, 483 (1969).



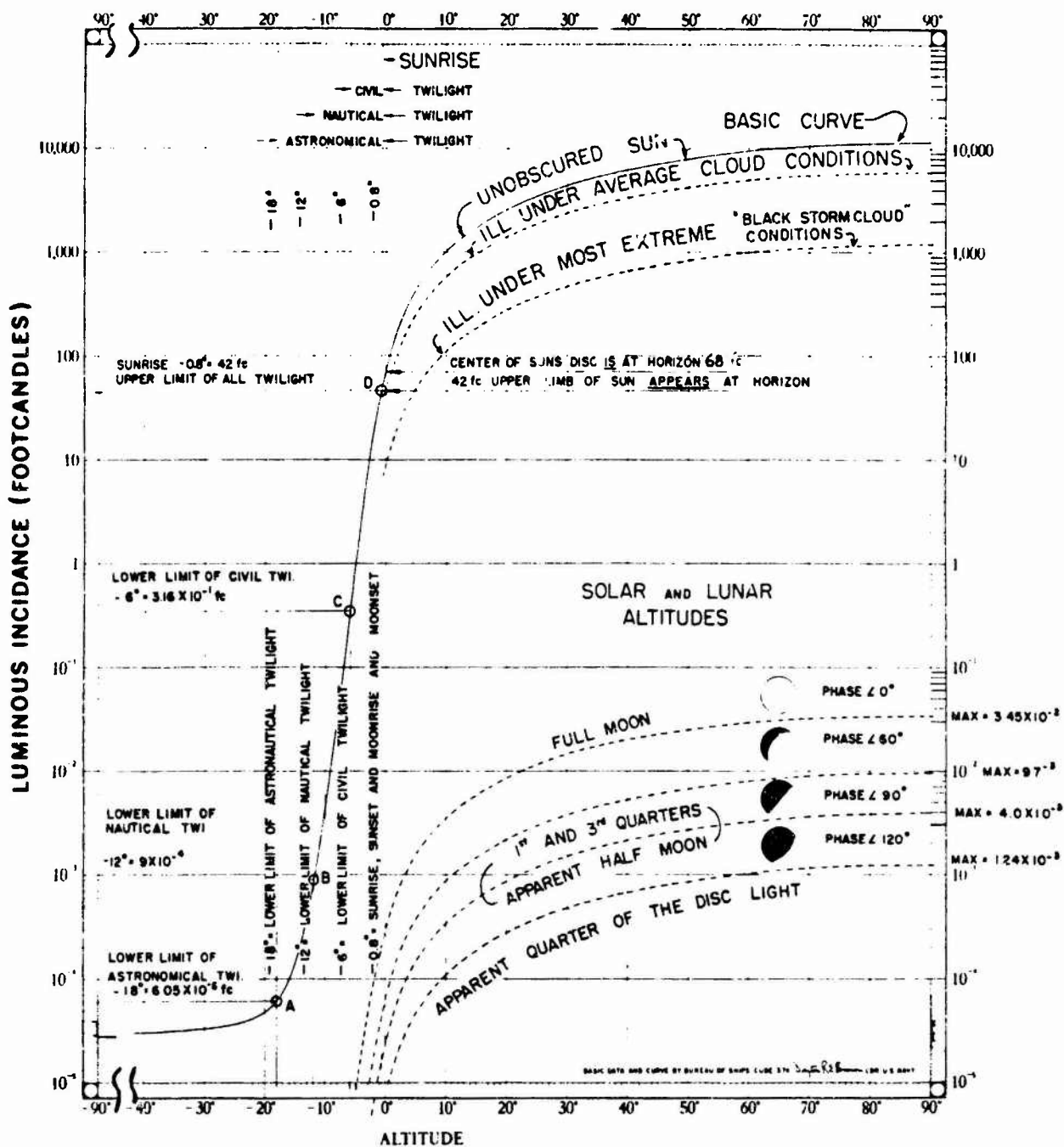


FIGURE 22. NATURAL LUMINOUS INCIDENCE (ILLUMINANCE) AS A FUNCTION OF SOLAR AND LUNAR ALTITUDE AND FOR VARIOUS PHASES OF THE MOON AS MEASURED BY BROWN

and spectral radiance at Lake Montauban, Canada for various lunar altitudes and per cent cloud cover. Biberman [41] presents irradiance values for moonlight plus airglow for various lunar phases and air masses. The measured values for Vatsia et al. [40] are shown in Figure 23. Biberman's results are illustrated in Figures 24, 25, 26, and 27.

5.2.3 SEA LEVEL VALUES (CALCULATED)

Although it is desirable to have measurements of the radiance and irradiance of the moon, there is a practical limit to the number of measurements which can be made in order to account for all possible atmospheric conditions. For this reason it is necessary to have an atmospheric-radiative-transfer model which will allow one to calculate the radiation field in a realistic atmosphere for a wide range of environmental conditions. Such a model was developed by Turner [42] for use in NASA's processing of multispectral data obtained by Earth satellites. The model allows one to calculate the spectral irradiance on the Earth's surface due to the sun or moon in terms of solar or lunar zenith angle, lunar phase, surface reflectance, and horizontal visual range.

The direct radiation from the moon is attenuated exponentially by the atmosphere. That part of the radiation which is not absorbed is scattered one or more times and produces what is called the diffuse component. Figure 28 illustrates the variation of the diffuse lunar irradiance at the Earth's surface in terms of the lunar zenith angle for a full moon. The atmospheric states considered range from a very hazy atmosphere of visibility 2 km to the clearest possible atmosphere with a visibility of 336 km. Values of the irradiance for angles greater than 75° are not to be considered as being extremely reliable since refraction of

[41] L. M. Biberman, Natural Levels of Illumination and Irradiance, Photoelectronic Imaging Devices, Vol. 1, Chapt. 3, Plenum Press, N.Y., 1971.

[42] R. E. Turner, Radiative-Transfer in Real Atmospheres, ERIM 190100-24-T, Environmental Research Institute of Michigan, 1974.

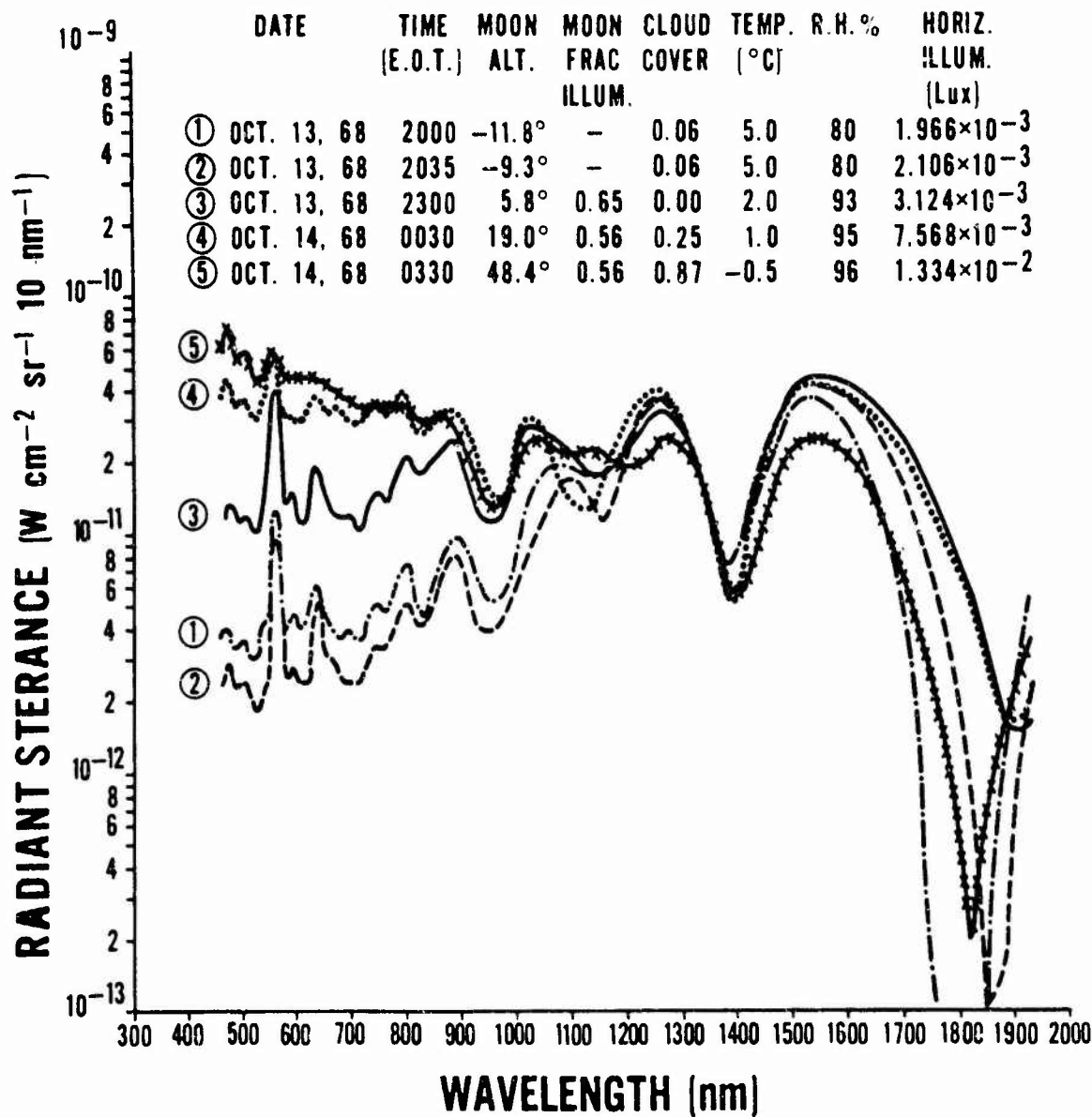


FIGURE 23. NIGHT SKY RADIANT STERANCE SPECTRA FOR VARIOUS ALTITUDES OF THE MOON AS MEASURED BY VATSIA, STICH AND DUNLAP

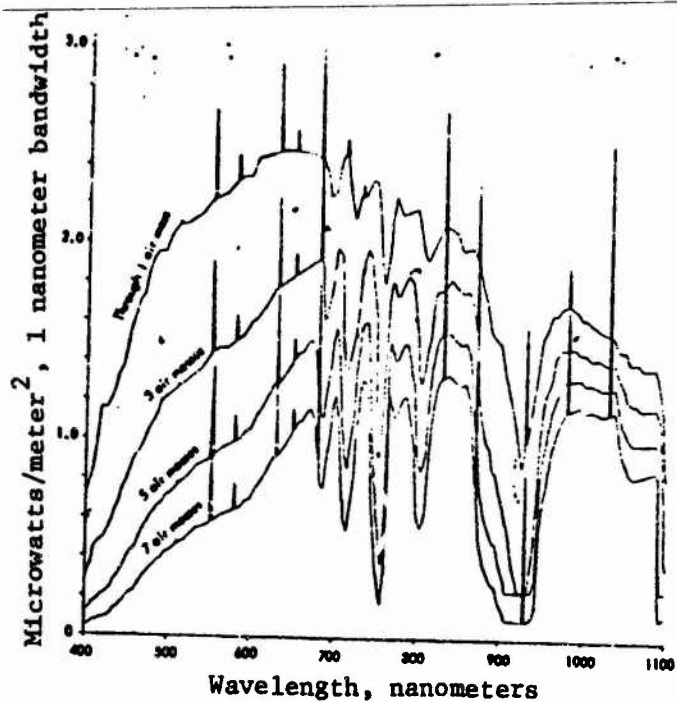


FIGURE 24. IRRADIANCE FROM FULL MOONLIGHT PLUS AIRGLOW

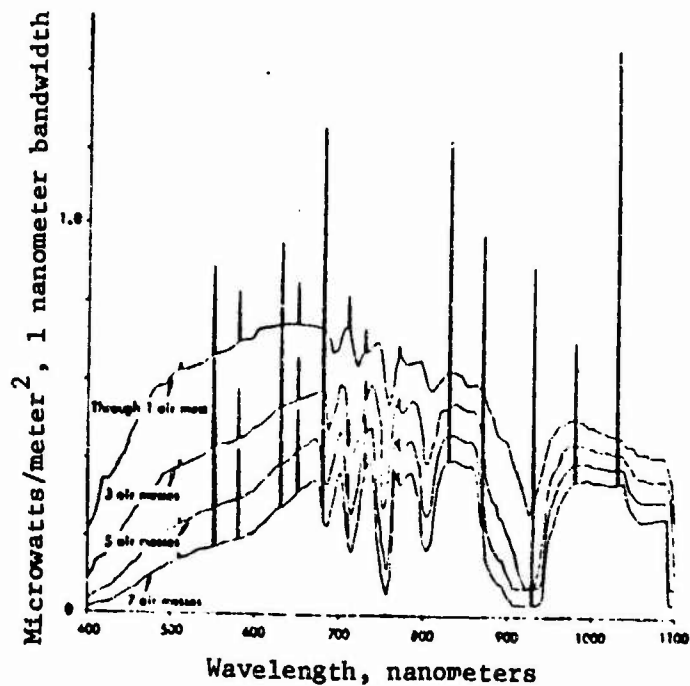


FIGURE 25. IRRADIANCE FROM 0.3 x FULL MOONLIGHT PLUS AIRGLOW

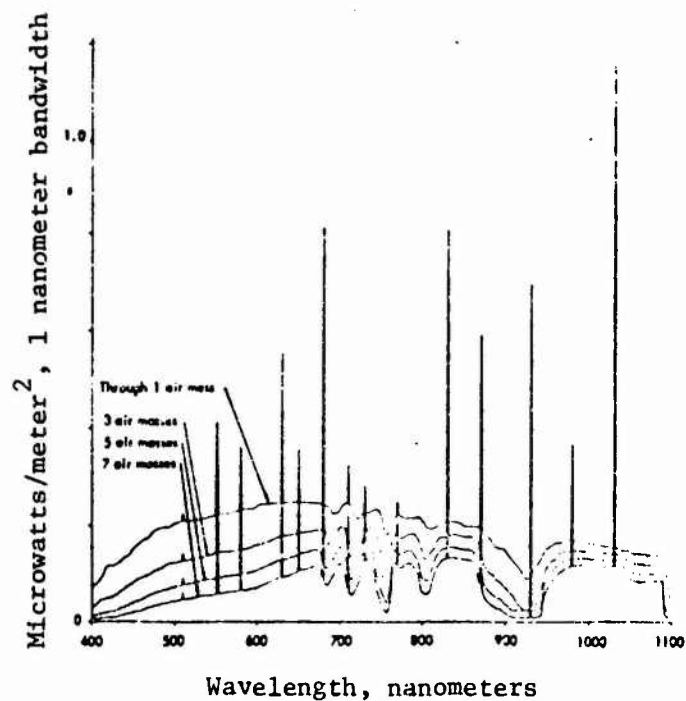


FIGURE 26. IRRADIANCE FROM 0.1 x FULL MOONLIGHT PLUS AIRGLOW

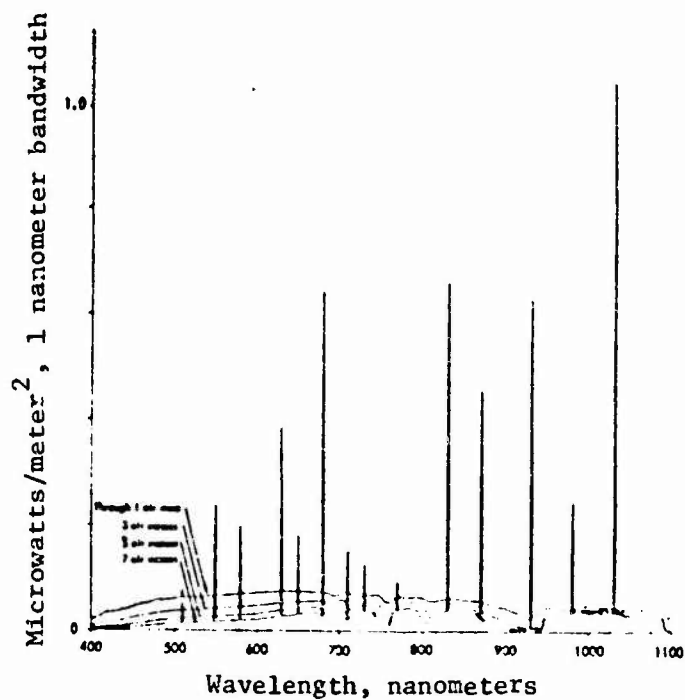
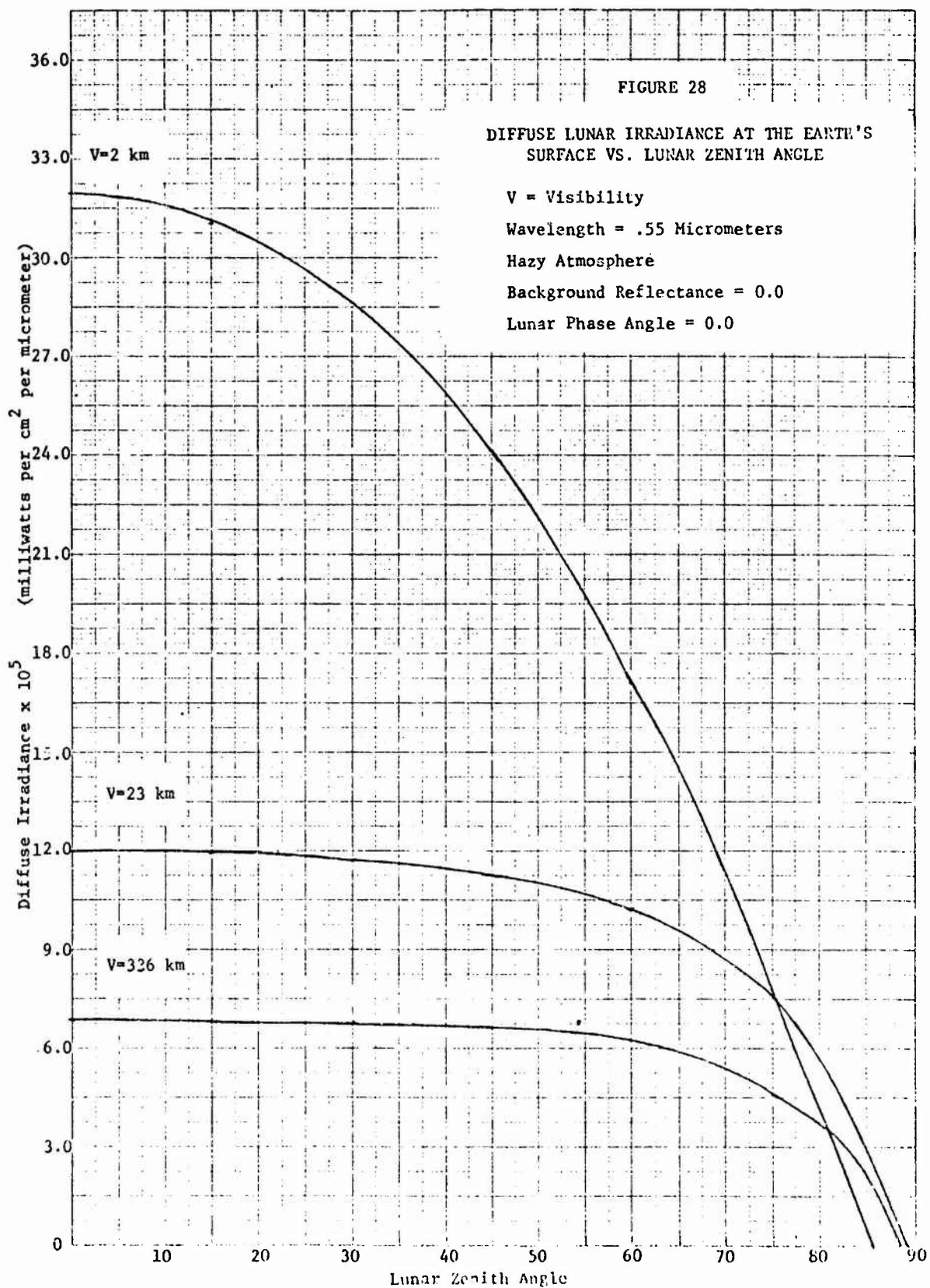


FIGURE 27. IRRADIANCE FROM 0.03 x FULL MOONLIGHT PLUS AIRGLOW

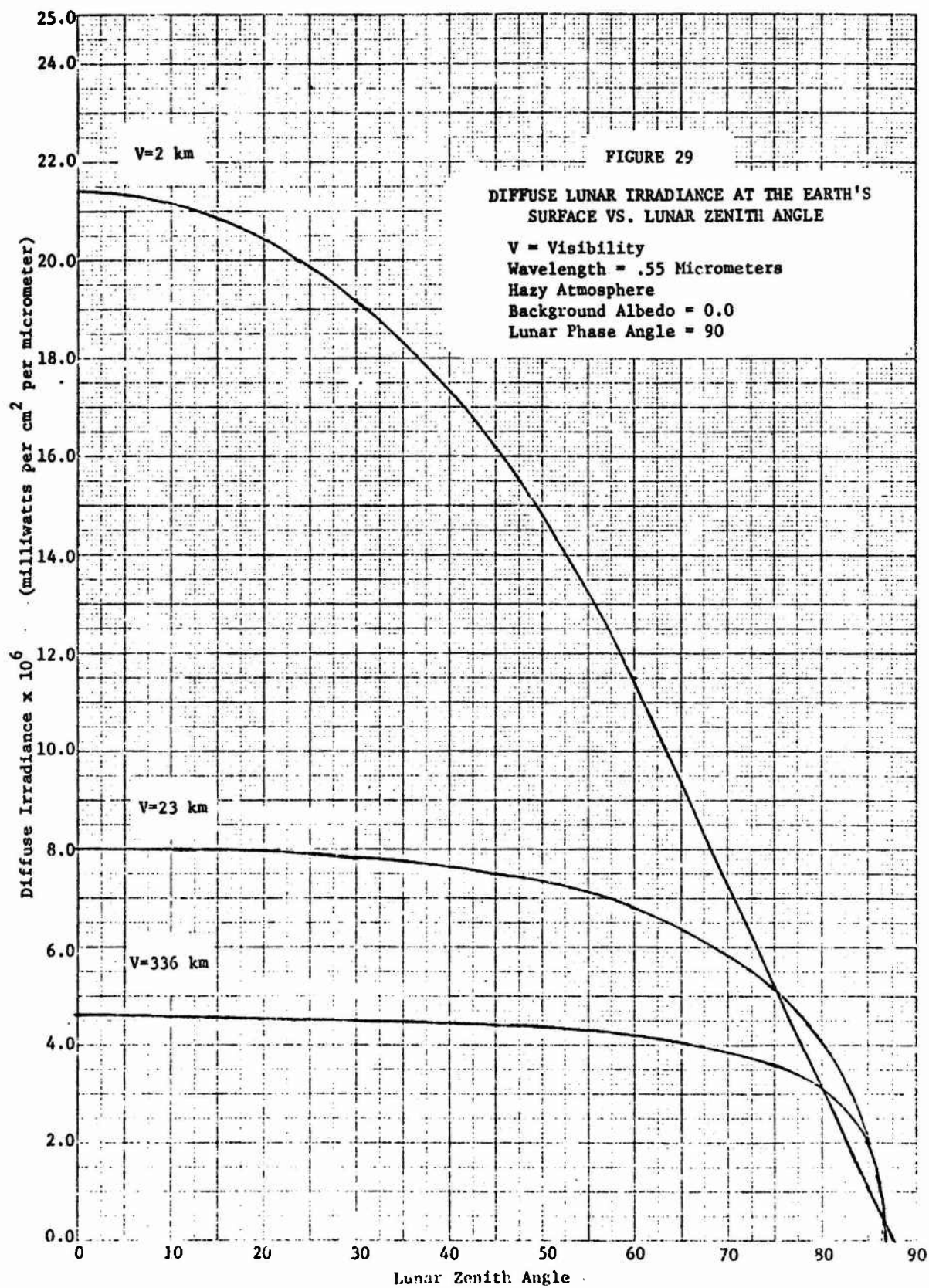


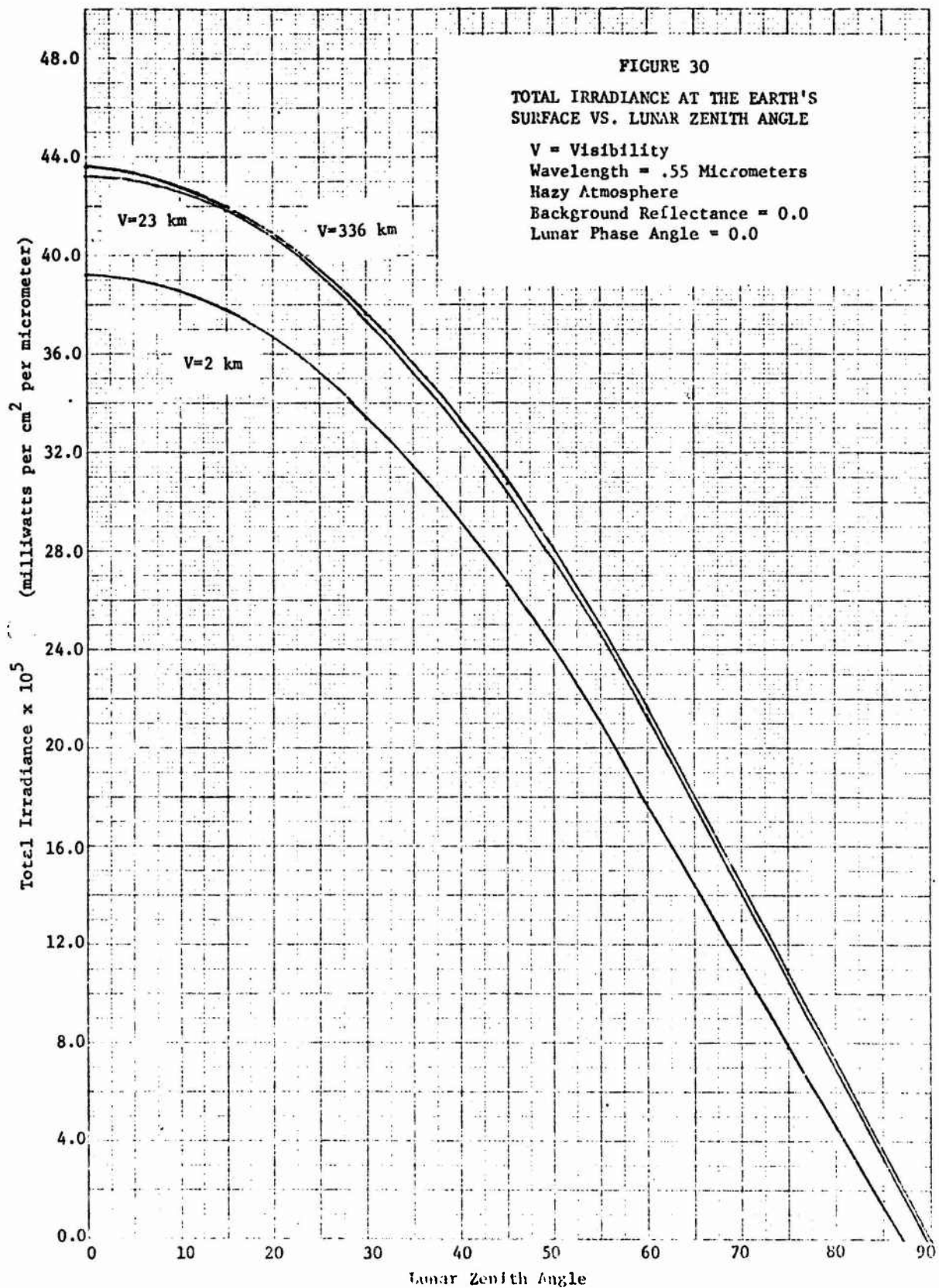
the atmosphere was not used in the model. Figure 29 illustrates the same variation except for a quarter moon.

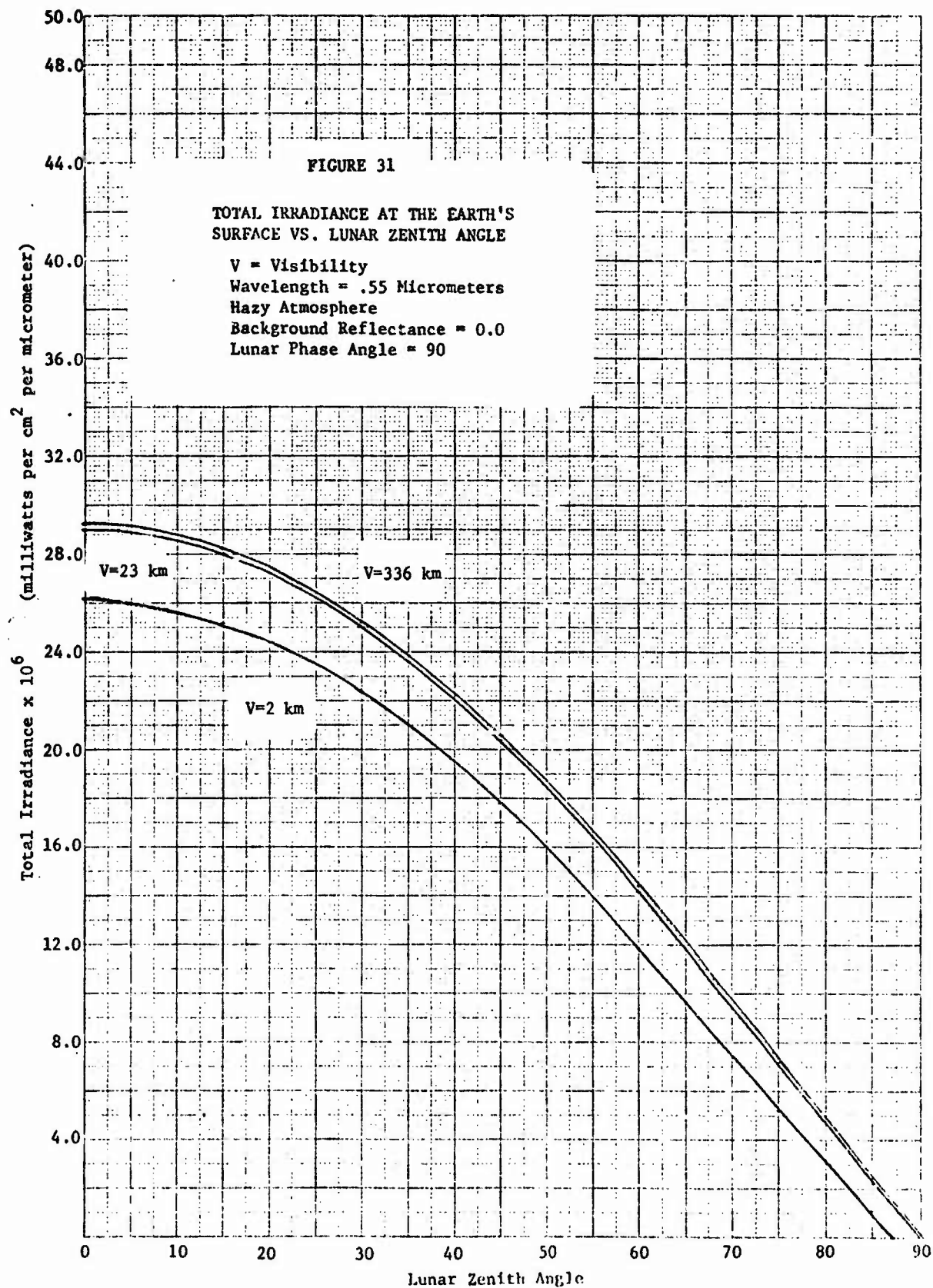
The total lunar irradiance is the sum of the diffuse component and the directly attenuated radiation. Figures 30 and 31 illustrate the variation of total lunar irradiance with lunar zenith angle for the full moon and the quarter moon. As can be seen, the dependence on visibility is small. This is a result of the sum of the direct and diffuse components. The diffuse radiation is greater for hazy atmospheres and the direct component is less than for clear atmospheres. Hence, the sum of the two opposing effects (attenuation and scattering) combine in such a way as to minimize the variation with visibility. This effect is depicted in Figures 32 and 33 for the full and quarter moons.

Transmittance is sometimes a more meaningful quantity than visibility. Let us consider the variation of the diffuse and total irradiance with transmittance at a wavelength corresponding to the peak value of the visual response of the human eye. Figure 34 illustrates this variation. For extremely thick atmospheres, as in fogs, the total and diffuse components have the same value for a given surface. When the transmittance reaches a value of about one per cent however, the diffuse irradiance decreases sharply with a further increase in transmittance. At a transmittance of one all the total irradiance curves have the same value, which are independent of reflectance as they should be since the total irradiance becomes equal to the direct irradiance at the top of the atmosphere. It is interesting that the total irradiance and the diffuse irradiance can be greater than the input value at the top of the atmosphere. This arises because for highly reflecting surfaces the diffuse radiation reflects back and forth between the surface and the overlying turbid atmosphere and the radiation is effectively trapped.

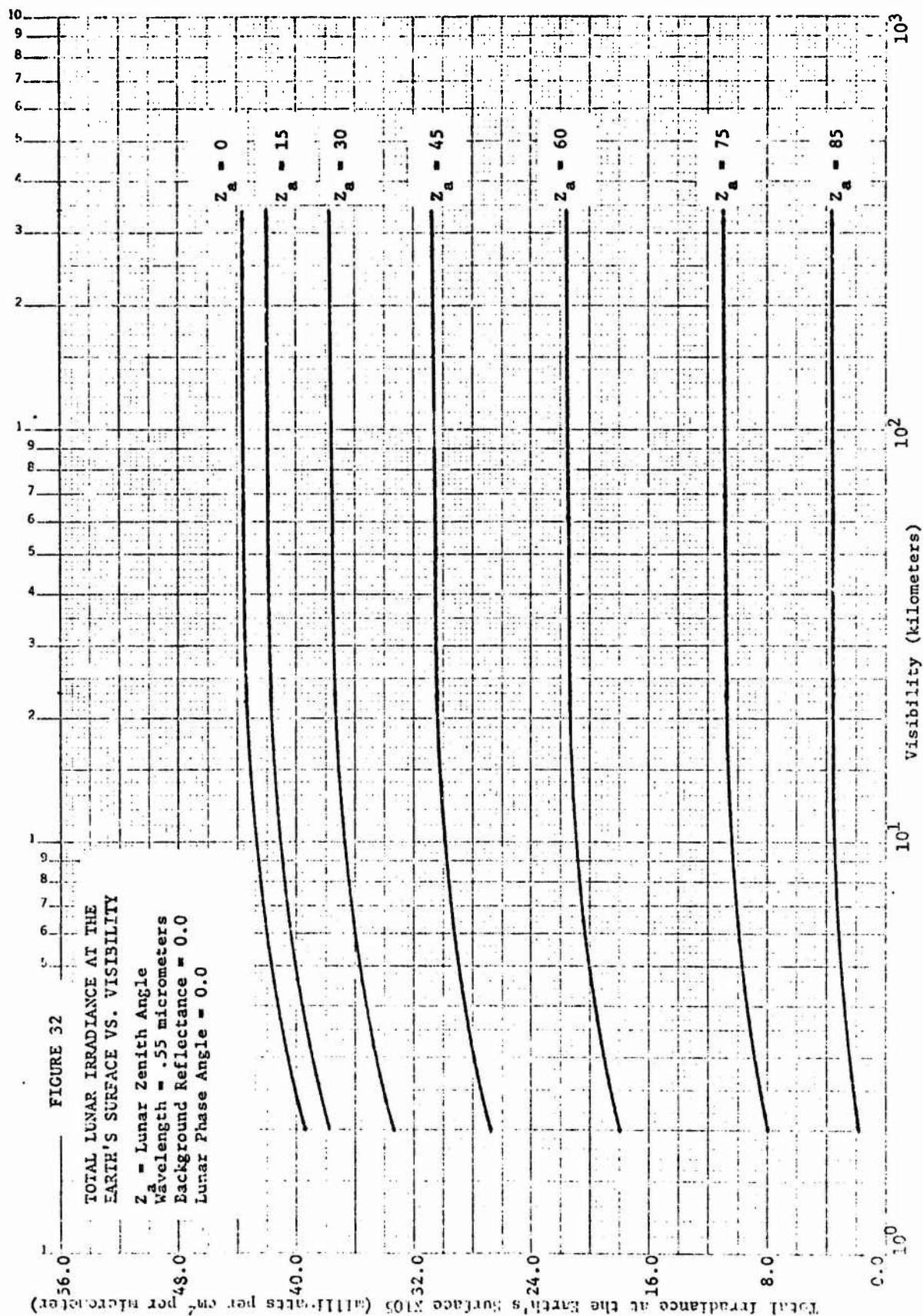
The dependence on reflectance can be understood more easily by looking at Figure 35. For atmospheres which are not extremely thick there is almost a linear relationship connecting the diffuse irradiance with reflectance but for optically thick atmospheres the relationship is

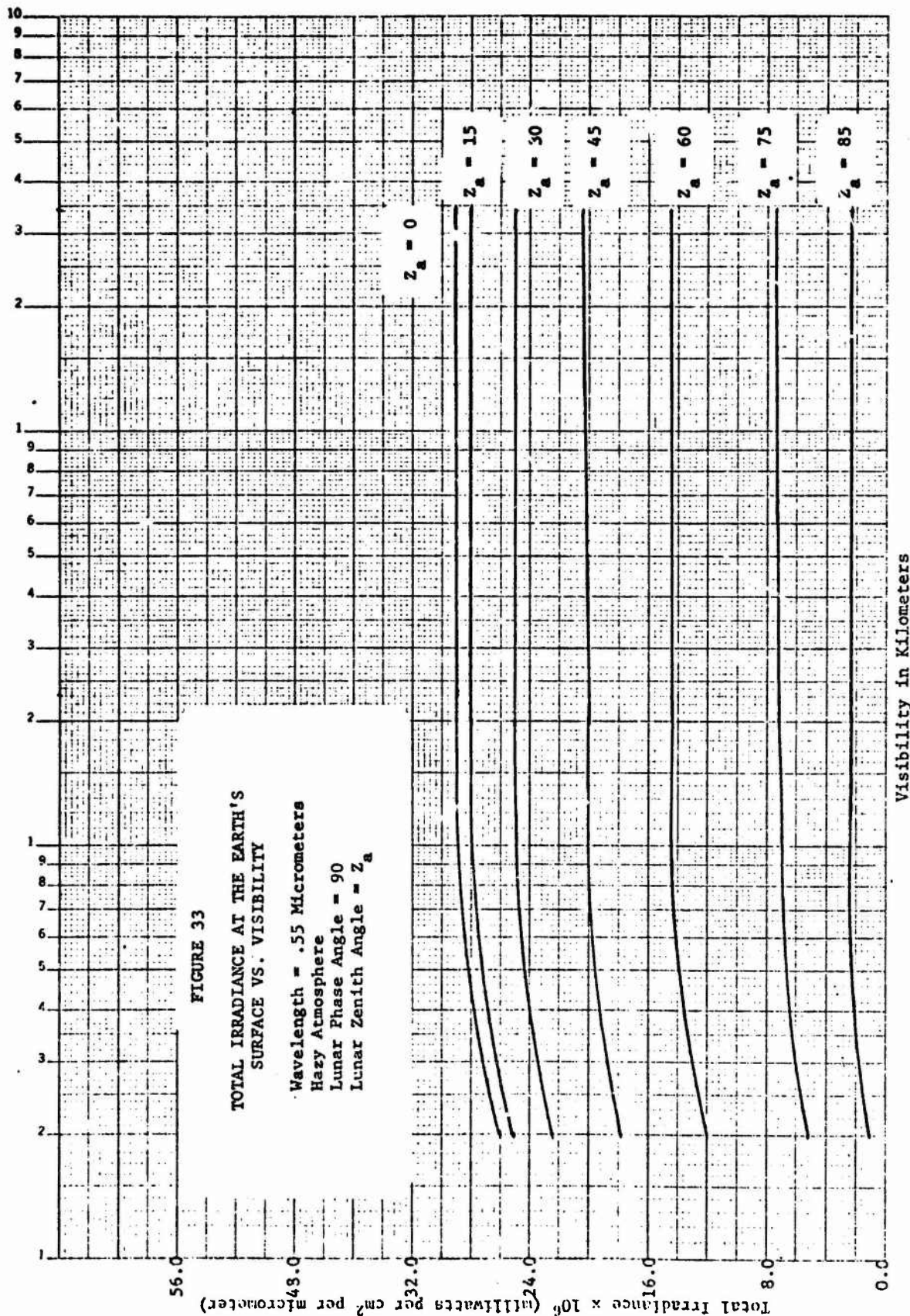


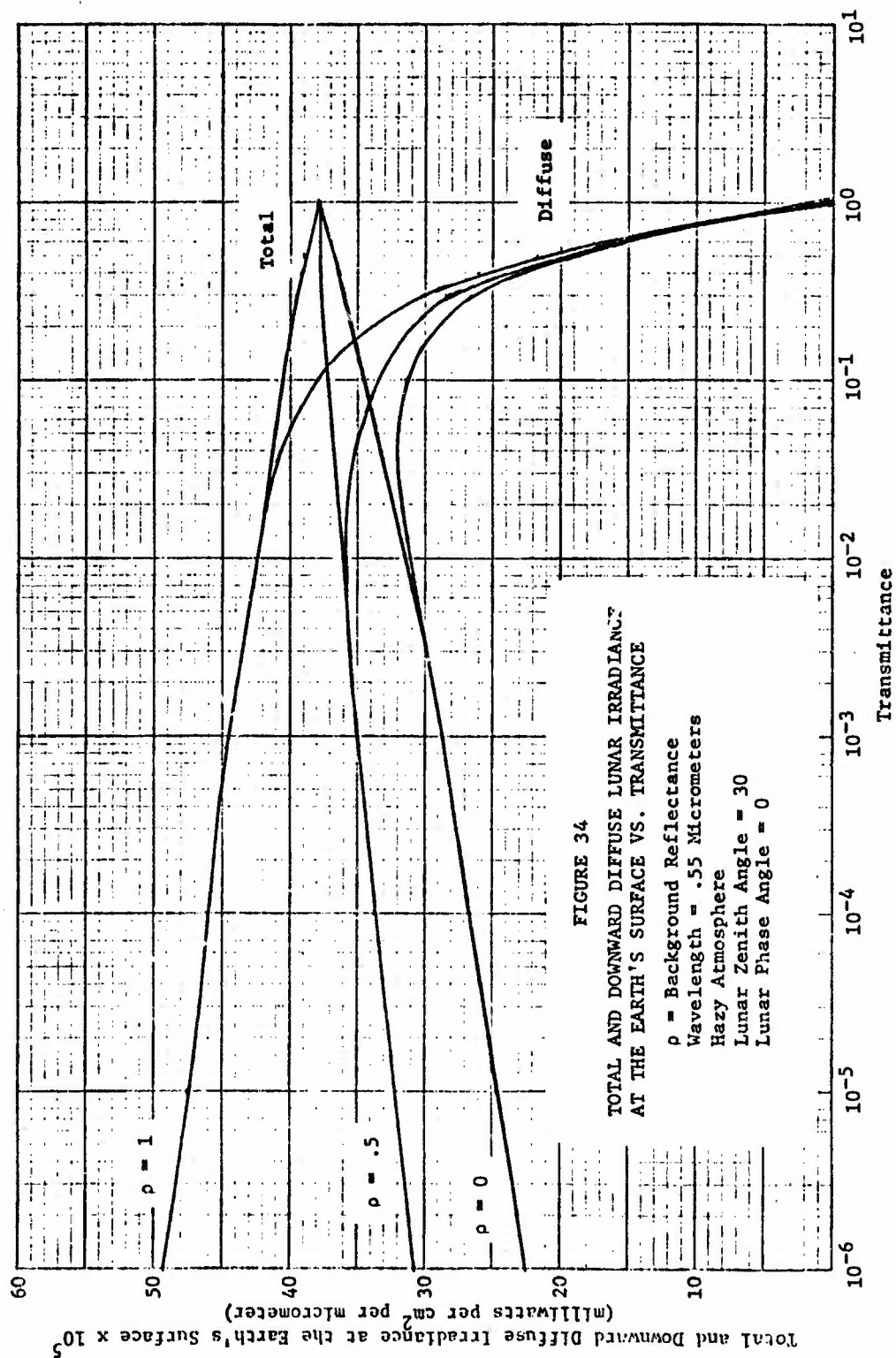


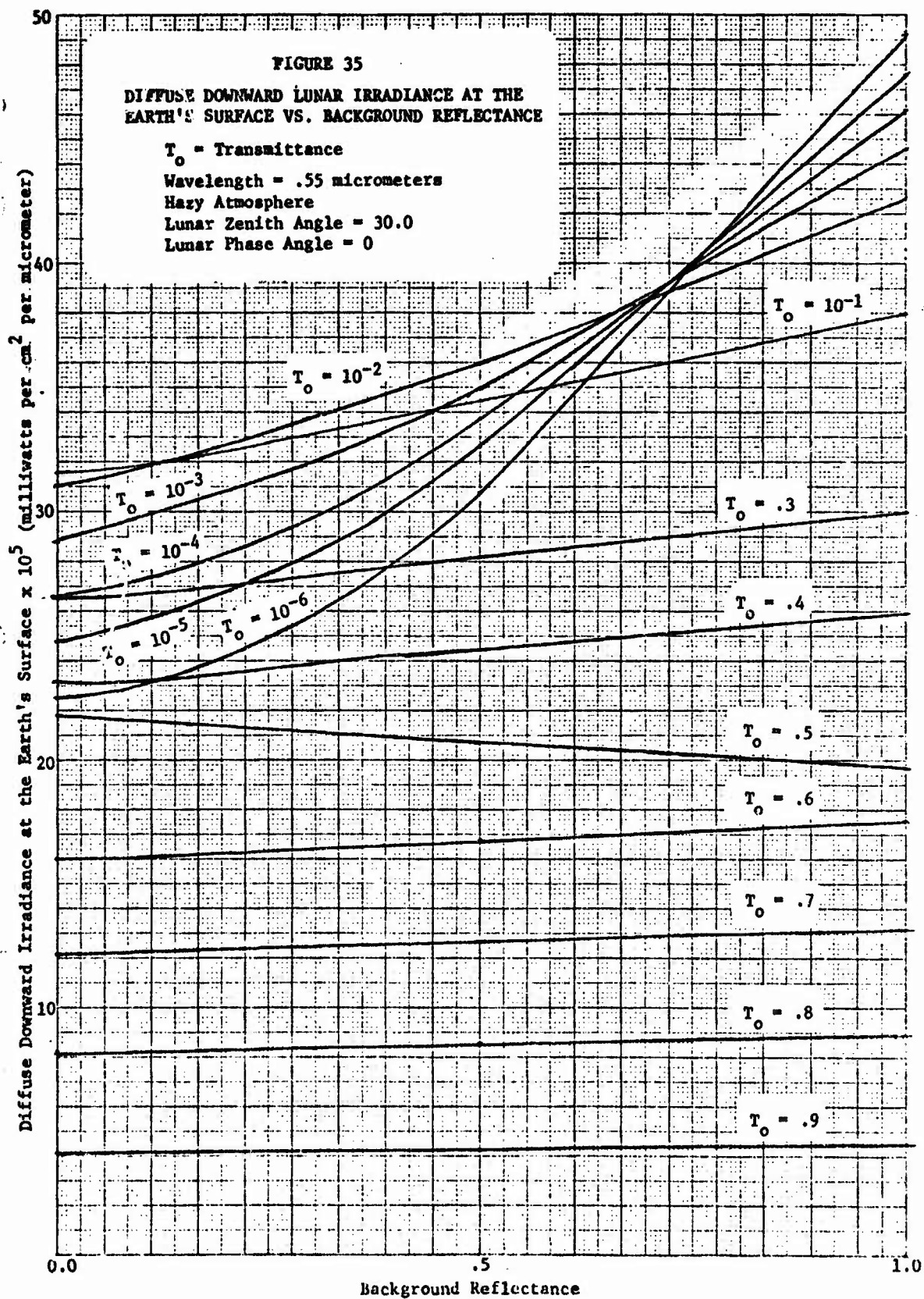


VISIBILITY IN KILOMETERS







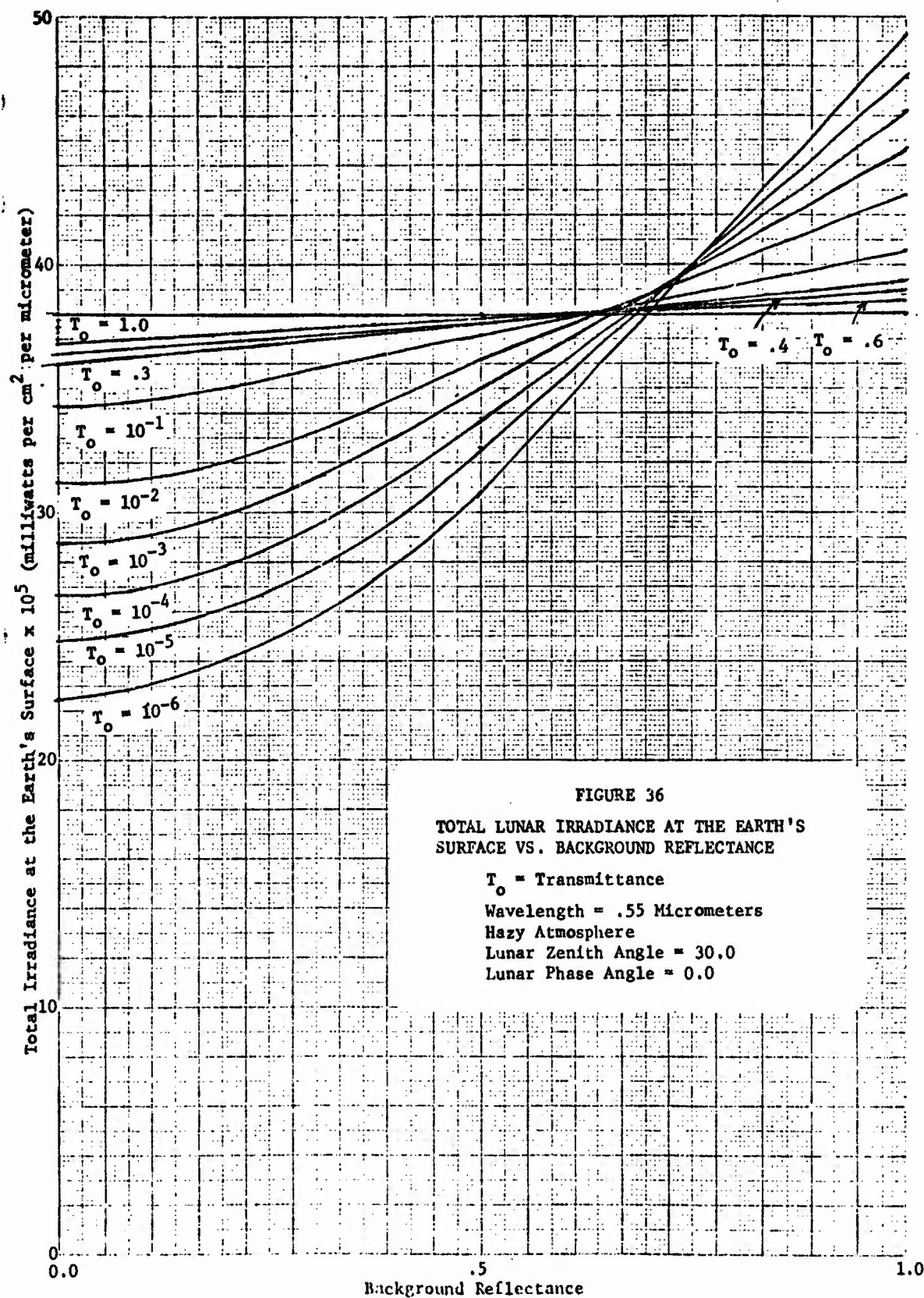


non-linear. It is interesting to note that at least in this particular case the diffuse irradiance is independent of transmittance for a reflectance near 0.70.

Finally, we can investigate the dependence of total irradiance on reflectance by analyzing Figure 36. Here we see that for ordinary atmospheric states with reasonable transmittances the total irradiance is essentially independent of reflectance. For foggy atmospheres, however, there is a distinct non-linear relationship. For low values of reflectance and as the atmosphere becomes clear more radiation is able to reach the surface and therefore the total irradiance increases. On the other hand, for high reflectance values, and as the atmosphere becomes clear, more radiation is able to leave the atmosphere by reflection and hence the total irradiance decreases. As in the case of diffuse irradiance there exists a small region of reflectance values such that the irradiance is essentially independent of transmittance.

In this section we have seen how the lunar irradiance varies with the normal environmental parameters. The spectral dependence of irradiance is that of the extraterrestrial lunar value modified by the basic spectral dependence of whatever atmosphere and surface reflectance exists. To consider all of these functional relationships is beyond the immediate scope of this study. These investigations are included in a report by Malila et al. [43].

[43] W. A. Malila, R. B. Crane, and R. E. Turner, Information Extraction Techniques for Multispectral Scanner Data, Report No. 31650-74-T, Willow Run Laboratories, Ann Arbor, 1972.



ARTIFICIAL SOURCES

In this section we shall consider the radiation field in an atmosphere composed of isotropic point sources (flares). The general mathematical problem of determining the complete multiply scattered field is quite complicated. Instead, we shall concentrate on the most important terms, the directly attenuated irradiance on the horizontal surface and singly-scattered irradiance.

6.1 POINT SOURCE

The general three-dimensional radiative-transfer equation for a point source is

$$\hat{\Omega} \cdot \nabla L(\vec{r}, \hat{\Omega}) + \kappa(\vec{r}) L(\vec{r}, \hat{\Omega}) - \frac{\beta(\vec{r})}{4\pi} \int_{\hat{\Omega}'} p(\hat{\Omega} \cdot \hat{\Omega}') L(\vec{r}, \hat{\Omega}') d\hat{\Omega}' = \frac{S}{4\pi} \delta(\vec{r} - \vec{r}_0) \quad (71)$$

where $\hat{\Omega}'$ is the direction of the incoming ray and $\hat{\Omega}$ is the direction of the received ray. S is the spectral power output of the source in watts and $L(\vec{r}, \hat{\Omega})$ is the spectral radiance at point \vec{r} . The spectral irradiance on the surface is given by

$$E(\vec{R}) = \int_{\hat{\Omega}'} \hat{n} \cdot \hat{\Omega}' L(\vec{R}, \hat{\Omega}') d\hat{\Omega}' \quad (72)$$

where \vec{R} is a vector from the origin of coordinates to the point in question located on the surface. The vector \hat{n} is the surface normal vector.

Actually, Equation (71) is used to find the Green's function for the radiative-transfer equation. This function is then the solution of the basic equation for a point source.

6.2 DISTRIBUTED SOURCE

The solution for a spatially distributed source is given by

$$L(\vec{r}, \hat{\Omega}) = \int \int \rho(\vec{r}_0, \hat{\Omega}_0) G(\vec{r}, \hat{\Omega}, \vec{r}_0, \hat{\Omega}_0) d\vec{r}_0 d\Omega_0 \quad (73)$$

where $\rho(\vec{r}_0, \hat{\Omega}_0)$ is the spatial distribution of the source and $G(\vec{r}, \hat{\Omega}, \vec{r}_0, \hat{\Omega}_0)$ is the Green's function. Thus, we can integrate over the source coordinates and obtain the radiance, $L(\vec{r}, \hat{\Omega})$ at any point \vec{r} . Examples of distributed sources are: clouds, buildings, mountains, burning vehicles, and other fires.

6.3 THE RADIATION FIELD

We shall now consider the radiation field from a point source. The geometry is illustrated in Figure 37. The radiative-transfer equation is

$$\hat{\Omega} \cdot \nabla L + \kappa(z) L(x, y, z, \mu, \phi) - \frac{\beta(z)}{4\pi} \int_0^{2\pi} \int_{-1}^1 p(\mu, \phi, \mu', \phi') L(x, y, z, \mu', \phi') d\mu' d\phi' = \frac{S}{4\pi} \delta(x) \delta(y) \delta(z - z_0) \quad (74)$$

We separate the radiation fields into two parts, the directly attenuated and the singly-scattered terms, i.e.,

$$L(x, y, z, \mu, \phi) = L_d(x, y, z, \mu, \phi) + L_s(x, y, z, \mu, \phi) \quad (75)$$

Taking the Fourier transform of Equation (74) and performing various mathematical operations we get for the direct radiance

$$L_d(x, y, z, \mu, \phi) = \frac{S}{4\pi\mu} e^{-[\tau(z_0) - \tau(z)]/\mu} \times \delta\left[x - \frac{\xi}{\mu} (z - z_0)\right] \delta\left[y - \frac{v}{\mu} (z - z_0)\right] U(z - z_0) \quad (76)$$

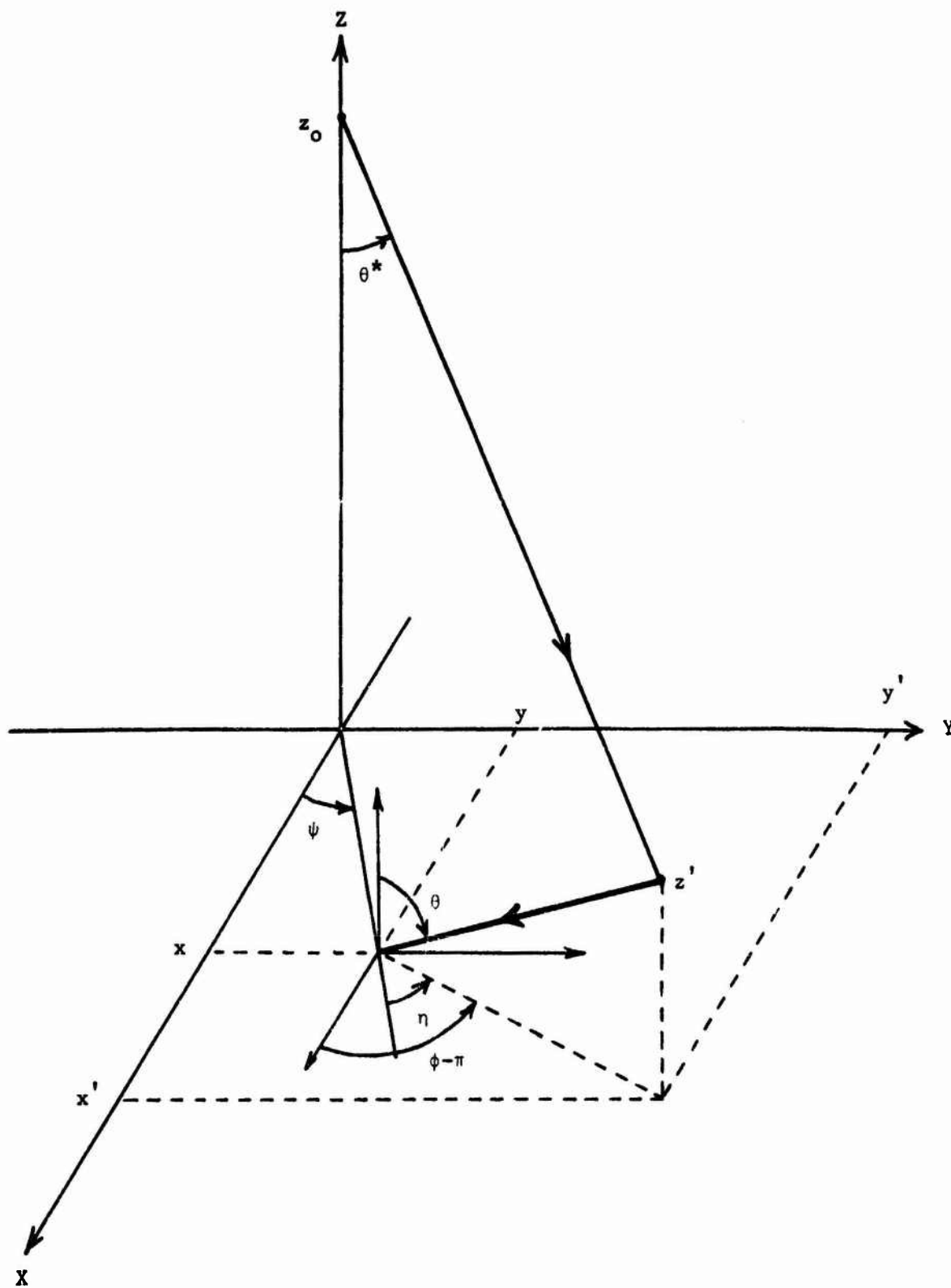


FIGURE 37. POINT SOURCE GEOMETRY .

for the upward directed radiance and

$$L_d(x, y, z, -\mu, \phi) = \frac{S}{4\pi\mu} e^{-[\tau(z) - \tau(z_0)]/\mu} \times$$

$$\delta\left[x - \frac{\xi}{\mu} (z_0 - z)\right] \delta\left[y - \frac{\nu}{\mu} (z_0 - z)\right] U(z_0 - z) \quad (77)$$

for the downward radiance where $\tau(z)$ is the optical depth at altitude z and ξ and ν are direction cosines with respect to the x and y axes. Integrating the downward radiance over a hemisphere gives us the downward attenuated irradiance due to a point source.

$$E_d(R) = \frac{z_0 S e^{-[\tau_0 - \tau(z_0)]} \sqrt{R^2 + z_0^2} / z_0}{4\pi(R^2 + z_0^2)^{3/2}} \quad (78)$$

where R is the distance from the origin along the surface.

Now, integrating the radiative-transfer equation once and performing considerable mathematical analysis leads to the following solution for the radiance

$$L_g(R, \eta, 0, -\mu) =$$

$$\frac{S}{16\pi^2\mu} \int_0^\infty \frac{p(\cos \chi) e^{-[\tau_0 - \tau(z')]/\mu} - \left[\frac{\tau(z_0) - \tau(z')}{z' - z_0} \right] \Delta}{\Delta^2} \beta(z') dz' \quad (79)$$

where

$$\Delta = \sqrt{R^2 + z_0^2 - 2z_0 z' + \frac{z'^2}{\mu^2} + 2Rz' \frac{\sqrt{1-\mu^2}}{\mu} \cos \eta} \quad (80)$$

and

$$\cos \chi = \frac{\mu^2 z_o - z' - R\mu \sqrt{1-\mu^2} \cos \eta}{\mu \Delta} \quad (81)$$

The spectral irradiance due to single scattering from a point source is then given by

$$E_s(R) = \int_0^{2\pi} \int_0^1 \mu L_s(R, \eta, 0, -\mu) d\mu d\eta \quad (82)$$

6.4 RESULTS OF CALCULATIONS

We are now going to see the effect of one or more flares on the illumination of the ground. Also, we shall illustrate the illumination due to the moon.

A typical scene is depicted in Figure 38. We have moonlight and

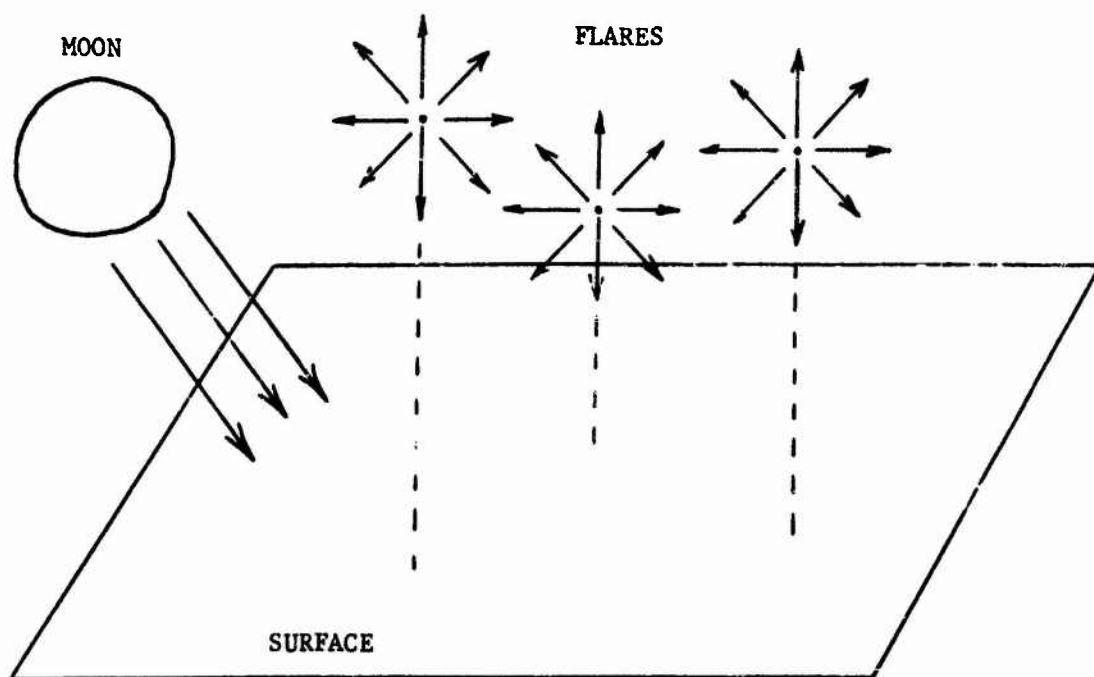


FIGURE 38. NATURAL AND ARTIFICIAL ILLUMINATION CONFIGURATION

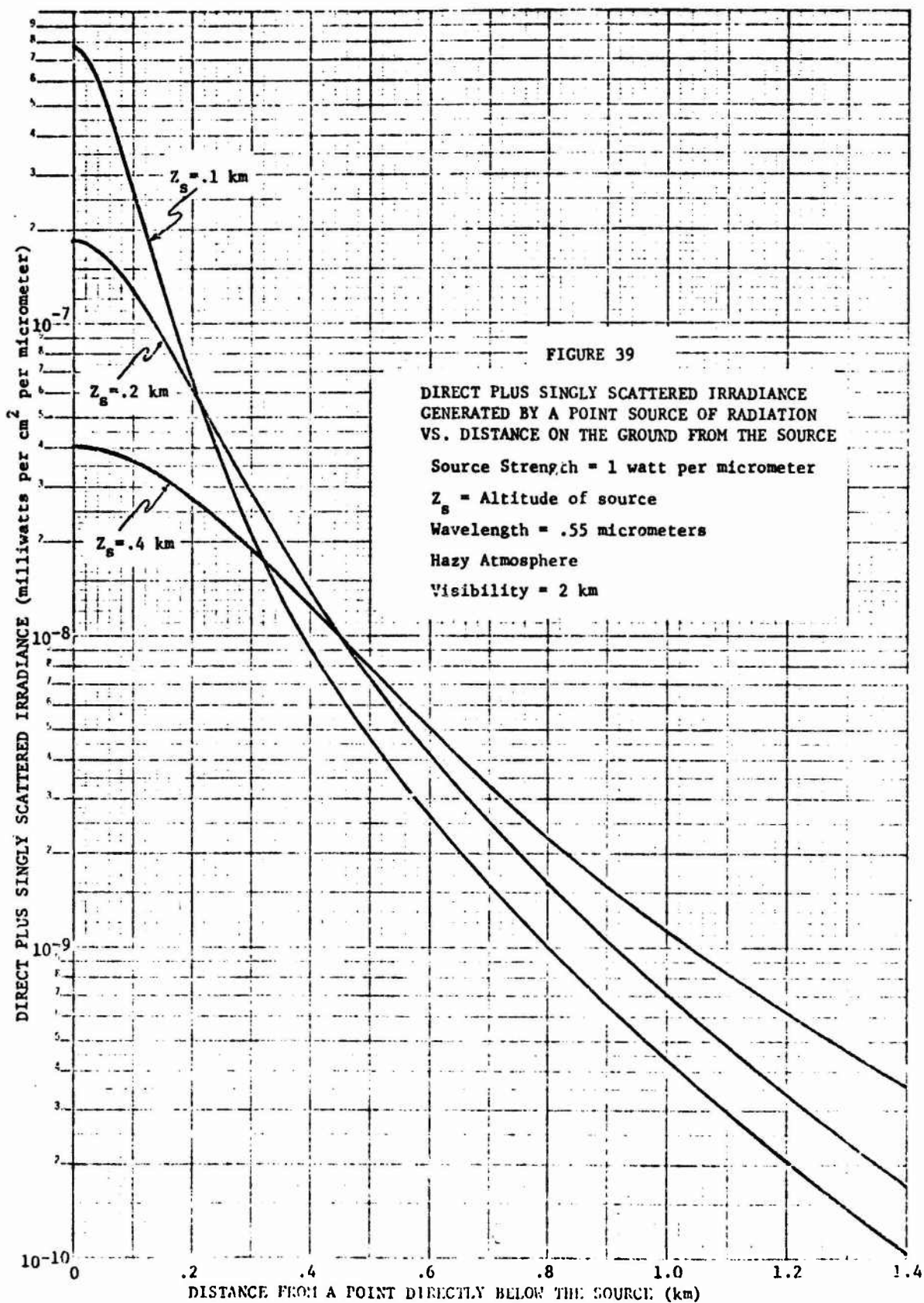
artificial flares illuminating the surface. The moonlight is the result of an extraterrestrial lunar irradiance being scattered by the atmosphere. The scattering is multiple scattering and we also include the effect of reflection from the surface. For the flares we calculate the directly attenuated and the singly scattered components.

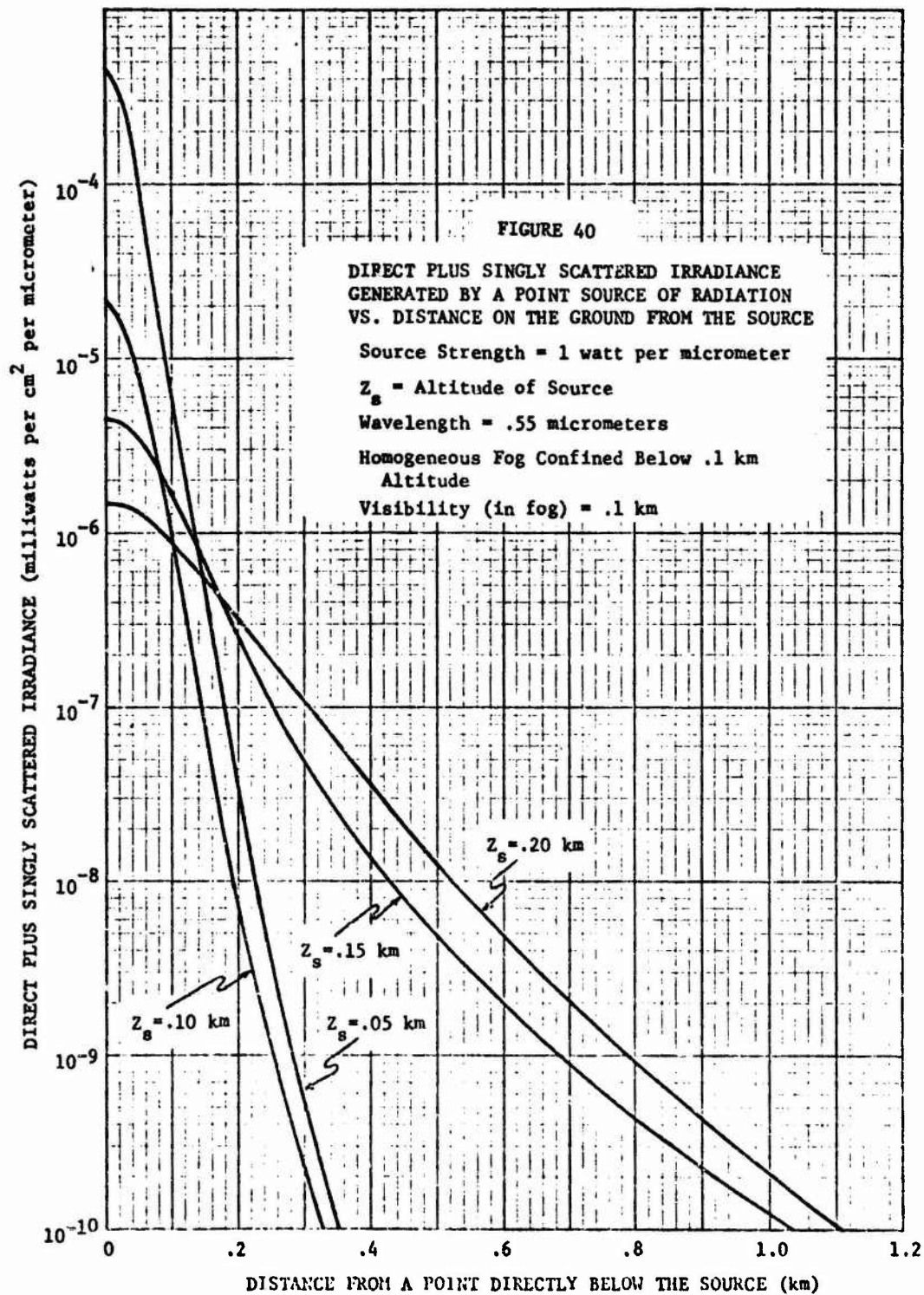
First, we should consider a single flare in a hazy atmosphere at three different altitudes. The total (direct plus singly-scattered) irradiance is illustrated in Figure 39. The results are normalized to a spectral power output of one watt per micrometer. Any other flare output is just multiplied by these values. It is interesting to note that for the higher flares the irradiance is less than for lower flares when one is near the origin (directly beneath the flare). At greater distances from the origin, however, it is reversed. This is due to the fact that the lower flares are more deeply embedded in the heavy haze layer near the surface where more scattering occurs.

We now look at the case of a uniform fog which has a constant profile up to an altitude of 0.1 km. The visibility is only 100 meters. This case is illustrated in Figure 40. Here we see the same effect as in the haze except that it is more severe, i.e., the lower sources provide more illumination at greater distances than the higher sources. An exception is to be noted however, for the very low source of 0.05 km. The other three sources are above the fog and scatter the radiation more, whereas the lowest source lies within the fog and the radiation is attenuated strongly.

Figure 41 depicts the case of a much heavier fog. Here we see the same effect as before only more so. The visibility in this case is 10 meters.

We can now look at the effect of an altitude variation of the source. Considering the 100 meter visibility fog the effect of this variation is shown in Figure 42. It should be noted that when we are at the origin the irradiance decreases monotonically as the source moves farther away. If, however, we are at greater distances along the surface then the





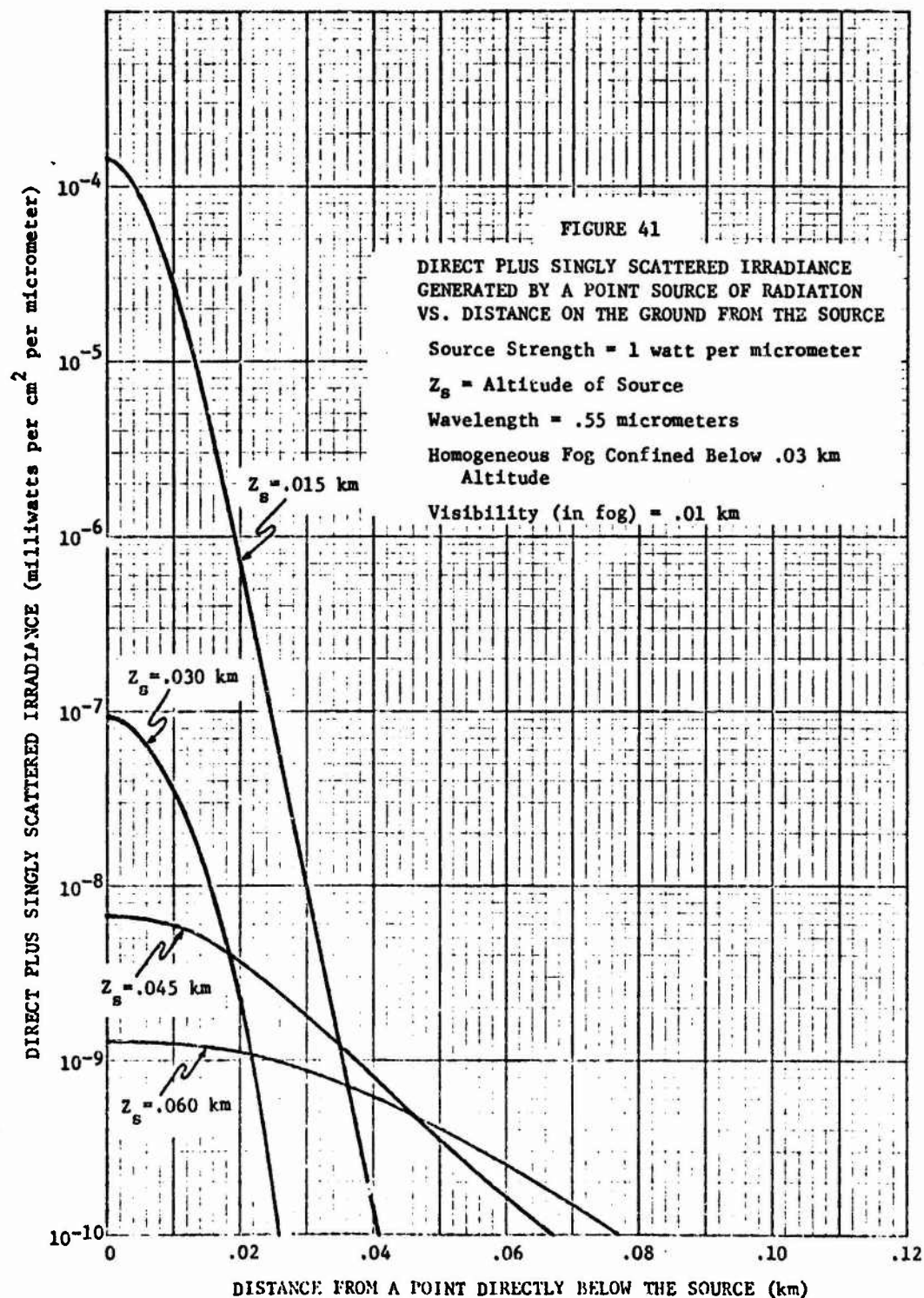
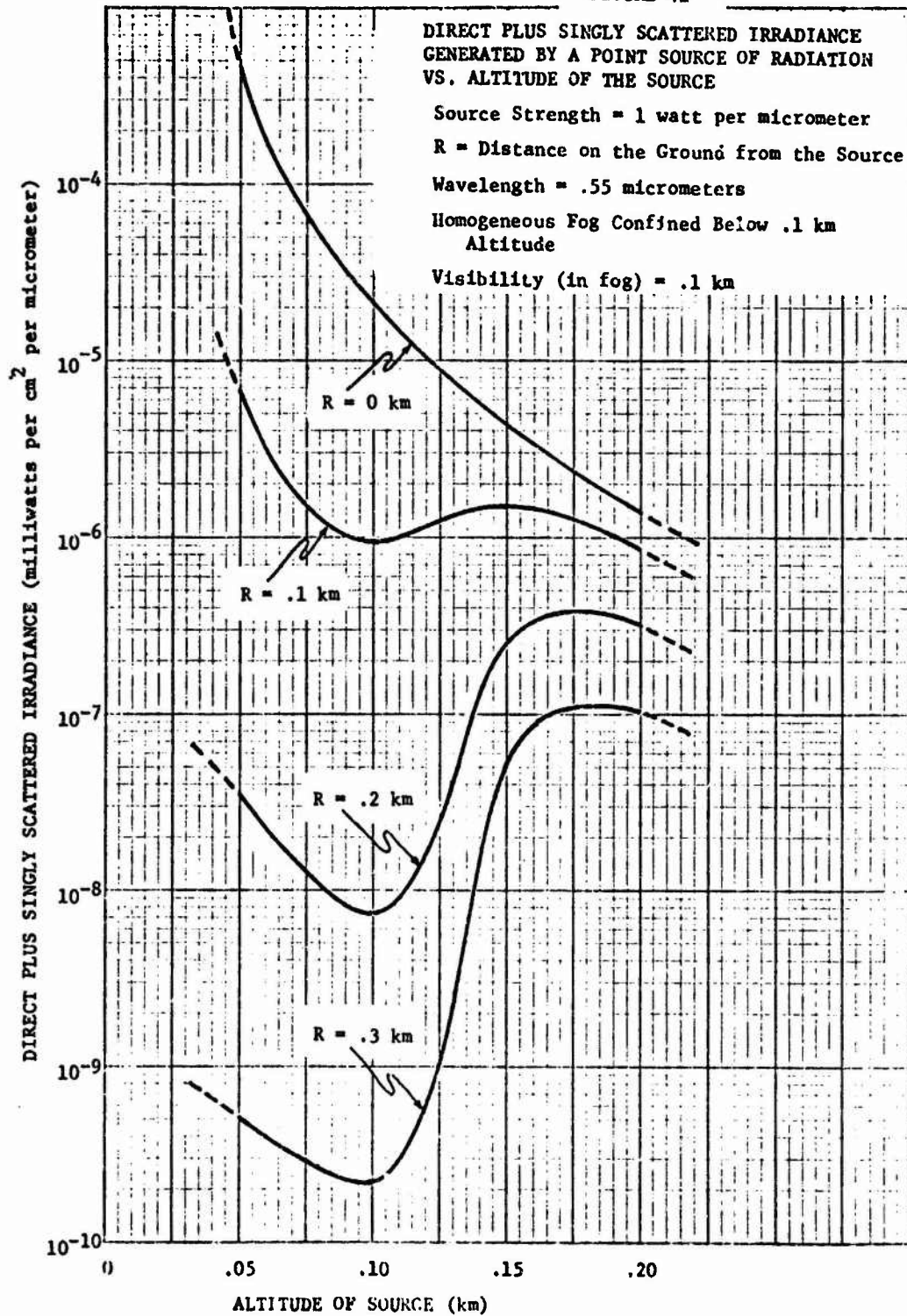


FIGURE 42



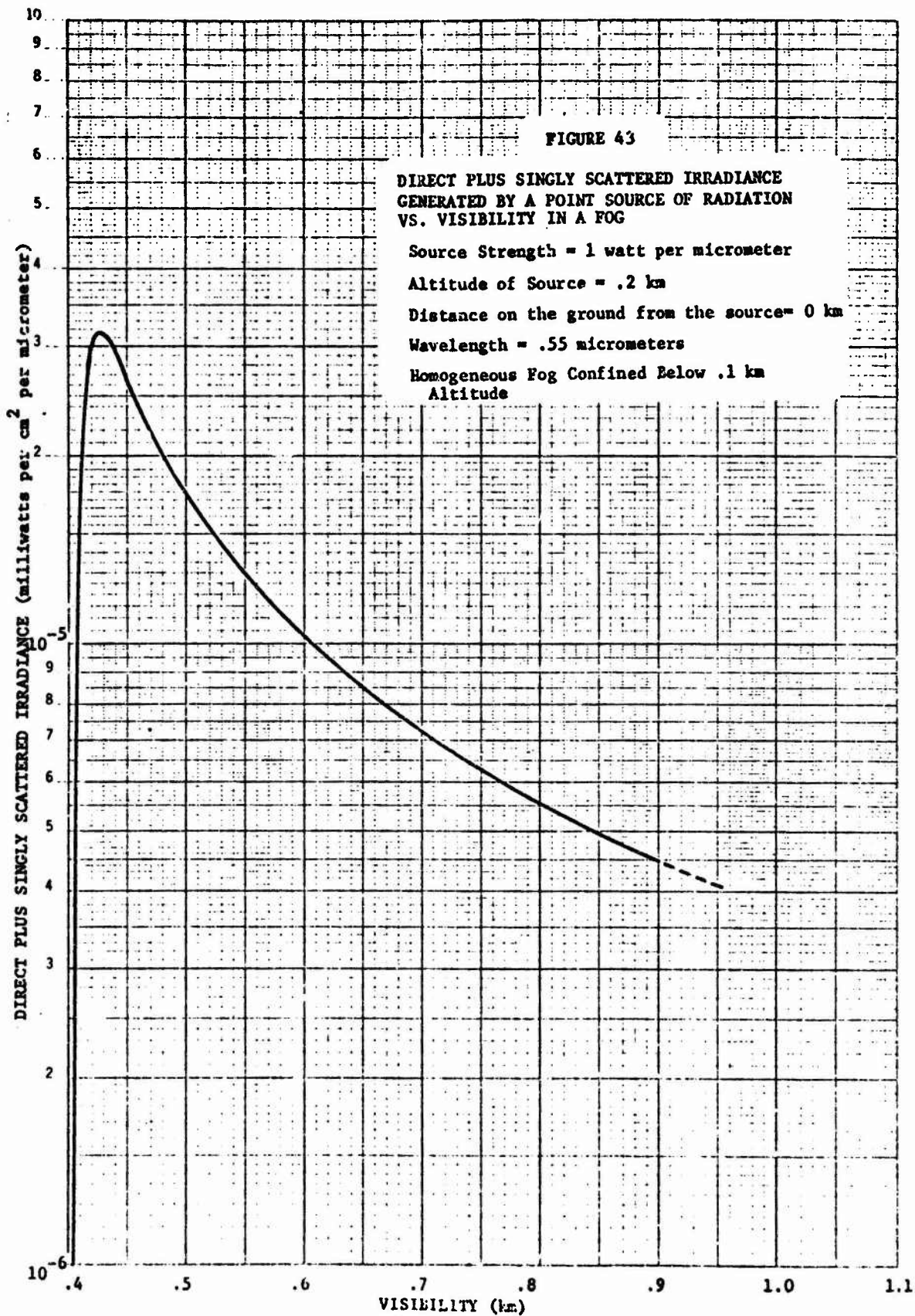
irradiance decreases down to a minimum value, then increases to a maximum and finally decreases monotonically thereafter. Here we are seeing the trade-off between attenuation and scattering. For low altitude sources the radiation is primarily being attenuated, hence the decrease. As the source height increases the singly-scattered radiation is more important and the irradiance begins to increase. There is a limit to its increase, of course, since eventually we have a source well above the fog layer and the amount of radiation decreases as the inverse square of the distance from the source. Therefore, a peak value is reached and a monotonic decrease proceeds from that point on.

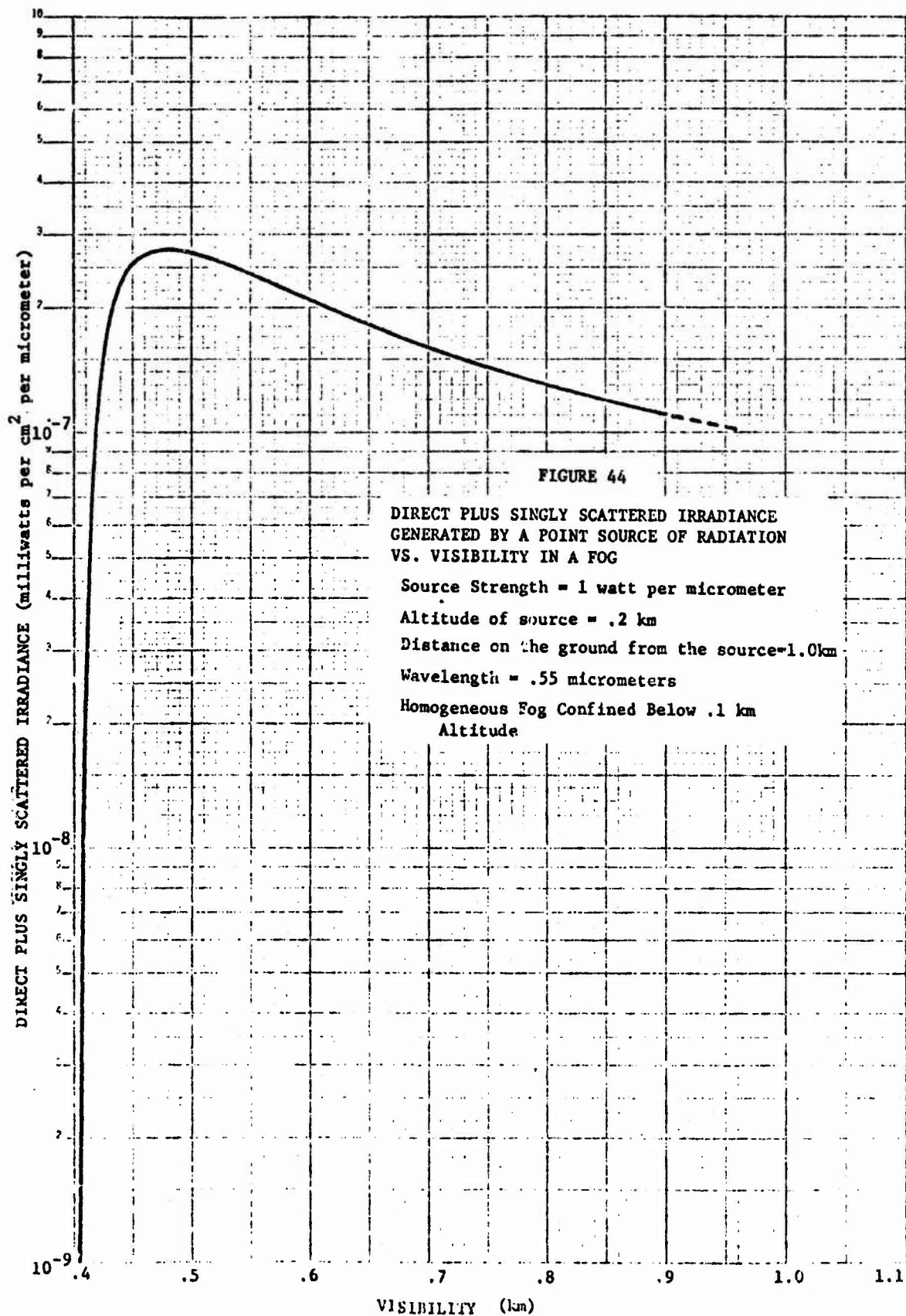
We shall now consider the case of a fixed point source at an altitude of 200 meters embedded in a fog with varying visibility. This is illustrated in Figure 43. For very low visibilities the attenuation is quite strong and almost no radiation arrives at the surface. As the visibility increases there is less attenuation and hence a sharp increase in irradiance occurs. However, as the visibility continues to increase the scattered radiation decreases and therefore the total irradiance decreases.

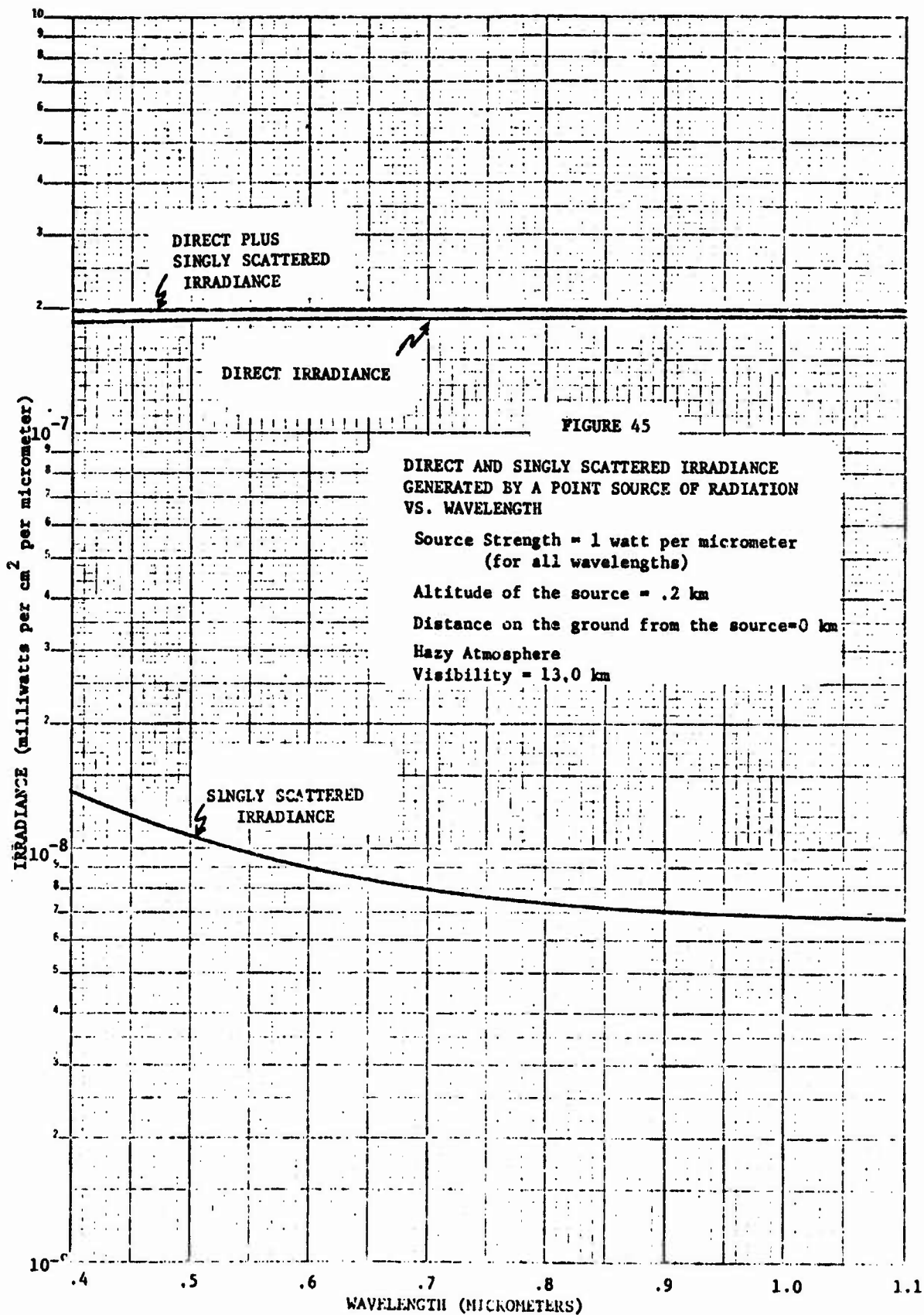
Figure 44 illustrates the same effect for a distance of 1 km from the source. The same basic variation occurs as in the previous case except the total magnitude is less.

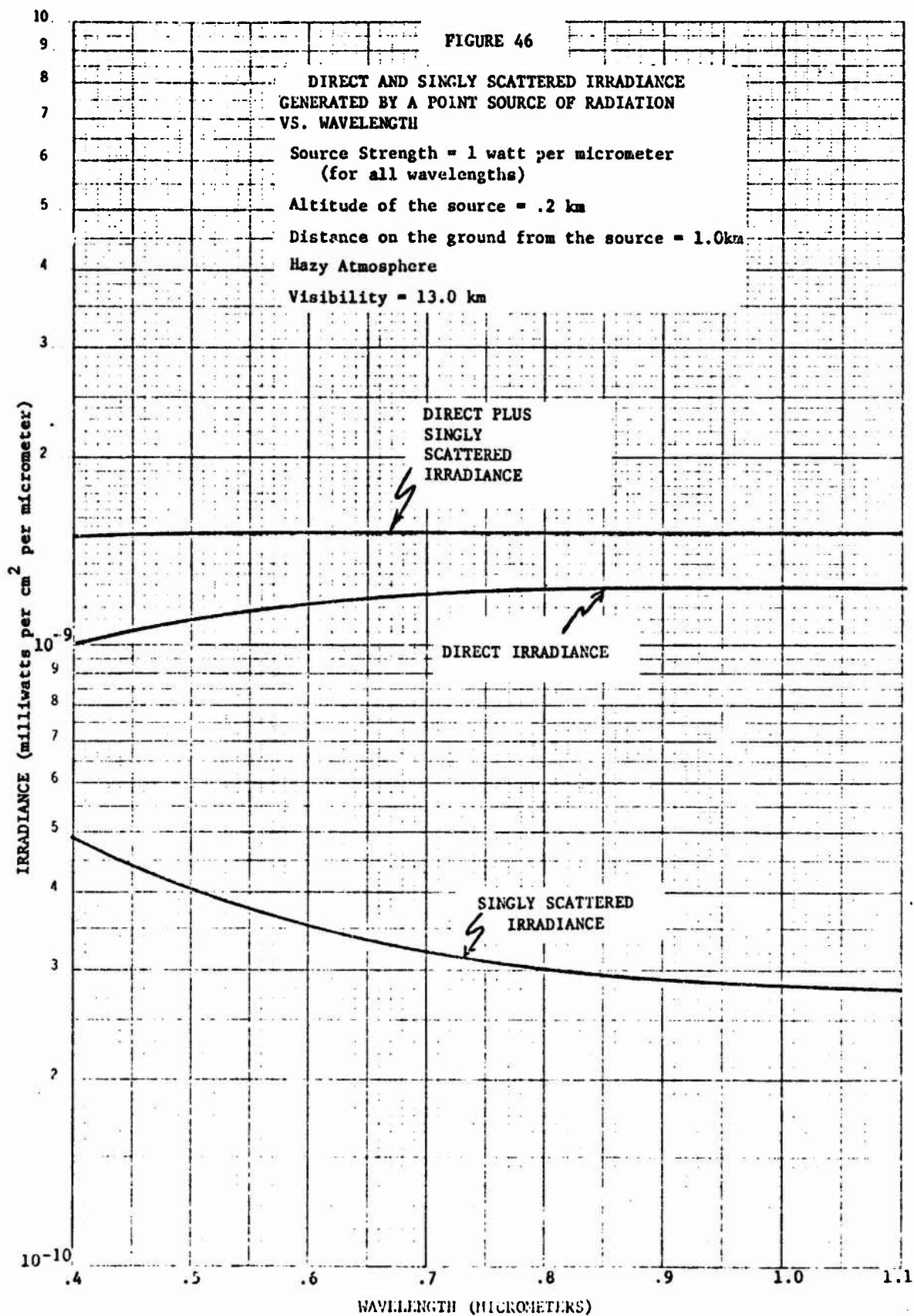
We should investigate the spectral dependence of the irradiance. We consider a spectrally flat (white) flare first in order to see the spectral dependence of the atmosphere. Figure 45 illustrates this variation for a hazy atmosphere with a visibility of 13 km. There is little spectral variation in the directly attenuated irradiance but the singly scattered component does decrease monotonically with increasing wavelength.

Figure 46 illustrates the same dependence except for a distance of one kilometer from the origin. Since we are farther from the source the attenuation and scattering is greater, hence the greater degree of spectral dependence.









Figures 47 and 48 demonstrate similar spectral variations for fogs instead of hazes. Since fog droplets are much larger than the particulates in a haze the spectral dependence is much less as we saw in Section 4.

We can now consider the spectral variation for actual flares. Data were provided us on actual flare spectra by Picatinny Arsenal. The spectra are presented in Figures 49 and 50. The change in the actual flare spectrum for Mark 45 flare is illustrated in Figure 51 for a hazy atmosphere. The direct and singly-scattered irradiance at first appear to be the same. Closer inspection indicates, however, that the direct irradiance is slightly greater in the infrared relative to the singly-scattered irradiance.

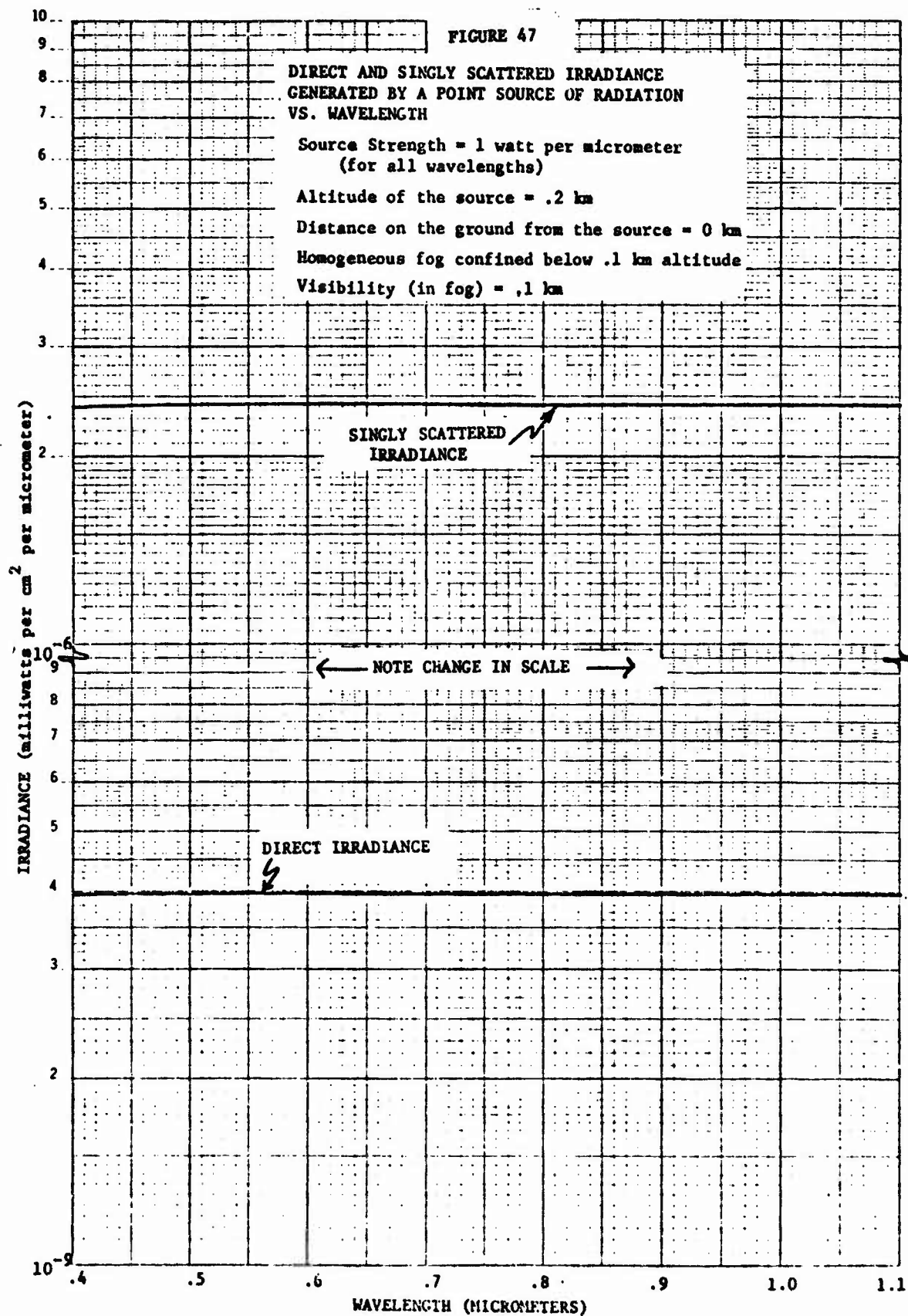
Summarizing these results, we can say that for "clean" fogs in which there are no absorbing contaminants with an intrinsic spectral dependence, then the spectral variation in irradiance is very small. For hazes or fogs contaminated with dust particles the spectral variation could be quite different. These atmospheric states should be investigated.

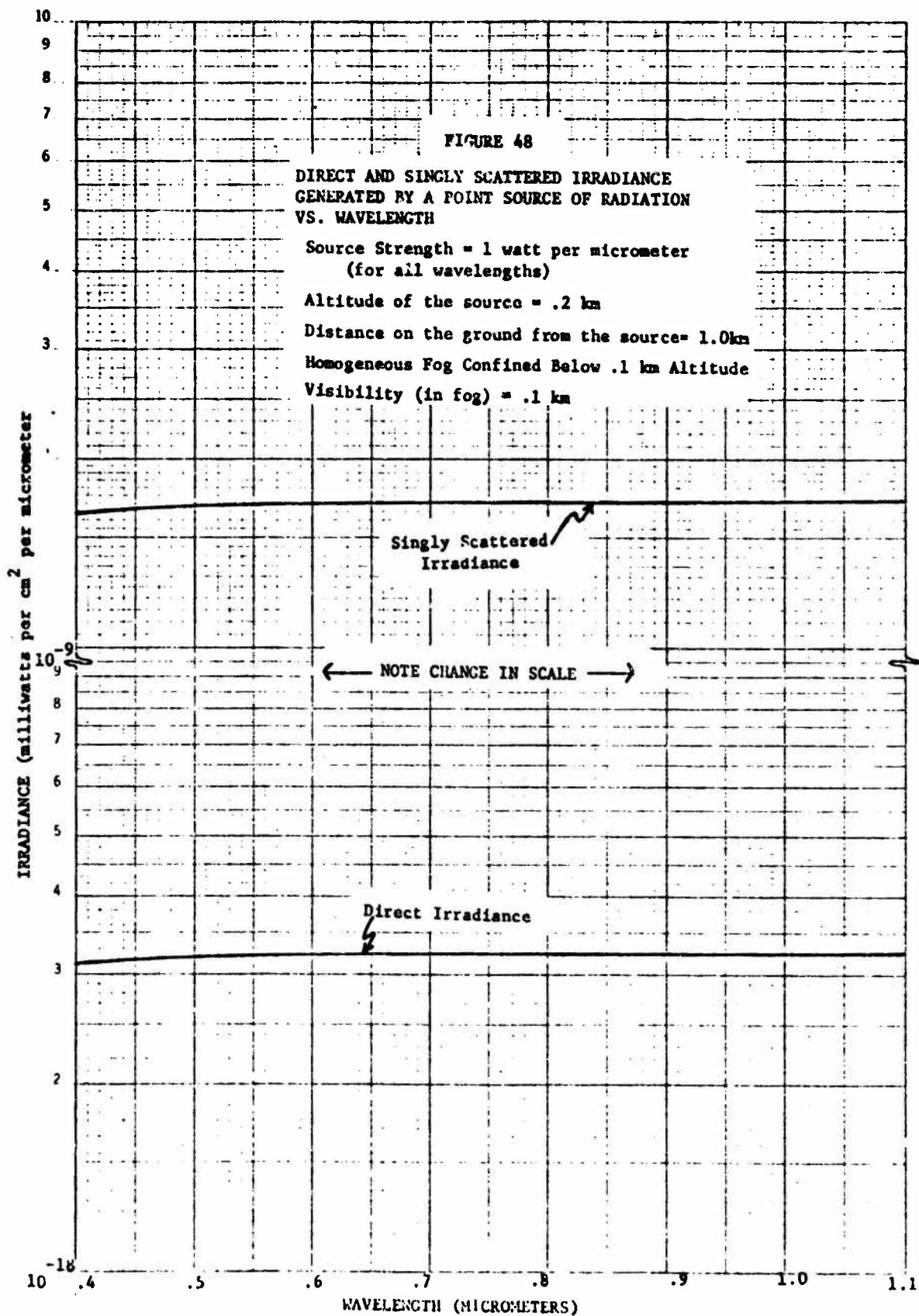
Next, we shall investigate multiple flares in a realistic nighttime environment.

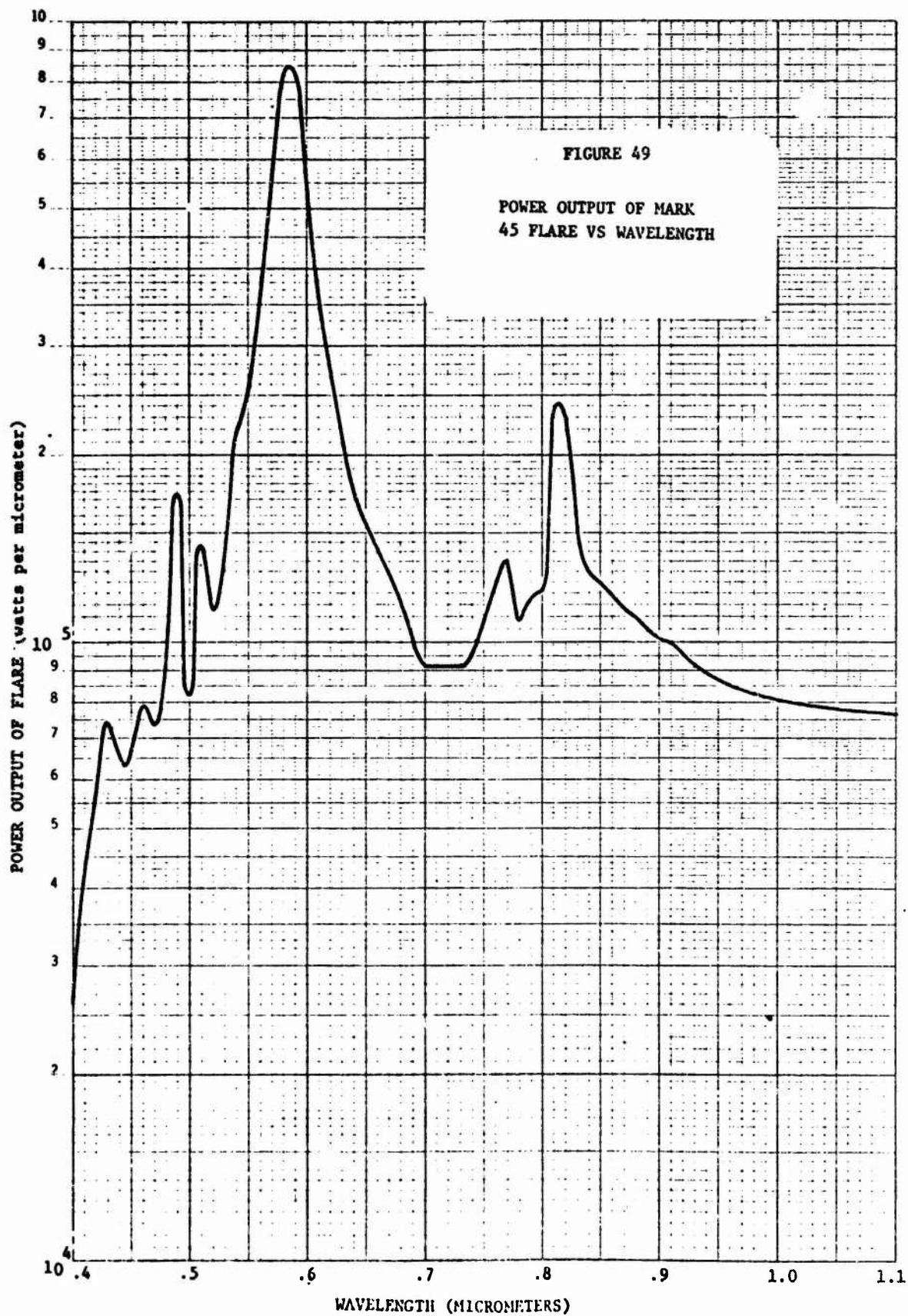
First, we shall consider three flares in a right triangle configuration as illustrated in Figure 52. They are at altitudes of 0.2 km, 0.1 km, and 0.4 km in a very hazy atmosphere with a visibility of 2 km. It should be noted that the highest flare has a high contour closer to the center than for the other flares. This effect was explained in the description of the single-flare graphs.

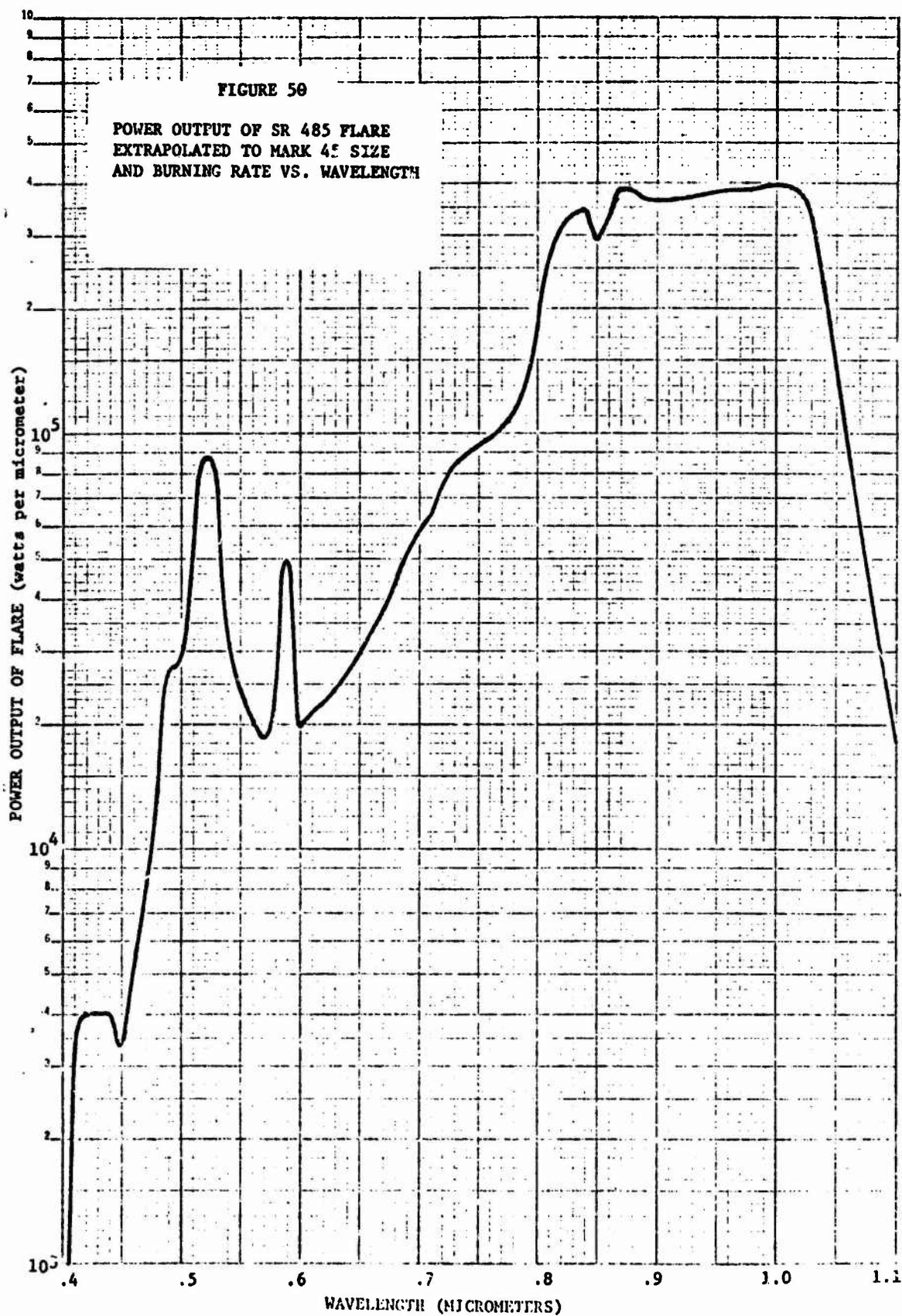
Figure 53 illustrates the contours for the same situation as in Figure 52 except that the flares are twice as far apart.

We can now look at the case of a fog. Figure 54 shows three flares in a foggy atmosphere. The fog has a constant profile up to a height of 100 meters. One flare is at an altitude of 50 m, another at the top of the fog layer, and the third lies 50 meters above the fog layer. Here we see a very interesting effect. The high-altitude flare produces a wide









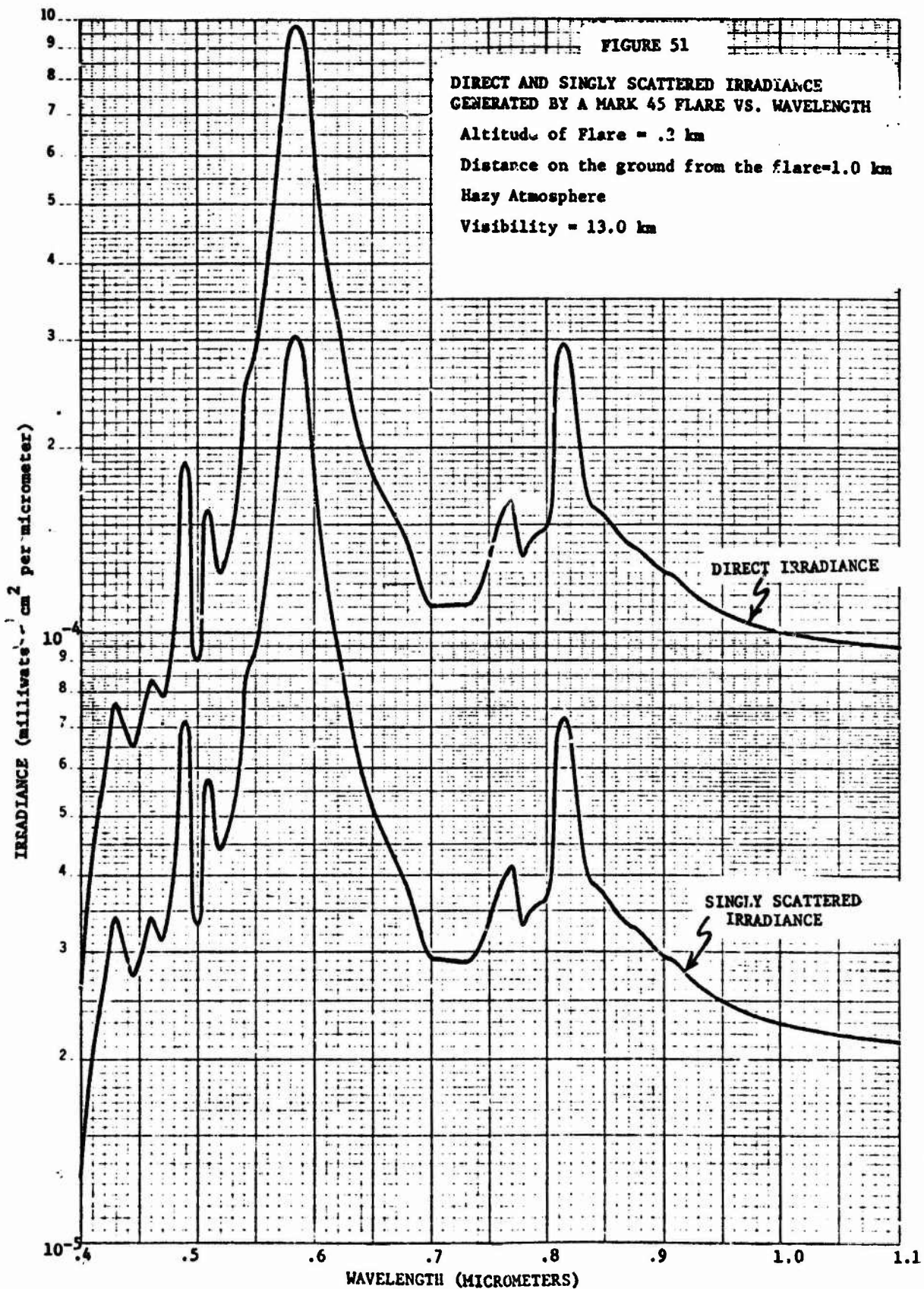
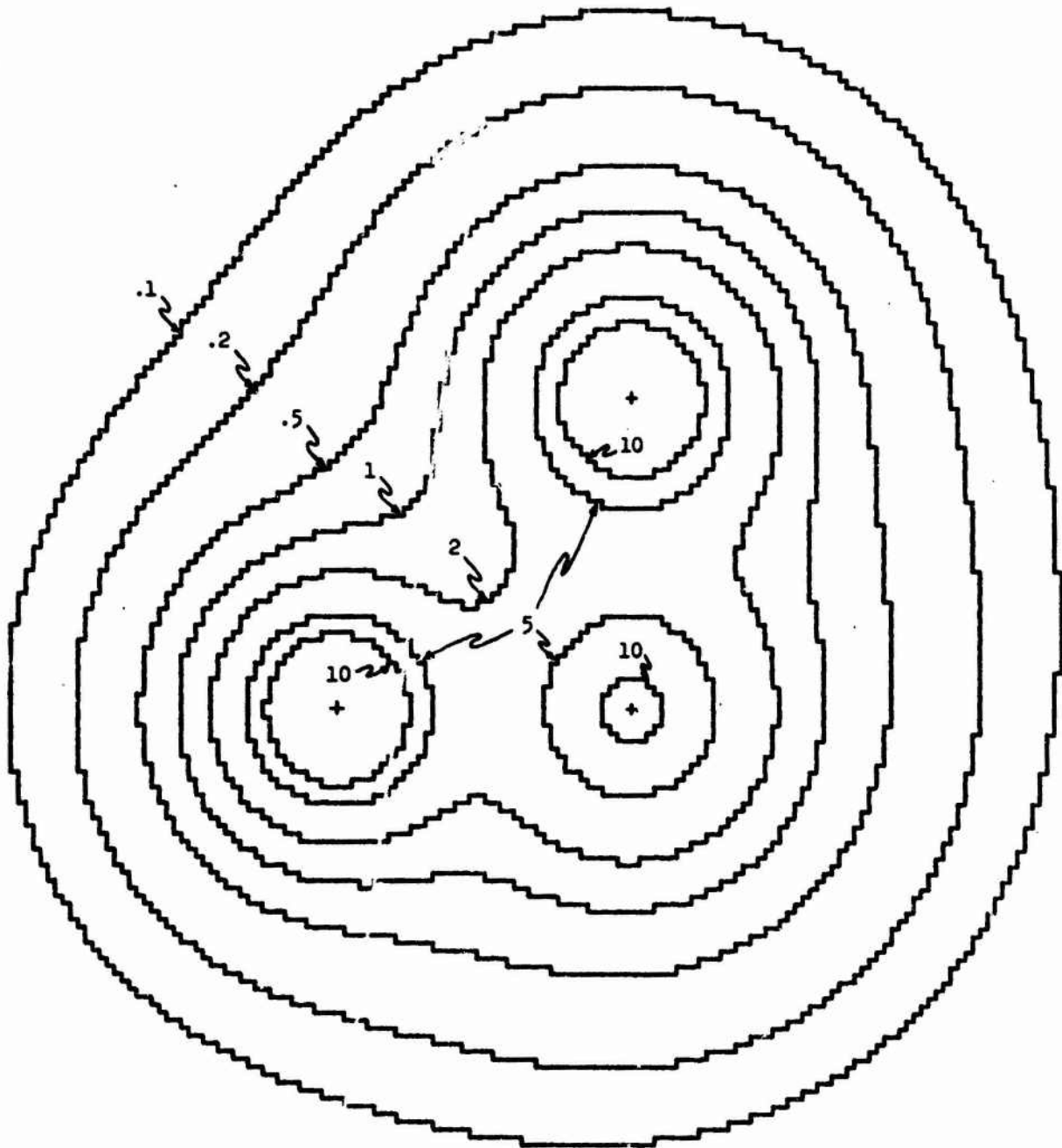


FIGURE 52
 CONTOURS OF CONSTANT DIRECT PLUS SINGLY SCATTERED IRRADIANCE
 GENERATED BY THREE MARK 45 FLARES

Wavelength = .55 micrometers
 Hazy Atmosphere
 Visibility = 2 km

Altitude of Flares = .2 km
 .1 km .4 km



Contour levels are in units of 10^{-3} milliwatts per cm^2 per micrometer

Scale = .5 km per inch

FIGURE 53

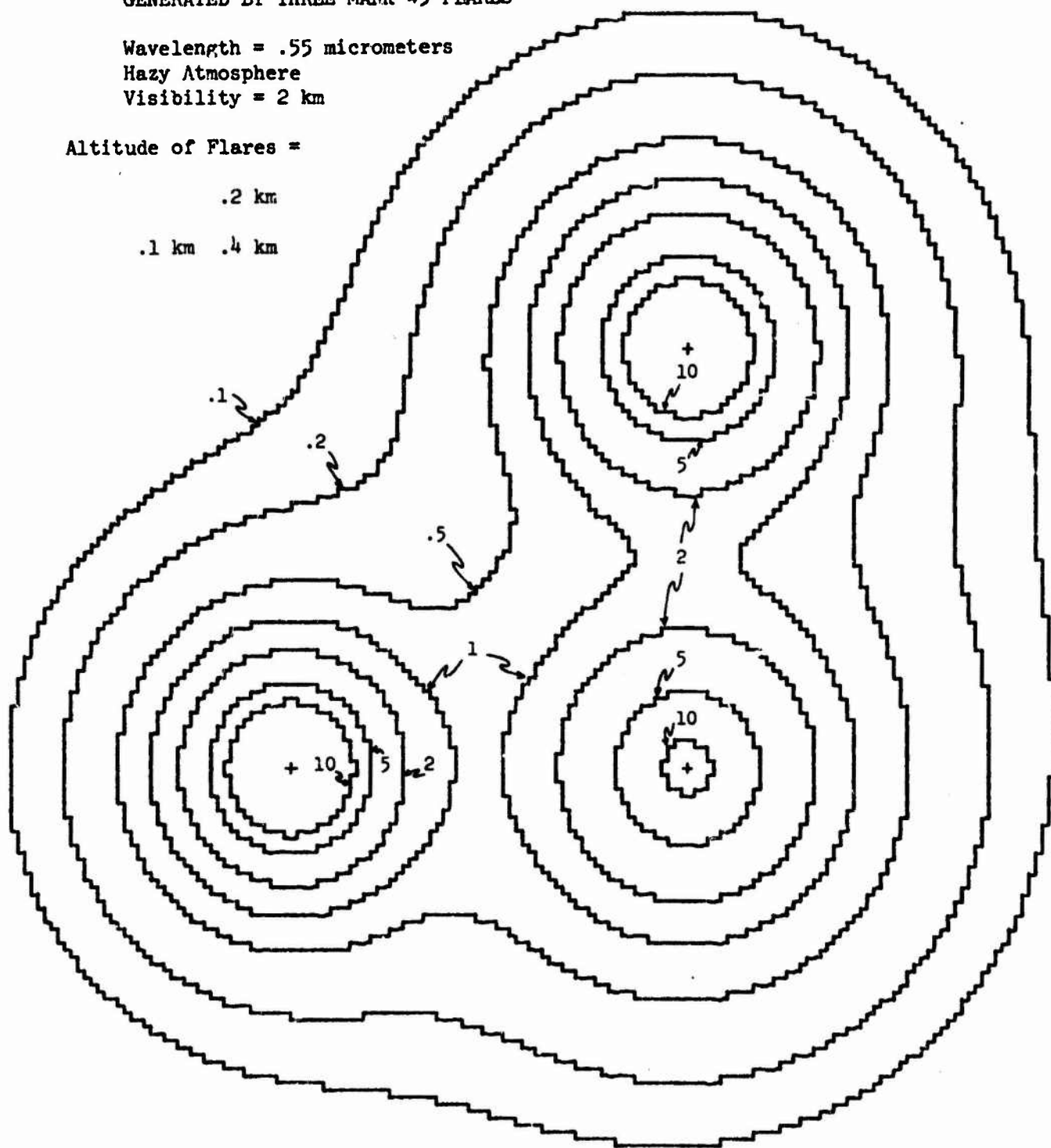
CONTOURS OF CONSTANT DIRECT PLUS SINGLY SCATTERED IRRADIANCE
GENERATED BY THREE MARK 45 FLARES

Wavelength = .55 micrometers
Hazy Atmosphere
Visibility = 2 km

Altitude of Flares =

.2 km

.1 km .4 km



Contour levels are in units of 10^{-3} milliwatts per cm^2 per micrometer

Scale = .5 km per inch

FIGURE 54

CONTOURS OF CONSTANT DIRECT PLUS SINGLY SCATTERED IRRADIANCE
GENERATED BY THREE MARK 45 FLARES

Wavelength = .55 micrometers

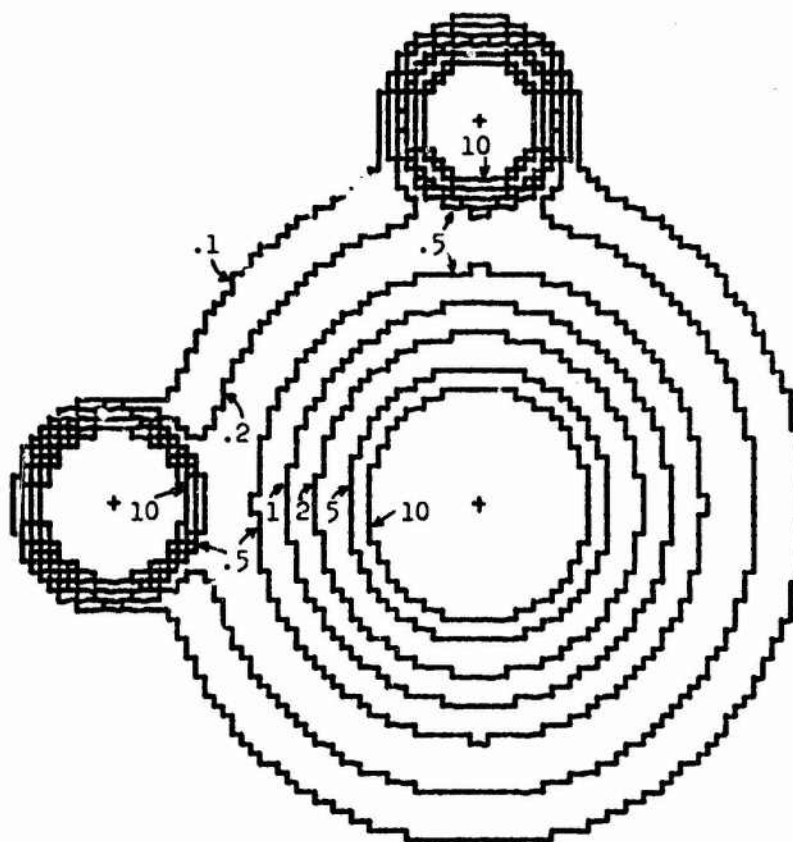
Altitude of Flares = .10 km

Homogeneous Fog Confined Below .1 km

Altitude

.05 km .15 km

Visibility (in fog) = .1 km



Contour levels are in units of 10^{-3} milliwatts per cm^2 per micrometer

Scale = .5 km per inch

distribution of radiation over an extended area whereas the lower altitude flares have a much more concentrated distribution. This is due to the fact that scattering is a more important effect than attenuation for the higher altitude case.

Figure 55 illustrates the distribution due to four flares in a fog. As in the previous case, the two flares above the fog layer produce a more extended distribution than the two flares below the fog layer.

Finally, in Figure 56 we present four flares in an extremely dense fog with a visibility of only 10 meters. The height of the fog is 30 m and two of the flares are within the fog whereas two are above. Again, we see the same effect as before. The lowest flare decreases most rapidly.

The flares are normalized to one watt per micrometer and the values of natural irradiance are given in Section 5. Hence any flare output can be compared with any natural background.

6.5 ILLUMINATION MODEL

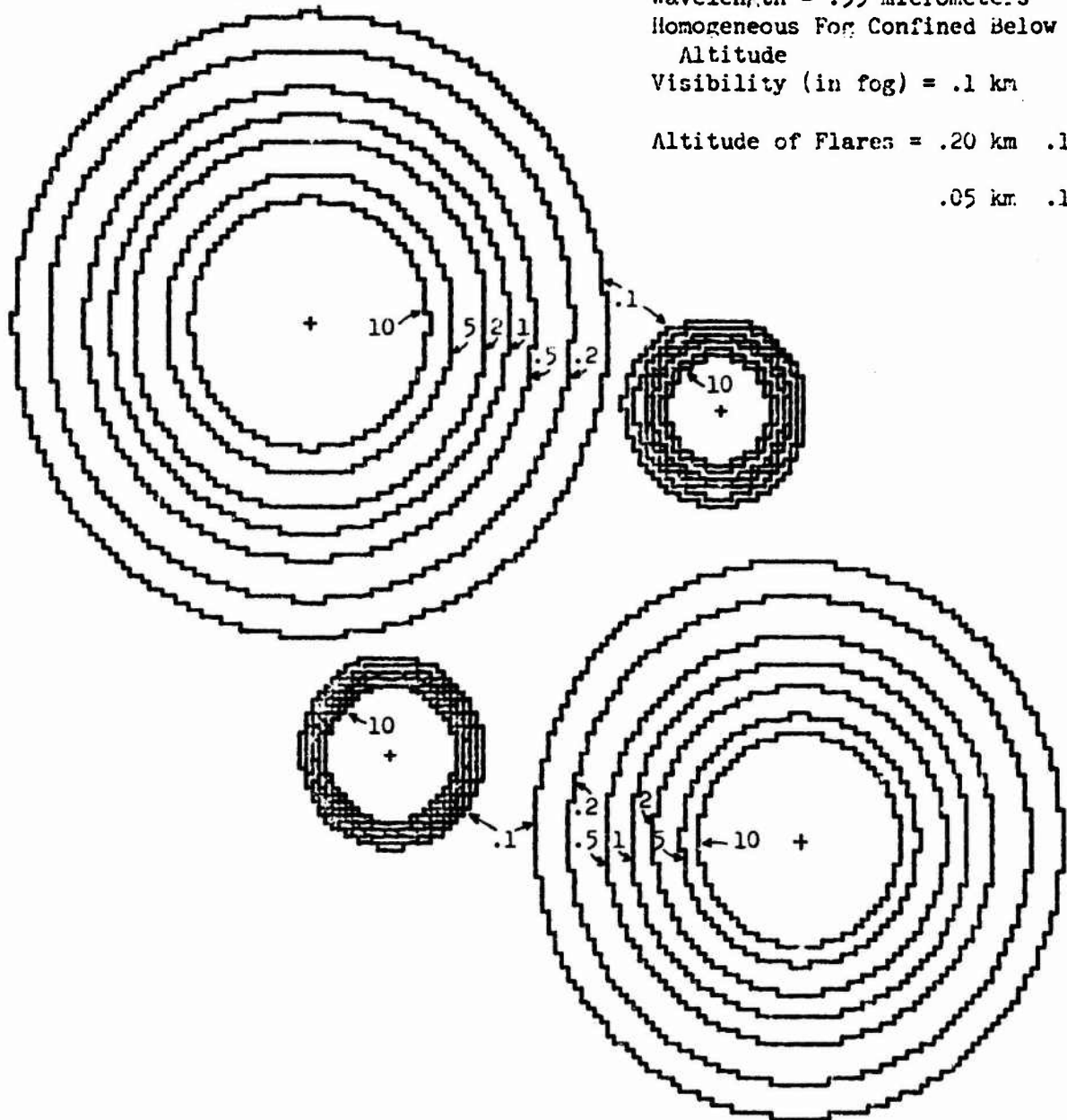
A complete model for the determination of the illumination of a scene as a result of natural and artificial radiation sources can be developed based upon the analysis in Sections 5 and 6. Figure 57 is meant to illustrate a more complete model for surface illumination. It should not be interpreted as a single computer program. The present capability is as follows: The scene can be defined in terms of surface reflectance for a uniform, flat terrain. Any number of point sources may be used. Meteorological data involving atmospheric pressure, horizontal visibility, and fog height can be specified to determine the atmospheric state. The date and time should be specified in order to determine the extraterrestrial solar or lunar irradiance at the top of the atmosphere and the solar or lunar zenith angle. Knowing the wavelength and the appropriate meteorological data, the optical parameters such as attenuation coefficients and optical depth can be calculated and these parameters are then used in the point source or natural source model to calculate the natural and artificial radiation fields.

FIGURE 55

CONTOURS OF CONSTANT DIRECT PLUS SINGLY SCATTERED IRRADIANCE
GENERATED BY FOUR MARK 45 FLARES

Wavelength = .55 micrometers
Homogeneous Fog Confined Below .1 km
Altitude
Visibility (in fog) = .1 km

Altitude of Flares = .20 km .10 km
.05 km .15 km



Contour levels are in units of 10^{-3} milliwatts per cm^2 per micrometer

Scale = .5 km per inch

FIGURE 56

CONTOURS OF CONSTANT DIRECT PLUS SINGLY SCATTERED IRRADIANCE
GENERATED BY FOUR MARK 45 FLARES

Wavelength = .55 micrometers

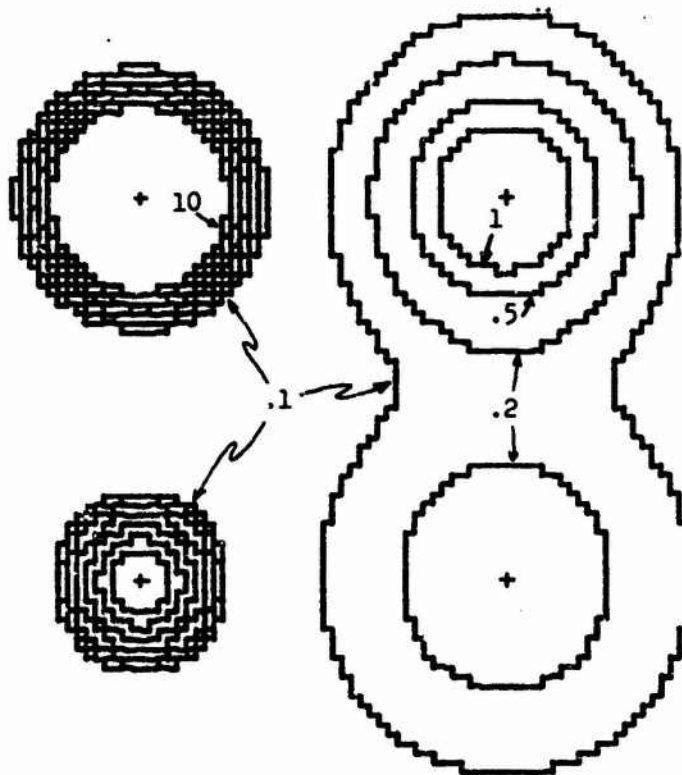
Altitude of Flares = .015 km .045 km

Homogeneous Fog Confined Below .03 km

Altitude

.030 km .060 km

Visibility (in fog) = .01 km



Contour levels are in units of 10^{-3} milliwatts per cm^2 per micrometer

Scale = .05 km per inch

ILLUMINATION MODEL

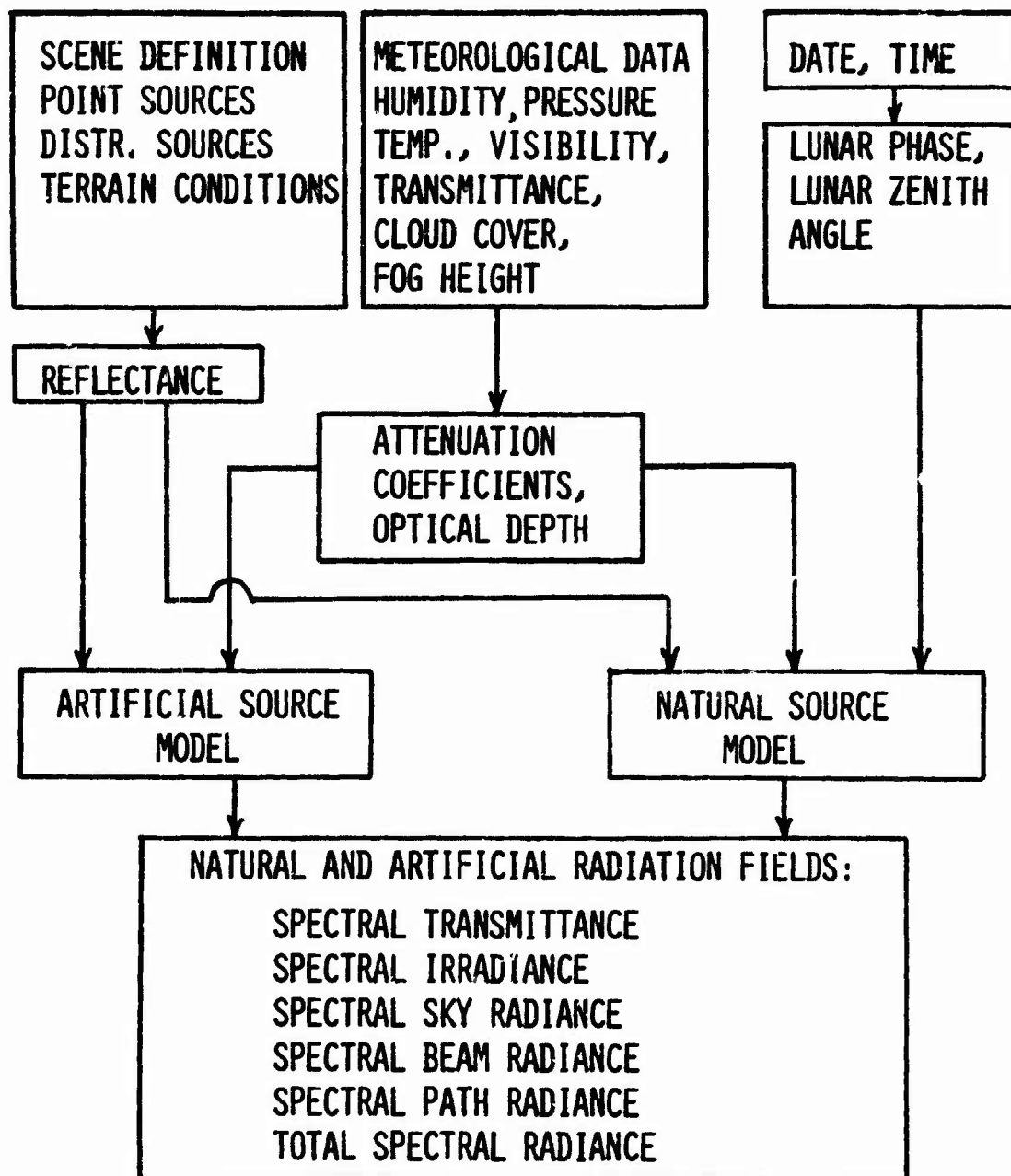


FIGURE 57. ILLUMINATION MODEL FOR NATURAL AND ARTIFICIAL SOURCES

4

The present models can be generalized to include gaseous absorption and multiple scattering as well as the effects of reflection from non-Lambertian surfaces. In addition, further modeling of cloud layers should be conducted in order to understand how the illumination on the surface changes as flares penetrate the cloud layer. Also, the basic mathematical procedures have already been developed which will allow one to calculate the illumination due to distributed (non-point) sources such as fires, city lights, mountains, and other natural or man-made sources.

COMPUTATIONAL METHODS

The mathematical model used to calculate the direct and singly scattered irradiance generated by an isotropic point source is in principle an exact formulation. However, some approximations and simplifications are required to adapt the solution of the 3-fold integral equation for the singly scattered irradiance to the computer. This equation is written as follows:

$$E_{ss} = \frac{S\omega_o}{16\pi^2} \int_0^1 \int_0^{2\pi} \int_0^\infty \frac{\kappa(z) p(\cos \chi) e^{-[\tau_o - \tau(z)]/\mu}}{D^2 \times 10^7} \times$$

$$e^{-\left[\frac{\tau(z_s) - \tau(z)}{z - z_s} \right]} D \, dz \, d\phi' \, d\mu' \quad (83)$$

S is the source strength in watts per micrometer, ω_o is the single scattering albedo, $\kappa(z)$ is the vertical attenuation coefficient, $p(\cos \chi)$ is the scattering phase function, $\tau(z)$ is the optical depth, μ is the cosine of the angle between a vertical line and a line drawn between the scattering center and the irradiated spot on the ground (at a distance R from a point on the ground directly below the source), z_s is the altitude of the source, D is the distance in kilometers from the source to the scattering center, ϕ' and μ' are angular variables of integration for the spherical coordinate system described in Section 7.2, and the factor of 10^7 in the denominator converts the units of the result to milliwatts per cm^2 per micrometer.

7.1 SIMPLIFICATIONS AND APPROXIMATIONS WHICH REDUCE COMPUTATIONAL EXPENSE

The simplifications and approximations which are used in the computer solution for E_{ss} fall into two major categories. The first of these categories is concerned with making the evaluation of the equation economical. In particular, the aerosol or fog scattering phase functions used in the computations are determined by linear interpolation from values in a table. This result is then combined with the Rayleigh phase function (which is calculated analytically), with each phase function being weighted by the ratio of its scattering coefficient to the total scattering coefficient. This interpolation and combination technique avoids the very costly alternative of calculating the phase function from a polynomial series (which, since it requires a great many terms to be accurate, has been done just once to generate the interpolation table). The interpolation is done in two variables: scattering phase angle and wavelength. The interpolation with respect to wavelength is done only once at the beginning of the computations, and this result is then interpolated with respect to the scattering phase angle as required.

The vertical attenuation coefficient, $\kappa(z)$, and the optical depth, $\tau(z)$, are actually functions of wavelength and visibility as well as altitude. For fogs $\kappa(z)$ and $\tau(z)$ are computed analytically as functions of visibility and altitude, but their dependence on wavelength is determined by interpolation from a table, representing either a selective fog or a stable fog, as specified by an input to the computer program. The analytical dependence of $\kappa(z)$ and $\tau(z)$ on altitude is selected among four alternatives according to another program input. For hazes (aerosol scattering) $\kappa(z)$ and $\tau(z)$ are computed from a piece-wise analytical representation of Elterman's model. The dependence of $\kappa(z)$ and $\tau(z)$ on wavelength is first calculated using an 8th order polynomial. For altitudes less than 5 km or greater than 26 km an exponential variation with altitude is assumed, while for altitudes between 5 km and 26 km another 8th order polynomial is used to represent the altitude dependence of the model.

This altitude dependent part is then multiplied by the wavelength dependent part to obtain $\kappa(z)$ and $\tau(z)$. The visibility enters the calculations (in a straightforward analytical way) only for altitudes less than 5 km. The values of $\kappa(z)$ and $\tau(z)$ determined above are added to the values of $\kappa(z)$ and $\tau(z)$ for Rayleigh scattering, which are calculated analytically. For hazes the effects of ozone absorption are also included as determined by linear interpolation from tables in wavelength and altitude.

It is desirable to perform the integration with respect to z (altitude) as the innermost integral (to determine radiance as a function of ϕ' and μ' as well as to minimize the number of calculations in the innermost integral), yet it is not desirable to recompute $\kappa(z)$ and $\tau(z)$ during each cycle through this integral. Hence, as much as possible the expressions in the equation which involve $\kappa(z)$, $\tau(z)$, z , and constant factors are calculated once at the beginning of the computer program and are saved in an array from which they may be readily obtained when they are needed.

The variables μ and μ' are related as follows:

$$\mu = \mu' \cos \alpha + \sqrt{1 - \mu'^2} \sin \alpha \cos \phi' \quad (84)$$

while

$$D = \sqrt{P^2 + \left(\frac{z}{\mu}\right)^2 - 2P \frac{z}{\mu} \mu'} \quad (85)$$

and

$$\cos \chi = \frac{P\mu' - \frac{z}{\mu}}{D} \quad (86)$$

where P is the distance between the source and the irradiated spot on the ground, α is the angle between a vertical line and a line drawn between

the source and this irradiated spot, z is the altitude of the scattering center, and χ is the scattering phase angle. (Note: The limits of the integration in ϕ' and μ' must correspond to integration over the hemisphere specified by $0 \leq \mu \leq 1$. This is accomplished by changing the signs of both μ and μ' whenever the calculation of μ from ϕ' and μ' yields a result less than zero. D and $\cos\chi$ are then calculated using these new values of μ and μ' . This corresponds to a reflection of the coordinates ϕ' and μ' through the origin.) During the integral with respect to ϕ' , $\cos\phi'$ has to be recomputed for each change in ϕ' . Letting the increment in ϕ' be represented by $\Delta\phi'$, we use the trigonometric identities for the sine and cosine of the sum of two angles to compute successive values for $\sin\phi'$ and $\cos\phi'$. This requires that we compute $\sin\Delta\phi'$ and $\cos\Delta\phi'$ once and then take appropriate sums and differences of products between $\sin\phi'$ or $\cos\phi'$ and $\sin\Delta\phi'$ or $\cos\Delta\phi'$:

$$\cos(\phi' + \Delta\phi') = \cos\phi' \cos\Delta\phi' - \sin\phi' \sin\Delta\phi' \quad (87)$$

$$\sin(\phi' + \Delta\phi') = \sin\phi' \cos\Delta\phi' + \cos\phi' \sin\Delta\phi' \quad (88)$$

Although it appears that one only needs to increment $\cos\phi'$, one must also increment $\sin\phi'$ in order to keep this sequence going. This method for incrementing $\cos\phi'$ is more efficient than calculating $\cos\phi'$ from each new value of ϕ' .

Since the calculation of E_{ss} has bilateral symmetry, one need only integrate for $0 \leq \phi' \leq \pi$ and multiply this result by 2. However, a further simplification is also possible. Since

$$\cos\left(\frac{\pi}{2} - \phi'\right) = \sin\phi' \quad (89)$$

$$\cos\left(\frac{\pi}{2} + \phi'\right) = -\sin\phi' \quad (90)$$

$$\cos(\pi - \phi') = -\cos\phi' \quad (91)$$

the ϕ' integration can be split into four more parts. Hence, we integrate over the range $0 \leq \phi' \leq \frac{\pi}{4}$, but add together four separate results for each value of ϕ' -- the straightforward result corresponding to the equation for μ as a function of ϕ' and μ' as written, and three other results corresponding to replacing $\cos\phi'$ in the equation for μ by $\sin\phi'$, $-\sin\phi'$, and $-\cos\phi'$, respectively. The appropriate substitute values for $\cos\phi'$ are all readily available from the ϕ' incrementing scheme described above.

7.2 SIMPLIFICATIONS AND APPROXIMATIONS WHICH MAKE THE EQUATION SOLUBLE

The second major category of simplifications and approximations used in the calculation of E_{ss} on the computer is concerned with making evaluation of the equation possible. Since the integrals cannot be evaluated analytically in a closed form, some sort of numerical integration method is required. Two basic considerations are of importance here: (1) the choice of a coordinate system, and (2) the method for incrementing the coordinates. The guiding principle in making these two choices is to try to equalize the contributions to the integral corresponding to each discrete combination of the variables of integration. Unfortunately, different source locations and different atmospheric configurations require somewhat different numerical treatments if one desires to minimize computational expense. This led to the development of two separate computer programs, each specialized to a particular subset of the possible configurations of the problem. The differences between these two programs will be discussed below.

The choice of an appropriate coordinate system for the integrals is influenced somewhat by the method chosen for incrementing the variables of integration. As described in Section 7.1 equal increments were chosen for the ϕ' integration. Another incrementing scheme which is relatively straightforward to implement is that of geometrically increasing (or decreasing) increments. According to this scheme the coordinates are incremented in a multiplicative, rather than additive, manner:

equal increments: $z + \Delta z = z + \Delta z$

geometric increments: $z + \Delta z = \alpha_z z$, $\alpha_z > 1$

Each new discrete value of z in this example is obtained by multiplying the previous discrete value by α_z , hence $\Delta z = (\alpha_z - 1)z$ varies in direct proportion to the value of z . With equal increments Δz would be constant. Of course in the z integral required to calculate E_{ss} the range of integration goes from $z = 0$ to $z = \infty$. With either incrementing scheme one would need an infinite number of increments to cover this range. However, the atmosphere is essentially non-existent above 50 km altitude, so this can be used as an upper bound on the range of integration. With geometric increments this still implies that an infinite number of increments are needed. The technique is then to sum the contributions to the integral, starting at the upper bound (e.g. 40 km), and to increment the variable of integration backwards:

$$z - \Delta z = z/\alpha_z , \quad \alpha_z > 1 \quad (92)$$

The running total of these contributions is then compared to each new contribution to determine when this total has more or less converged. (Since Δz keeps getting smaller and smaller, eventually a point is reached at which the integrand, multiplied by Δz , keeps getting smaller and smaller as well -- except for extreme cases in which the integral would not have converged analytically either. Such is never the case for this problem.) When convergence is detected, an analytic approximation to the remainder of the integral is added in to finish the computation. In this case, once convergence is sensed, the integral is assumed to be constant for all remaining values of z .

Since the atmosphere is ordinarily densest close to the ground, an important portion of the scattering of the light from the source occurs at low altitudes. Hence, the treatment of the z integral described above was found to be both useful and economical for some configurations of the problem. In particular one of the two computer programs written to solve

this problem uses the above method and has been found to be especially useful when the source is close to the ground, outside most of the earth's atmosphere, or comfortably above a fog layer. However, if the source is close to a fog layer, immersed in a fog, or in the middle of a hazy atmosphere, the major portion of the singly scattered irradiation comes from scattering centers which are close to the source and which consequently receive more intense radiation from it than scattering centers farther away. In these latter cases one needs to have the smaller increments of the integration occur close to the source. In this instance the z integration is separated into two parts:

$$z + \Delta z = z_s - (z_s - z)/\alpha_z, \quad 0 \leq z < z_s \quad (93)$$

$$z - \Delta z = z_s + (z - z_s)/\alpha_z, \quad z_s < z \leq (z_s + z_{\max}) \quad (94)$$

This latter z integration scheme is used in the other of the two computer programs written to solve this problem. The method used in this second program to terminate the integral series is the same as that described above. It has been found that values of α_z between 1.05 and 1.15, corresponding to 47.2 and 16.5 iterations per decade (order of magnitude), respectively, in general produce results for the z integral which are accurate to within 1% to 5%. This accuracy improves for atmospheres which have gentle variations in density as a function of altitude (e.g. hazes). The above estimates of accuracy are based on results from integration by the trapezoidal rule (by which the values of the integrand at the endpoints of each Δz interval are averaged and are then multiplied by Δz). The trapezoidal rule is used for all the integrals in both of the computer programs written for this problem. The different methods for handling the integration with respect to z (altitude) are the only difference between these two programs.

Since the scattering phase functions used in this problem tend to scatter major amounts of radiation in the forward and backward directions,

much of the singly scattered radiation tends to follow paths close to a line connecting the source with the irradiated spot on the ground which is of interest. Consequently, it is desirable to use an angular coordinate system for the remaining integrals which facilitates increasing the number of increments when the variables of integration are close to the source coordinates. This is most easily accomplished if the source (or the irradiated spot) is near an origin or a "pole" of the coordinate system. Since it is desirable to have a handle on the singly scattered radiance received at the irradiated spot as a function of the angle of incidence, a spherical coordinate system was chosen which placed the irradiated spot at the origin and placed the source at the "pole". This is equivalent to rotating a standard spherical coordinate system with its "pole" at the zenith through the angle α defined in Section 7.1. The coordinates in this rotated system are designated by ϕ' and μ' .

Since μ' is the cosine of an angle (θ'), equal increments in μ' correspond to unequal increments in θ' . In fact, equal increments in μ' would cause the smallest increments in θ' to occur around $\theta' = 90^\circ$, which is just the opposite of what is needed. The next logical choice might be between using geometric increments in θ' or using geometric increments in μ' . Geometric increments in θ' would prevent the use of the trigonometric identities used for the ϕ' integral (Section 7.1) and would require that $\sin\theta'$ and $\cos\theta'$ be recalculated after each increment in θ' . On the other hand, geometric increments in μ' only require that one square root be calculated after each increment:

$$\sin\theta' = \sqrt{1 - \mu'^2} \quad (\text{see equation for } \mu \text{ in Section 7.1})$$

This latter approach is used in both computer programs, in which case:

$$\mu' + \Delta\mu' = 1 - (1 - \mu')/\alpha_{\mu'}, \quad , \quad \alpha_{\mu'} > 1$$

A value of $\alpha_{\mu} = 1.2$, corresponding to 12.6 iterations per decade (order of magnitude), has been found to produce accuracies within 10% for the μ' integral. The value of α_{μ} is the most critical for the contributions to the integral near $\mu' = 0$ ($\theta' = 90^\circ$), since the first effective increment in θ' is as large as $\Delta\theta' = 9.6^\circ$ for $\alpha_{\mu} = 1.2$.

When the μ' integral begins to converge, the remainder of the integral is computed by assuming that the integrand is constant for the remaining values of μ' , and this remainder is added to the running sum to obtain the total integral. One needs to be careful with this approximation. If the source is above a low lying fog layer, unusually large contributions to the μ' integral come from directions which are somewhat distant from the source direction. This happens because there are a great many scattering centers along those directions which cover large distances within the fog. As μ' approaches unity (θ' approaches 0°) the distance for which these rays of integration remain in the fog layer decreases dramatically. At the same time the scattering phase angle falls within the range $\chi \sim 90^\circ$ (e.g. $45^\circ \leq \chi \leq 90^\circ$) for which little scattering occurs. This combination of effects can cause the μ' integral to appear to converge at values of μ' corresponding to $\theta' \sim 50^\circ$. Since such angles are much too large for an accurate estimate for the remainder of the integral to be made, one must input to the computer programs an unusually stringent convergence criterion for this situation. As a check on this problem, the computer programs tabulate the z integral, the changes to the μ' integral, and the running sum of the μ' integral for each value of μ' .

CONCLUSIONS AND RECOMMENDATIONS

In this report we have developed practical atmospheric-radiative-transfer models which are used to calculate the natural and artificial radiation fields in atmospheres ranging in visibility from the clearest possible atmosphere to the densest fog. The model for calculation of the natural illumination due to solar or lunar sources is valid for the spectral range $\sim 0.30 \mu\text{m}$ to $3.0 \mu\text{m}$ in that multiple scattering by gases and aerosols is accounted for. At the present time, gaseous absorption is excluded from the computational model but absorption by particulates is included. It is also assumed that the surface is a uniform, flat, Lambertian (perfectly diffuse) reflector. We have seen that the spectral irradiance (or illuminance) on the surface is dependent upon the solar (or lunar) zenith angle, atmospheric visibility, and surface reflectance in a somewhat complicated way. The surface illumination may increase or decrease with increasing atmospheric turbidity depending upon the surface reflectance. These effects are not always made evident when using empirical models of atmospheric radiation due to their limited range of parameters. Sound physical principles have been used in the development of this radiative-transfer model and the results of calculations based upon this model have been compared with results from more elaborate but also more lengthy mathematical calculations and the agreement is excellent.

A detailed, mathematically exact model has also been developed in this report which was used to calculate the singly-scattered radiation field in any uniform atmosphere due to point sources (flares). Here, we found some interesting and unexpected results. For uniform fogs, a flare within the fog produces a highly concentrated distribution of radiation on the surface whereas a flare above the fog layer produces a much more extended distribution of radiation. Hence, if it is desirable to create a relatively broad illumination level over an extended area then flares should be ignited well above a fog. Some caution should be urged in the

interpretation of these results however, since multiple scattering effects have not been included in the analysis. Inclusion of multiple scattering would probably tend to broaden the spatial distribution due to the fact that scattering always tends to redistribute the radiation field. As indicated in Section 7, there were many computational problems which had to be overcome in the detailed numerical integration used in the point source model. The accuracy of the results were tested by taking a point source (the sun) at an altitude of 91 million miles and comparing one irradiance with the irradiance as calculated according to the usual, verified, multiple-scattering model.

It is difficult to compare model calculations with experimental results since the experimentalists rarely define or estimate critical parameters. Many times a report will read "partly cloudy" or "low visibility", which is quite vague and does not quantify the necessary parameters of visual range or optical thickness. What is needed is a detailed, controlled experiment performed under a variety of environmental conditions. More reasonable comparisons can then be made.

Thus, in conclusion, we have a multiple-scattering model which can be used to calculate the natural illumination level in clear, hazy, or foggy atmospheres as a result of the known solar or lunar input irradiance at the top of the atmosphere. Also, we have a single-scattering point source model which can be used to calculate the illumination level on the surface as a result of any number of flares embedded in clear, hazy, or foggy atmospheres.

Before a complete model of the radiation field can be made for all environmental conditions, there is some additional work which must be done. We recommend the following:

1. Fog and Cloud Model Parameterization: We have generated the mathematical methods which can be used to calculate the radiation field in an atmosphere in which flares are the sources. As an illustration of the computational techniques we have calculated the illumination on the surface for a simple fog. It remains to be seen however, to what extent

the spatial distribution changes if different fogs or cloud layers are present. Perhaps a flare within or above a cloud layer will produce a more extended spatial distribution of illumination than one within a dense fog. Also, multiple scattering should be included in the point source analysis, especially for dense fogs or clouds.

2. Temporal Effects: Specific requirements usually require that results on the signatures of various objects in a given scene be generated within minutes or hours rather than days. For this reason, one should consider the temporal variation in the environment. For example, in thirty minutes a fog can change its optical properties considerably, and meteorological input data must be updated in a much shorter time interval. Also, wind-blown dust and smoke can greatly alter the illumination level for a scene in a matter of seconds. It would be desirable, therefore, to model the radiation field, both natural and artificial, as a function of the time-varying environmental parameters.

3. Distributed Sources: One of the most important sources of radiation, particularly at night, is the diffuse sky radiation arising from distant terrain sources such as city lights. Mountains and large hills can also reflect solar or lunar radiation. As a result of advanced mathematical techniques partially used in the solution of the point source problem, we have developed the capability of modeling a distributed source of radiation such as that arising from a collection of city lights, illuminated clouds, hillsides, fires, etc. Clearly, this modeling capability should be implemented for target signature analysis studies, especially for cloudless, moonless nights.

4. Surface Effects: In almost all radiative-transfer analysis one assumes a perfectly diffuse (Lambertian) for mathematical simplicity. In actual practice, however, such a surface is never realized. In fact, strong goniometric properties exist for many natural and man-made surfaces and such properties can affect the directly reflected radiation by a

considerable amount. Also, it is recommended that reflection of flare radiation by the surface be included in the continuing analysis of the radiation field. Since the reflectance of vegetation and other natural materials is quite high (~50-60%) in the near infrared this effect could be of major importance.

5. Target Illumination: Actual targets are not horizontal, flat objects lying on horizontal surfaces but are extended objects characterized by many panels oriented at all directions with respect to the surface. The question arises, what is the illumination on each panel and what is the luminance from each panel as a result of the natural and artificial radiation fields? Some empirical models have been developed which attempt to answer this question for daytime natural sources such as sunlight. What is needed however, is a complete, unified model which can be used to predict the illumination on specific targets for flares and natural sources of illumination for various environmental conditions.

6. Thermal Infrared: It is usually assumed that scattering is only of importance in the visible part of the spectrum. While that assumption is generally true for clear or hazy atmospheres it is certainly not true for clouds, fogs, or dust and smoke plumes. The reason is that the particles are of the same order of magnitude as the wavelength in the infrared ($\sim 5 \mu\text{m} - 12 \mu\text{m}$) and scattering can be of considerable importance. Hence, one should consider scattering and emission of radiation by particulates for the thermal region.

7. Other Effects: Finally, we recommend that additional subjects be investigated. One of these is the illumination due to realistic anisotropic flares. It is assumed that a flare is represented by an isotropic point source, whereas, in reality it has an intrinsic radiation pattern approximately that of a dipole field. This effect could be of importance as we have seen in the current analysis. Another effect is the radiation field arising from searchlight illuminated clouds. This

is a distributed source which was included in an above section. Gaseous absorption can also be included in the infrared. We have models which will determine the radiance and transmittance through atmospheres with various profiles of humidity, pressure, and temperature.

It is believed by the authors that if the above recommendations were carried out a much more comprehensive model would result which could be used in target signature analysis investigations.

APPENDIX

As has been shown throughout this report the illumination due to natural and artificial sources of radiation depends upon many parameters and the results cannot be represented by a single graph or chart. Nevertheless, here we shall present a simple description of the overall procedure whereby a user can obtain reasonably accurate values for the illumination on the Earth's surface without having to go through all of the computational details included in this report.

The spectral irradiance due to the moon is given by Figs. 28, 29, and 30. Any visibility condition from a visual range of 336 km down to a visual range of 2 km can be determined by interpolation and by referring to Figs. 32 and 33. If visual range is not available to the user in field applications then an appropriate parameter might be the spectral transmittance, usually obtainable by a laser transmissometer. In this case, the lunar irradiance values can be extended to very hazy or foggy conditions as illustrated in Figs. 34, 35, and 36. Corresponding values for any other wavelength can be determined by multiplying these curves by the lunar curve of Figure 21. Likewise, any lunar phase may be considered by multiplying the curves by the phase function of Figure 19.

A similar procedure can be given for the description of the illumination due to point sources of radiation such as flares. If we consider a single flare with an output spectral power of one watt per micrometer, then the irradiance for a flare of any power can be found by simply multiplying the power by the curves of Figs. 39 through 48. Most of the curves are normalized to a wavelength of 0.55 μm but any wavelength may be considered by interpolation from Figs. 45, 46, 47, 48, and by considering the intrinsic spectral power output of a particular flare. The intrinsic spectral power outputs of two flares are represented in Figs. 49 and 50.

For a combination of flares in an arbitrary configuration the total irradiance on the surface can be found by simply adding the results for each flare separately. Since this procedure is time consuming to carry out for

each configuration, we have used a computer plotting technique. The results for a few simple configurations are presented in Figs. 52 through 56.

The above is a simple description of a method by which one can obtain illumination levels on the ground for moonlight and artificial flares. The basic parameters which are required are: visual range (km) or spectral transmittance (dimensionless), surface albedo (dimensionless), date, time of day, flare configuration, and type of fog. All of these parameters except the last are relatively easy to specify. We have given results in this report based upon "standard" or normal fog conditions. If there are unusual conditions present then a more detailed treatment is necessary. The procedures for calculating these detailed parameters are given in Sections 3 and 4.

REFERENCES

1. R. M. Goody, Atmospheric Radiation, Oxford University Press, New York, 1964.
2. G. M. Hidy and J. R. Brock, An Assessment of the Global Sources of Tropospheric Aerosols, Academic Press, New York, 1971, p. 1088.
3. F. E. Volz, Infrared Absorption by Atmospheric Aerosol Substances, J. Geophys. Res., 77, No. 6, 1972, p. 1017.
4. F. E. Volz, Infrared Optical Constants of Ammonium Sulfate, Sahara Dust, Volcanic Pumice, and Flyash, Appl. Optics, 12, No. 3, 1973, p. 564.
5. G. W. Grams, I. H. Elifford, Jr., B. G. Schuster, and J. J. DeLuisi, Complex Index of Refraction of Airborne Fly Ash Determined by Laser Radar and Collection of Particles at 13 km, J. of Atmos. Sciences, 29, 1972, p. 900.
6. D. F. Flanigan and H. P. DeLong, Spectral Absorption Characteristics of the Major Components of Dust Clouds, Appl. Optics, 10, No. 1, 1971, p. 51.
7. C. E. Junge, Journal Meteorol., 12, 1955, p. 13.
8. A. C. Holland and G. Gagne, The Scattering of Polarized Light by Polydisperse Systems of Irregular Particles, Appl. Optics, 9, No. 5, 1970, p. 1113.
9. R. S. Powell, R. R. Circle, D. C. Vogel, P. D. Woodson III, and B. Donn, Optical Scattering from Non-Spherical Randomly Aligned, Polydisperse Particles, Planet. Space Sci., 15, 1967, p. 1641.
10. D. M. Ruthven and K. F. Loughlin, Effects of Particle Shape and Size Distribution on the Transient Solution of the Diffusion Equation, Nature Phys. Sci., 230, 1971, p. 69.
11. D. Deirmendjian, Electromagnetic Scattering on Spherical Polydispersions, Elsevier, New York, 1969, p. 78.
12. C. Wiegand, Chemical Composition and Radioactivity of the Atmosphere, C. Junge, World Publishing Co., Cleveland, 1963.
13. L. S. Ivlev, Aerosol Model of the Atmosphere, Prob. Fiz. Atmos. Leningrad, No. 7, 1967, pp. 125-160.

14. V. Ye. Zuyev, Propagation of Visible and Infrared Waves in the Atmosphere, NASA TTF-707, NTIS, U. S. Department of Commerce, Springfield, Va., 1970.
15. B. J. Mason, The Physics of Clouds, Clarendon Press, Oxford, 1971.
16. N. A. Fuchs, The Mechanics of Aerosols, Pergamon, Elmsford, N. Y., 1964.
17. C. N. Davies, Aerosol Science, Academic Press, New York, 1964.
18. H. L. Green and W. R. Lane, Particulate Clouds, Dusts, Smokes, and Mists, 2nd Edition, D. Van Nostrand, Inc., Princeton, 1964.
19. M. Neiburger and C. W. Chien, Physics of Precipitation, Geophys. Monogr. No. 5, Washington, D.C., 1960, pp. 191-210.
20. H. Koschmieder, Theorie der horizontalen Sichtweite, Beitr. Phys. freien Atm. 12, 1924, pp. 33-53.
21. L. Elterman, U.V., Visible, and IR Attenuation for Altitudes to 50 km, 1968, AFCRL Report No. 68-0153, Office of Aerospace Research.
22. L. Elterman, Vertical-Attenuation Model with Eight Surface Meteorological Ranges 2 to 13 Kilometers, AFCRL Report No. 70-0200, 1970, Office of Aerospace Research.
23. A. Arnulf, J. Bricard, E. Cure, and C. Veret, Transmission by Haze and Fog in the Spectral Region 0.35 to 10 Microns, J. of the Opt. Soc. of Amer., Vol. 47, No. 6, 1957, pp. 491-498.
24. R. G. Eldridge, Haze and Fog Aerosol Distributions, J. of Atmos. Sciences, 1966, pp. 605-613.
25. D. Deirmendjian, Quart. Journal Royal Meteorol. Soc. 86, 371, (1960).
26. H. C. van de Hulst, Light Scattering by Small Particles, John Wiley and Sons, 1957.
27. M. Kerker, The Scattering of Light and Other Electromagnetic Radiation, Academic Press, 1969.
28. W. Trabert, Die Extinction des Lichtes in einem truben Medium (Sichtweite in Wolken), Meteor. Z., 18, pp. 518-525, 1901.
29. J. E. Jiusto, Project Fog Drops, Investigation of Warm Fog Properties and Fog Modification Concepts, NASA CR-72, 1964.

30. USAF Air Research and Development Command, Handbook of Geophysics, The Macmillan Co., New York, Rev. Ed., 1961.
31. J. C. Arvesen, R. N. Griffin, Jr. and B. D. Pearson, Jr., Determination of Extraterrestrial Solar Spectral Irradiance from a Research Aircraft, Appl. Optics, 8, No. 11, 1969.
32. M. P. Thekaekara and A. J. Drummond, Standard Values for the Solar Constant and Its Spectral Components, Nature Phys. Sci., 229, 1971, pp. 6-9.
33. H. N. Russel, Ap. J. 43, 1916, p. 117.
34. M. G. Rougier, Ann. Obs. Strassbourg, 2, 1933, p. 205.
35. K. Bullrich, Ber. Deutsch. Wetterd., U.S. Zone No. 4, 1948.
36. A. P. Lane and W. M. Irvine, Astron. J. 78, No. 3, 1973, p. 267.
37. T. P. Condron, J. J. Lovett, W. H. Barnes, L. Marcotte, and R. Nadile, Gemini 7 Lunar Measurements, AFCRL-68-0438, Sept., 1968.
38. D. R. E. Brown, Natural Illumination Charts, Report No. 374-1, Dept. of the Navy, Bureau of Ships, Washington, D.C., 1952.
39. D. Pleiter and G. A. Morley, Night Radiation Measurements, Defense Documentation Center, AD 865252.
40. M. L. Vatsia, U. K. Stich, and D. Dunlap, J. Opt. Soc. Am. 59, 483 (1969).
41. L. M. Biberman, Natural Levels of Illumination and Irradiance, Photoelectronic Imaging Devices, Vol. 1, Chapt. 3, Plenum Press, N.Y., 1971.
42. R. E. Turner, Radiative-Transfer in Real Atmospheres, ERIM 190100-24-T, Environmental Research Institute of Michigan, 1974.
43. W. A. Malila, R. E. Crane, and R. E. Turner, Information Extraction Techniques for Multispectral Scanner Data, Report No. 31650-74-T, Willow Run Laboratories, Ann Arbor, 1972.